

---

Electronic Thesis and Dissertation Repository

---

12-8-2014 12:00 AM

## Morphological And Structural Mapping Of The Oudemans Impact Crater Layered Central Uplift, Mars

Bahareh Kasmai, *The University of Western Ontario*

Supervisor: Dr. Gordon osinski, *The University of Western Ontario*

Joint Supervisor: Dr. Livio Tornabene, *The University of Western Ontario*

Joint Supervisor: Dr. Dazhi Jiang, *The University of Western Ontario*

A thesis submitted in partial fulfillment of the requirements for the Master of Science degree in Planetary Science

© Bahareh Kasmai 2014

Follow this and additional works at: <https://ir.lib.uwo.ca/etd>



Part of the [Geology Commons](#), [Geomorphology Commons](#), [Other Earth Sciences Commons](#), and the [Tectonics and Structure Commons](#)

---

### Recommended Citation

Kasmai, Bahareh, "Morphological And Structural Mapping Of The Oudemans Impact Crater Layered Central Uplift, Mars" (2014). *Electronic Thesis and Dissertation Repository*. 2628.  
<https://ir.lib.uwo.ca/etd/2628>

This Dissertation/Thesis is brought to you for free and open access by Scholarship@Western. It has been accepted for inclusion in Electronic Thesis and Dissertation Repository by an authorized administrator of Scholarship@Western. For more information, please contact [wlsadmin@uwo.ca](mailto:wlsadmin@uwo.ca).

MORPHOLOGICAL AND STRUCTURAL MAPPING OF THE OUDEMANS  
IMPACT CRATER LAYERED CENTRAL UPLIFT, MARS

(Thesis format: Monograph)

by

Bahareh Kasmai

Graduate Program in Geology (Planetary Science)

A thesis submitted in partial fulfillment  
of the requirements for the degree of  
Master of Science – Geology (Planetary Science)

The School of Graduate and Postdoctoral Studies  
The University of Western Ontario  
London, Ontario, Canada

©Bahareh Kasmai 2014

## Abstract

Central uplifts in large meteorite impact craters provide valuable information about the subsurface geology of planetary bodies. Compared to impact craters on Earth, Martian central uplifts can be well exposed and can be mapped in detail by using satellite imagery. Central uplifts preserve morphological and structural features formed as result of the combination of emplacement during the impact process, post impact modification, and erosion over time. In this study, the Oudemans Crater central uplift (the largest central uplift with layers on Mars) was investigated. Oudemans (9.89 S, 268.1 E) is 124 km in diameter and is located in the Sinai Planum at the western end of Valles Marineris canyon system; it also is part of the Tharsis province, which is major volcanic region on Mars. The central uplift was structurally and geomorphologically mapped and analyzed using High Resolution Imaging Science Experiment (HiRISE) imagery combined with other data sets tied to topographic data as a base map in Arc-GIS. The Oudemans Crater central uplift was divided into five main geomorphologic units: 1) exposed bedrock; 2) megabreccia; 3) clast-rich impact melt rock; 4) clast-poor and pitted impact melt; and 5) erosional deposits (mass wasting unit and aeolian deposit) units. Faults, folds, dykes, and deformed bedding were also mapped. Through structural mapping, deformed, folded, and fractured layers were mapped as they provide a frame of reference with respect to the structural deformation of the uplift. The preferred orientation of faults appears to be perpendicular to the impact trajectory (oblique trend to the central uplift) and to be thrust faults. Four obvious folds were mapped towards the centre of the uplift consistent with increased deformation towards the Crater centre. Dykes are typically perpendicular to the bedrock and can be seen mostly in the centre of the central uplift.

## Keywords

Mars, Impact cratering, Impact processes, Oudemans, Central uplifts, Layered bedrock.

## Co-Authorship Statement

I conducted the mapping and GIS work and processed and analyzed the data. Dr. Osinski and Dr. Tornabene provided training in remote sensing and GIS mapping techniques, guidance on how to conduct research, proper presentation of the material, and input into the text and interpretation.



## Acknowledgments

I would like to express my deepest gratitude to my advisors: Dr. G. R. Osinski for his excellent guidance, caring, and continuous support in the preparation of my thesis. I appreciate him for his vast skill and detailed review during the preparation of this thesis. His moral support enabled me to complete my work successfully; Dr. L. L. Tornabene for his understanding, great assistance, and encouragement and for pushing me farther than I thought I could go. He was positive and gave generously of his time and vast knowledge. He always knew where to look for the answers to obstacles while leading me to the right source, theory, and perspective. I highly thankful him for his assistance in teaching valuable software (e.g., GIS, JMars, remote sensing) that were useful for my project; Dr. D. Jiang for showing me the road and helping to get me started on the path to this degree. His enthusiasm and faith in me throughout have been extremely helpful. He was always available for my questions about structural geology.

To the staff at the Geology department of University of Western Ontario, thank you—specially to Margaret Moulton, Marie Schell and Kevin Jordan for always give me words of encouragement. To all my friends, Bianca, Faranak, B, Hadis, and Anna, thank you. I would like personally thank Bianca for giving me some help for improving my work.

I would also like to warmly thank and appreciate my family for their material and spiritual support in all aspects of my life.

I would like to thank my sisters, Behshid, and Behnoush, who have provided assistance and hope in numerous ways to survive me from stress.

# Table of Contents

## Contents

Abstract .....	iii
Co-Authorship Statement.....	iv
Acknowledgments.....	v
Table of Contents .....	vi
List of Figures .....	viii
List of Appendices and Tables.....	xii
1. Introduction .....	1
2. Background .....	3
2.1. The surface of Mars.....	3
2.1.1. Overview .....	3
2.1.2. Global Structures and Topography on Mars.....	3
2.1.3. Martian Geological crater chronology.....	8
2.2. Impact crater formation.....	10
2.2.1. Contact and compression stage.....	11
2.2.2. Excavation .....	13
2.2.3. Modification .....	14
2.3. Impact crater morphology and morphometry.....	16
2.4.1. Impact ejecta deposits.....	19
2.4.2. Impact melt deposits.....	20
2.4.3. Impact breccia.....	22
2.6. Geologic setting of Oudemans Crater .....	23
2.7 Previous work on Oudemans Crater and other Martian layered uplifts.....	24
3. Data and Methods .....	26
4. Results .....	30
4.1. Morphologic Mapping.....	30
4.1.1. Unit 1: Bedrock .....	32
4.1.2. Unit 2: Megabreccia .....	34

4.1.4. Unit 4: Smooth and pitted material.....	38
4.1.5. Unit 5: Mass wasting .....	39
4.1.6. Unit 6: Aeolian deposits .....	40
4.2. Structural Mapping.....	41
4.2.1 Fractures .....	42
4.2.2. Faults .....	44
4.2.3. Folds .....	46
4.2.3. Dykes .....	48
5. Interpretations and Discussion.....	53
5.1. Exposed layered bedrock and undivided bedrock.....	53
5.2. Crater-fill deposits.....	55
5.2.1 Impact melt rocks .....	55
5.2.2 Martian crater-related pitted material (volatile-rich impact melt deposits).....	58
5.2.3 Megabreccia .....	59
5.3. Mass wasting and aeolian deposits.....	60
5.4. Nature of the central uplift at Oudemans Crater .....	60
5.5. Stratigraphic history .....	63
6. Summary and Conclusion.....	65
7. References .....	74
Curriculum Vitae .....	81

# List of Figures

FIGURE 1. MARS ORBITER LASER ALTIMETRE (MOLA) MAPS CLEARLY SHOW A DISTINCTION BETWEEN LOWLANDS AND HIGHLANDS. THE NORTHERN LOWLANDS HAVE OVERALL ELEVATIONS ABOUT FIVE KILOMETERS LOWER THAN THE CRATERED UPLANDS OF THE SOUTHERN HEMISPHERE. <a href="http://www.psr.d.hawaii.edu">HTTP:// WWW.PSRD.HAWAII.EDU</a> . ....	4
FIGURE 2. PART OF GLOBAL TOPOGRAPHIC MAP OF MARS ON MOLA SHADED-RELIEF INDICATING THE TOTAL STUDIED AREA (OUDEMANS CRATER). ZUBER@THARSIS.GSFC.NASA.GOV. ....	6
FIGURE 3. MARS CHRONOLOGY TIMESCALE SYSTEM AND OCCURRED EVENTS FROM TANAKA ET AL., (1986). ....	9
FIGURE 4. GLOBAL SCALE GEOLOGICAL MAP OF MARS, USING MOLLWEIDE PROJECTION (WITH EAST LONGITUDE AND CENTRED ON 260°E) AND MOLA SHADED RELIEF AS BACKGROUND. N=NOACHIAN, H=HESPERIAN, A=AMAZONIAN, E=EARLY, L=LATE. MAP FROM NIMMO AND TANAKA (2005). ....	10
FIGURE 5. SERIES OF SCHEMATIC CROSS-SECTIONS DEPICTING THE THREE MAIN STAGES IN THE FORMATION OF IMPACT CRATERS. THIS MULTI-STAGE MODEL ACCOUNTS FOR MELT EMPLACEMENT IN BOTH SIMPLE (LEFT PANEL) AND COMPLEX CRATERS (RIGHT PANEL). FOR THE MODIFICATION STAGE SECTION, THE ARROWS REPRESENT DIFFERENT TIME STEPS, LABELLED ‘A’ TO ‘C’. INITIALLY THE GRAVITATIONAL COLLAPSE OF CRATER WALLS AND CENTRAL UPLIFT (A) RESULTS INWARD MOVEMENT OF MATERIAL. LATER, MELT AND CLASTS FLOW OFF THE CENTRAL UPLIFT (B). THEN, THERE IS CONTINUED MOVEMENT OF MELT AND CLASTS OUTWARDS ONCE CRATER WALL COLLAPSE HAS LARGELY CEASED (C). AFTER FROM OSINSKI ET AL. 2011. FIGURE AND CAPTION FROM OSINSKI ET AL. 2012. ....	12
FIGURE 6. DISTRIBUTION OF HYDROTHERMAL DEPOSITS WITHIN AND AROUND A TYPICAL COMPLEX IMPACT CRATER. MODIFIED FROM OSINSKI ET AL. (2012). FIGURE AND CAPTION FROM OSINSKI ET AL 2012. ....	16
FIGURE 7. HiRISE IMAGE OF AN UNNAMED SIMPLE CRATER ON MARS (38.7 ° N/316.1 ° E) DISPLAYING AN ELEVATED CRATER RIM AND STEEPLY DIPPING UPPER CAVITY WALLS. THE MID AND LOWER PARTS OF THE WALL ARE COVERED BY TALUS DEPOSITS. IMAGE: NASA/JPL/UNIVERSITY OF ARIZONA. (B) KAGUYA/SELENE IMAGE (S0000001616_1906) OF THE COMPLEX IMPACT CRATER ARISTARCHUS ON THE MOON, SHOWING A CENTRAL PEAK, A FLAT CRATER FLOOR WITH ISOLATED HUMMOCKS AND AN EXTENSIVE SLUMP TERRACE ZONE. FIGURE AND CAPTION FROM KENKMANN ET AL (2013). ....	18
FIGURE 8. SCHEMATIC DIAGRAM OF A TYPICAL COMPLEX IMPACT STRUCTURE SHOWING THE MAIN SETTINGS IN WHICH IMPACT MELT-BEARING MATERIALS ARE TYPICALLY FOUND. FIGURE AND CAPTION FROM OSINSKI ET AL 2013. ....	21
FIGURE 13. OUDEMANS CRATER ON THEMIS IMAGE. BLUE CIRCLE SHOWS THE CRATER RIM AND RED CIRCLE SHOWS THE CENTRAL UPLIFT OF THE CRATER, AND YELLOW POLYGONS SHOW THE UPLIFTED CENTRAL UPLIFT IN THE CORE, AND A GAP IN THE NORTHWESTERN PART OF THE	

RIM . THEMIS_IRDAY_256PPD_West_v2_EQUIRECT_CLON0_LY80. IMAGE: NASA/JPL-CALTECH/ARIZONA STATE UNIVERSITY.....	28
FIGURE 15. GEOMORPHOLOGICAL AND STRUCTURAL MAP OF THE OUDEMANS CRATER CENTRAL UPLIFT. ....	31
FIGURE 16. AREA A IN UNIT 1A SHOWS LAYERED BEDROCK IN THE WESTERN PART OF THE CENTRAL UPLIFT (DTM SDX ON ESP_028449_1700_RED_A_01_ORTHO), AND AREA B MAPPED HiRISE IMAGE (ESP_011676_1700_RED). IMAGE: NASA/JPL/UNIVERSITY OF ARIZONA. LAYERED BEDROCK SURROUNDED BY SOME UNITS SUCH AS DARK-TONED CLAST-RICH SHOWED BY RED AND SMOOTH AND PITTED MATERIALS BY GREEN, AND COVERED IN SOME PART BY AEOLIAN DEPOSITS IN LIGHT GREY.....	33
FIGURE 17. THIS IMAGE SHOWS LAYERED BEDROCK OUTLINED BY THE RED POLYGON IN THE CENTRE. BEDDING IS SHOWN BY THE PURPLE LINES. IMAGE: NASA/JPL/UNIVERSITY OF ARIZONA. ....	33
FIGURE 18. LIGHT BROWN POLYGONS OUTLINE COATED BEDROCK WITH A LACK OF LAYERING (UNDIVIDED BEDROCK). THE BASE IMAGE COMPRISES PART OF FOUR HiRISE IMAGES, PSP_002446_1700_RED, ESP_026194_1700_RED, ESP_027117_1700_RED, ESP_026273_1700_RED. IMAGE: NASA/JPL/UNIVERSITY OF ARIZONA.....	35
FIGURE 19. IMPACT MEGABRECCIA SHOWING LAYERED MEGABRECCIA WITH DIFFERENT SIZE OF CLASTS, ALL CLASTS OUTLINED WITH ORANGE POLYGONES. PART OF HiRISE IMAGE ESP_036176_1700_RED. IMAGE: NASA/JPL/UNIVERSITY OF ARIZONA.....	36
FIGURE 20. DARK-TONED CLAST-RICH IMPACT DARK-TONED UNIT IN THE WESTERN PORTION OF THE OUDEMANS CRATER ON HiRISE AND CTX IMAGES ESP_011676_1700_RED. LARGER CLASTS ARE SHOWED BY LIGHT PURPLE POLYGONS IN THIS UNIT. IMAGE: NASA/JPL/UNIVERSITY OF ARIZONA.....	37
FIGURE 21. DARK-TONED AND LIGHT-TONED PIT UNIT SEEN IN GREY COLOUR IN MOST PART OF THE AREA IN THE CENTRAL UPLIFT ON CTX IMAGERY. P05_003079_1714_XN_08S091W_FINAL.TIF, P06_003501_1713_XN_08S092W_FINAL.TIF, G20_026194_1690_XN_11S091W_FINAL.TIF. IMAGE: NASA/JPL/UNIVERSITY OF ARIZONA. ....	38
FIGURE 22. MASS WASTING UNIT OBSERVED IN THE NORTHERN AND CENTRAL PART OF THE CENTRAL UPLIFT. HiRISE IMAGE PSP_002446_1700_RED AND ESP_026194_1700_RED. IMAGE: NASA/JPL/UNIVERSITY OF ARIZONA. ....	39
FIGURE 23. AEOLIAN DEPOSITS SEEN MOSTLY IN THE NORTHERN OF THE CRATER, HiRISE IMAGE ESP_026194_1700. IMAGE: NASA/JPL/UNIVERSITY OF ARIZONA. ....	40
FIGURE 24. MAPPED HiRISE IMAGE ESP_027882_1700_RED, ..... SHOWING TILTED LAYERS IN BLUE COLOUR. IMAGE: NASA/JPL/UNIVERSITY OF ARIZONA...	41
FIGURE 25. CLOSE UP OF FRACTURES IN BEDROCK. PORTION OF HiRISE IMAGE, ESP_027882_1700_RED. IMAGE: NASA/JPL/UNIVERSITY OF ARIZONA.....	42

FIGURE 26. ROSE DIAGRAM OF FRACTURE TREND. IMAGE: NASA/JPL/UNIVERSITY OF ARIZONA. ....	43
FIGURE 27. THIS IMAGE SHOWS DISPLACEMENTS ACROSS FAULTS WITH HIGH DISTRIBUTION TOWARD CENTRE .....	44
OF THE CENTRAL UPLIFT, FAULTS SEEN BY GREEN LINES, PSP_002446_1700_RED.....	44
IMAGE: NASA/JPL/UNIVERSITY OF ARIZONA. ....	44
FIGURE 28. THIS IMAGE SHOWS ROSE DIAGRAM OF FAULTS IN SIX DIVIDED SECTIONS. IMAGE: NASA/JPL/UNIVERSITY OF ARIZONA. ....	45
FIGURE 29. FEW CLEAR FOLDS OBSERVED IN THE LAYERED SECTION OF THE CRATER ON HiRISE IMAGES; PSP_002446_1700_RED, ESP_027882_1700_RED. PURPLE LINES SHOW THE BEDROCK, WHITE LINES SHOW THE LIMBS AND RED LINES SHOW THE FOLD AXIS. IMAGE: NASA/JPL/UNIVERSITY OF ARIZONA. ....	47
FIGURE 30. IMAGE OF FOLD B IN HiRISE PSP_002446_1700_RED, FOLD AXIS DISPLAYED BY RED ARROW, BEDDING SEEN BY PURPLE LINES, FAULTS BY GREEN LINES, DYKES BY ORANGE LINES, AND FRACTURES BY PINK LINES. IMAGE: NASA/JPL/UNIVERSITY OF ARIZONA.....	48
FIGURE 31. THIS IMAGE SHOWS HIGHER CONCENTRATION OF DYKES IN ORANGE COLOUR IN THE CENTRE, OUTLINED BY THE RED CIRCLE. IMAGE: NASA/JPL/UNIVERSITY OF ARIZONA. ....	49
FIGURE 32. THIS IMAGE SHOWS OFFSETS CAUSED BY DYKES WHICH SHOWN BY ORANGE ARROWS OBSERVED IN HiRISE PSP_008195_1700_RED, RED DIGITS (4 KM, AND 6 KM) SHOWED A THICKNESS OF THE DYKES. THIS IMAGE IS A CLOSE UP ONE OF THE DYKES SHOWED BY WHITE ARROW IN THE PREVIOUS PHOTO. IMAGE: NASA/JPL/UNIVERSITY OF ARIZONA...	50
FIGURE 33. IMPACT BRECCIA DYKE IS CUTTING SHARPLY THROUGH LAYERS. DYKES SHOWN BY ORANGE POLYLINES AND LAYERS SHOWN BY PURPLE ONES. HiRISE IMAGERY; PSP_008195_1700_RED. IMAGE: NASA/JPL/UNIVERSITY OF ARIZONA. ....	51
FIGURE 34. ROSE DIAGRAMS OF DYKE TREND. IMAGE: NASA/JPL/UNIVERSITY OF ARIZONA. ....	52
FIGURE 35. ROSE DIAGRAMS OF BEDDING TRENDS. IMAGE: NASA/JPL/UNIVERSITY OF ARIZONA. ....	56
FIGURE 37. THIS IMAGE SHOWS KING CRATER ON MOON. Y-SHAPED CENTRAL UPLIFT AND COLLAPSED RIM DISPLAYED BY YELLOW AND ORANGE LINES RESPECTIVELY. ....	62
FIGURE 38. STRATIGRAPHIC COLUMN ORDERED UNITS BY AGE, COMPOSITION AND FORMATION TIME FROM OLDER TO YOUNGER. ....	64

# List of Appendixes and Tables

APPENDIX A. RESULTS FROM ORIENTATION MEASUREMENT OF LINEAR FEATURES OF AREA A.  
..... 67

APPENDIX B. RESULTS FROM ORIENTATION MEASUREMENT OF LINEAR FEATURES OF AREA B.  
..... 68

APPENDIX C. RESULTS FROM ORIENTATION MEASUREMENT OF LINEAR FEATURES OF AREA C.  
..... 69

APPENDIX D. RESULTS FROM ORIENTATION MEASUREMENT OF LINEAR FEATURES OF AREA D.  
..... 70

APPENDIX E. RESULTS FROM ORIENTATION MEASUREMENT OF LINEAR FEATURES OF AREA E.  
..... 71

APPENDIX F. RESULTS FROM ORIENTATION MEASUREMENT OF LINEAR FEATURES OF AREA F.  
..... 72

|

# 1. Introduction

Impact cratering is a complex geological process that has affected the surfaces of all solid planets and moons in our solar system (Melosh, 1989). Impact craters can be classified into two main morphologic types: simple and complex. Simple craters are bowl-shaped depressions with smooth walls lacking terraces filled with impact melt deposits, while complex craters contain terraced walls, flat floors, and central uplifts (Pike, 1980). Remote sensing studies of complex impact craters on planetary bodies provide information relating to the original morphology and morphometry of craters (Osinski and Grieve, 2013). Furthermore impact craters reveal uplifted deep-seated bedrock exposures within their central uplift, but also in the ejecta deposits and walls. Central uplifts of complex craters provide an excellent opportunity to study the deepest portions of the Martian crust globally (Caudill et al., 2012b; Quantin et al., 2012; Tornabene et al., 2012a; Tornabene et al., 2012b).

The exposed uplifted bedrock in the central uplifts of Martian craters provides us with insights into regional geologic history through the exposure of lithologies and the recorded pre-impact target structure and stratigraphy therein e.g., (Tornabene et al., 2012a). Studying the exposed bedrock in the central uplifts of complex craters also provides unique opportunities to investigate the early climate history and habitability through the older underlying bedrock they expose and the impact-generated hydrothermal systems these craters can generate in the presence of water (Osinski and Pierazzo, 2013). Recent detailed investigations of central uplifts show that they are not only comprised of uplifted bedrock, but also various deposits of impact melt rocks, impact breccias, and post-impact deposits e.g., dust, mass-wasting deposits, etc (Ding et al., 2014; Marzo et al., 2010; Nuhn, 2014; Osinski et al., 2011; Tornabene et al., 2010; Tornabene et al., 2014). It is now clear that central uplifts preserve morphological and structural features that are the result of a combination of emplacement during the impact process, post impact modification, and erosion over time (Osinski and Pierazzo, 2013; Tornabene et al., 2012a; Tornabene et al., 2013). As such, they are often difficult to study, but provide important clues regarding the impact process, the formation of central uplifts and the processes that modify them.



Morphological, structural and spectral mapping of impact craters on Mars are, therefore, useful to interpret the geological processes that have shaped and modified the surface (e.g., volcanism, aeolian processes, erosion and deposition, etc.) (Barnhart, 2010; Bleacher et al., 2003; Craddock et al., 1997; Ding et al., 2014; Forsberg-Taylor et al., 2004; Grant et al., 2008b; Melosh, 1989; Platz et al., 2013).

Studies of impact craters on Earth (i.e., terrestrial impact structures) provide many insights into the impact process. However, because of obscuration by vegetation, water or deposits (i.e., Earth's active geologic surface), the original morphology and structures in the majority of terrestrial impact structures are eroded (Kenkmann et al., 2005; Kenkmann et al., 2014). In contrast, many Martian craters are minimally obscured and are well - preserved and, thus, can be geologically mapped in detail by using high-resolution spacecraft imagery (Tornabene et al., 2010; Tornabene et al., 2014). Many researchers tried to understand the formation of central uplifts; such as Kenkmann et al., (2014) who summarized that the weakening mechanism is required to form central uplifts, but the nature of this process remains poorly constrained and understood.

Oudemans Crater, with a 124 km in diameter, was selected here because it has central uplift with well exposed LB and represents the largest layered central uplift on Mars identified to date. Importantly, layers provide a frame of reference with respect to the structural deformation of the uplift, such as folding, and movement-offset along faults (Bridges, 2006; Caudill et al., 2012a; Nuhn, 2014; Wulf et al., 2012).

The goal of this study is to produce a morphological and structural map of the central uplift of the Oudemans Crater on Mars in order to investigate and inform on regional stratigraphy, the relation between morphological units, and structural deformation during the modification stage of crater formation. We attempt to constrain the origin and deformation history of the morphologic units of the central peak of the Oudemans Crater utilizing High Resolution Imaging Science Experiment (HiRISE) (resolution up to 25 cm/pixel), Context Camera (CTX) (~5 m/pixel), and other data to map metre scale features. The research encompasses the morphological and structural analysis of the central uplift. Geological mapping was performed to aid the analysis and to provide a geological framework.

## **2. Background**

### **2.1. The surface of Mars**

#### **2.1.1. Overview**

Mars, the fourth terrestrial planet from the Sun and has one of the most complex geologic histories in our solar system (Fig. 1). Mars has a surface temperature between  $\sim 140^\circ$  and  $300^\circ$  K. The average percentage of carbon dioxide ( $\text{CO}_2$ ) in the atmosphere is 95%, and the mean atmosphere pressure at the surface is  $\sim 6.5$  mbar. Mars has a diameter of  $\sim 6,800$  km, which corresponds to approximately half the size of Earth. Mars possess two small moons: Phobos, and Deimos, which are heavily-cratered planetary bodies, having crater distributions similar to the Moon (Veverka and Thomas, 1979). No active plate tectonics has been observed on Mars as there is no evidence of active ridge and trench systems. However, Mars was once volcanically and tectonically active.

#### **2.1.2. Global Structures and Topography on Mars**

Mars is thought to be a one-plate planet (stagnant lid) with a thick crust. Heat is transported to the surface lying on top of mantle convection, then cooling the outer layers of Mars's surface through lithosphere growth occurred due to stagnant lid mantle convection throughout the evolution, so it can reconcile early crust formation and magnetic field generation (Zuber et al., 2000).

The surface of Mars is characterized by a global- scale dichotomy. The highlands are in the northern Martian hemisphere, and the heavily-crated lowlands located in the southern hemisphere (Wilson, 2009). In other words, the northern and southern hemispheres of Mars have different topographies, elevation, crustal thicknesses, and impact crater densities.

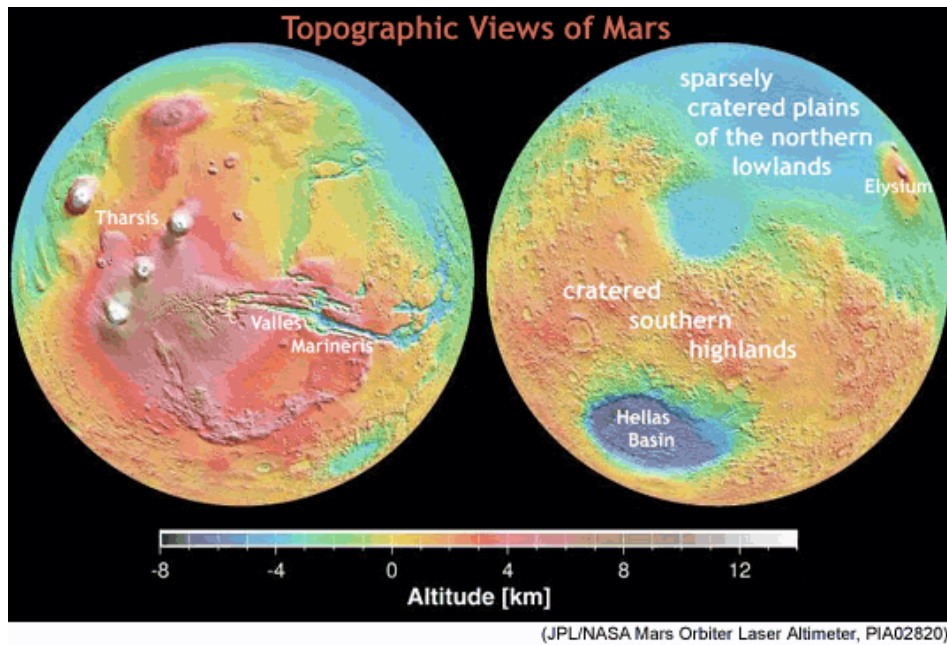


**Figure 1. Mars Orbiter Laser Altimetre (MOLA) maps clearly show a distinction between lowlands and highlands. The northern lowlands have overall elevations about five kilometers lower than the cratered uplands of the southern hemisphere.**  
[http:// www.psrcd.hawaii.edu](http://www.psrcd.hawaii.edu).

The smooth northern lowlands are characterized by vast volcanic plains, while the southern highlands are heavily cratered, and partially covered with extensive lava flows. This dichotomy boundary (the transition between the highlands and lowlands) is one of the earliest global geologic features on Mars that separates the older, heavily-cratered southern hemisphere highlands from the smooth, younger northern hemisphere lowlands (Carr, 2006). This feature is marked by a dramatic elevation change and steep scarp by using topography and gravity, and the root of this separation is a change in crustal thickness along a boundary (Andrews-Hanna et al., 2008).

One observation was about the bimodal crustal thickness distribution between the lowlands and highlands which generated by the excavation of crust during a gigantic impact (Neumann et al., 2004). Another observation was about the dichotomy boundary that now looks like an elliptical shape around Mars. The low- angle massive impacts are generated elliptical basins, such as Hellas basin on Mars. The basin is simulated to be buried by the melt generated by the impact and contained within the basin but much less than earlier (Neumann et al., 2004). So this massive impact source for the crustal dichotomy would leave the largest regions (northern lowlands) in the solar system (Andrews-Hanna et al., 2008) (The thickness of northern part of the crust is 32 km while in Southern part is 58 km

(Carr, 1981; Watters et al., 2007; Zuber et al., 2000). Deposition and erosion by aeolian, fluvial and glacial processes shaped the present-day dichotomy boundary.

The majority of the Martian crust formed in the Noachian (Head et al., 2001; McEwen et al., 1999; Zuber, 2001) with widespread tectonic activity, then the crust formed in the Hesperian (Head et al., 2002) and was followed by the Amazonian. (Carr, 1979) assumed that the Martian crust is made up brecciated lava flows.

Thermal history models of the lithosphere of Mars, based on a factor of mantle heat transfer by stagnant-lid convection, have been explored by (Reese et al., 1998). These models show a global melt zone underneath the lithosphere that is present for a significant part of the Martian evolution, in some models even at present (Reese et al., 1999).

Based on some calculations in these models, Breuer and Spohn (2003) assumed that an early plate tectonics epoch was likely and followed by stagnant lid convection. The models include the effects of mantle differentiation by crust formation after the end of the plate tectonics epoch. The stagnant lid model requires some early superheating of the core to explain an early magnetic field (Breuer and Spohn, 2003; Gerald Schubert, 2001).

Convection models indicate that on a time scale of a few hundred million years the mantle convective engine slowed, as interior heat was lost and as radioactive heat production was concentrated into the shallow crust. Rapid interior cooling led to a globally thick lithosphere. The last 3.5 Gyr of Martian history was marked by slow cooling and by the concentration of volcanic and tectonic activity in ever more limited regions (Gerald Schubert, 2001; Hauck and Phillips, 2002; Weizman et al., 2001).

On Mars, the lack of plate tectonics and lower weathering rates preserve the oldest portions of the Martian crust. Mars displays a wide range of terrains and has significant topographic relief. The highest elevation from zero elevation datum on Mars marked by the summit of Olympus Mons at ~ 27 km while the lowest elevation is about ~ 7 km belonging the floor of the Hellas basin. Heavily cratered terrain occurs mostly in the southern hemisphere. Most of the Martian plains within the cratered terrain are volcanic with a complex interplay of fluvial, aeolian and volcanic processes (Greeley and Spudis, 1978).

These plains are subdivided by both type and age to three categories; moderately cratered plains, ridged plateau plains, and volcanic plains. Martian volcanoes occur as shield volcanoes, dome volcanoes and highland patera. Shield volcanoes in the Tharsis and Elysium regions include multiple flows, sometimes emplaced through lava tubes and channels, typical of shield-forming flows on Earth. Carr (1979) concluded that flow could be carried for long periods by evaluating the pore pressures on Mars. Presence of small ancient channels and valleys networks on Mars show that climatic conditions in the past were variable.

A vast network of canyon system occurs on the surface of Mars for ~4,000 km along the equatorial zone located eastward from the Tharsis Montes and comprising of grabens, canyons, pit craters and channels. The region containing the main canyon system, named Valles Marineris (largest and deepest exposures of layered volcanic rock on Mars) with layered walls is part of the Tharsis region (Beyer and McEwen, 2005; Caudill et al., 2012a). The canyon is subdivided into three sections; Noctis Labyrinthus in the west, the main section of canyons in the centre and a complex eastern part. The study area is located in the western part of this region (between Sinai Planum and Noctis Labyrinthus) (Fig. 2).

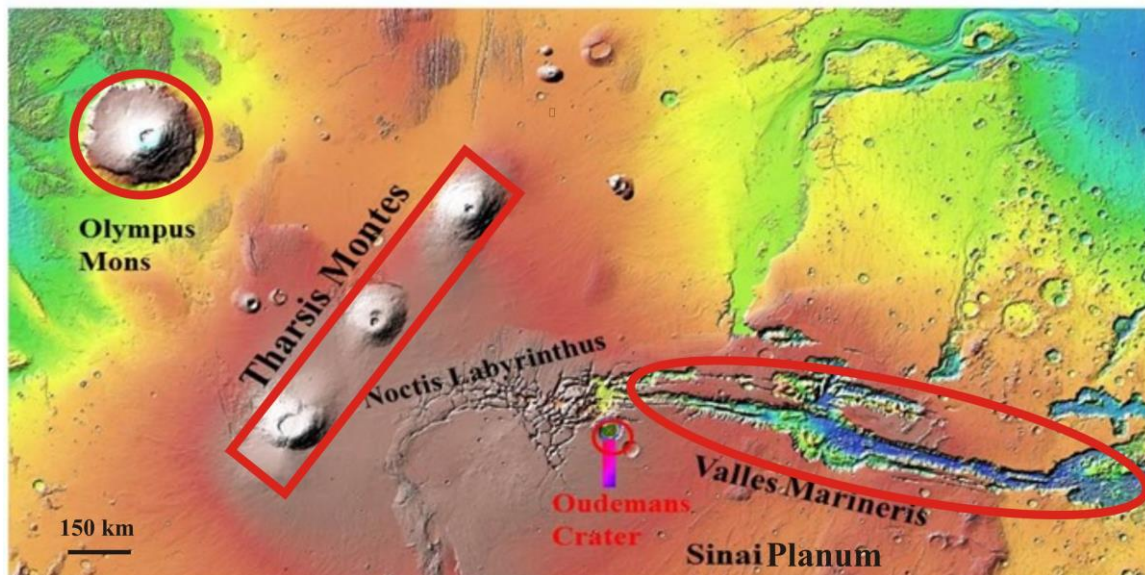


Figure 2. Part of global topographic map of Mars on MOLA shaded-relief indicating the total studied area (Oudemans Crater). Zuber@tharsis.gsfc.NASA.GOV.

Conditions on early Mars may have been similar to those on early Earth. However, landforms developed through different processes and conditions. The surface of Mars has many geological features and a complex evolutionary history that have distinguishable equivalents on Earth, including tectonics, impacts, canyons, volcanism, etc. Mars was the most active in the Noachian, although episodes of volcanic activity continued until a few Ma ago (Head et al., 2001; Neukum and Jaumann, 2004; Solomon, 2005; Tanaka et al., 1992).

Mars has a thin atmosphere with presence of volatiles and some geological processes to reshape craters (Carr, 2006). Two large volcanic provinces contain most of the erupted volcanic materials: Tharsis and Elysium. In these areas, large shield volcanoes can be observed, including the highest mountain in the solar system: Olympus Mons with 27 km elevation from zero elevation datum (Parfitt and Wilson, 2009). These large shields are the result of basaltic flows and can be compared to intra-plate volcanoes on Earth. Martian craters may be weathered by water, wind (aeolian activity) deposition, ice, and mass wasting. Gradation involves above-mentioned factors. Gravity is the driving force of gradation and the material moved by mass wasting, by running water, by icy water, or by wind. Mass wasting is a downslope movement of rock under the influence of gravity. Water in both solid and liquid form exists at depth in some regions of Mars. There are a wide range of landforms on Mars formed by running water, ice, lava, wind and mud. Volcanic activity and impacts may have disrupted ground ice and the water table resulting in release of water on Mars (Tornabene et al., 2008); (Greeley, 1994); (Harrison et al., 2010; Jones and Lineweaver, 2010). Wind is a factor for the movement of particles on Mars. So by measuring winds and observing dust storms show that the aeolian processes could be a substantial role in present-day modification of the surface (Greeley, 1994).



### 2.1.3. Martian Geological crater chronology

Tanaka (1986) proposed a chronology system for Mars. This system divides the geological history of Mars into three main time-stratigraphic units. The oldest period is called the Noachian (>3.9 Ga), followed by the Hesperian period (3.9-3.0 Ga), and by the Amazonian (3.0 Ga-present) (Fig. 3).

From ~4 Ga to ~3.9 Ga, Mars and Earth suffered extra-terrestrial events such as the Late Heavy Bombardment (LHB) (Strom et al., 2005). Some researchers have suggested most tectonic activity occurred during the Noachian such as heavy bombardment, forming the majority of Martian impact craters, valley networks and presence of surface water (Carr, 2006; Head et al., 2001; Nimmo and Tanaka, 2005; Tanaka et al., 1992). During the early Noachian, the high impact cratering, and erosion rates, had a substantial impact on the atmosphere, which decreased by a ~ 50 to 90% loss of the atmosphere (Jakosky and Phillips, 2001). Local volcanism, especially in the Tharsis region, was occurred in the Noachian period. Tanaka (1986) also indicated that high rates of volcanic and tectonic activity, erosion and weathering, fluvial, and periglacial resurfacing processes occurred in this period.

Numerical modeling showed that plate tectonics or flood volcanism have occurred during an early episode of rapid cooling ( $> 200 \text{ K} \times \text{Gyr}$ ), after which cooling mainly occurred conductively through Martian lithosphere (Van Thienen et al., 2005).

The Hesperian period is a transition between the high cratering and volcanic activity in the Noachian and the lower cratering and volcanic activity of the Amazonian (Head et al., 2001). This period is characterized by regional volcanism, glacial activity, and lava flows. During the last period (Amazonian period), volcanism, meteorite impacts, tectonics and water flow were active on a limited scale (Carr, 2006; Tanaka, 1986) (Fig. 4). However, the formation of the largest volcanic edifice, Olympus Mons, probably began during this period (Fuller and Head, 2002).

In the stagnant lid regime, there is no crustal recycling and there is no two-stage differentiation (a process of primary and secondary crust formation on terrestrial planets). Instead, melt is formed underneath the lithosphere at greater depth than with plate tectonics. Crust growth is limited by the increasing thickness of the lithosphere as the Mars cools because melt buoyancy decreases with increasing depth to the source region.

Oudemans Crater is estimated to be Late Hesperian to Early Amazonian in age based on the interpretation of the relationship of the crater with local and regional geologic units (Mest et al., 2011; Witbeck et al., 1991). Oudemans Crater has been identified as one whose formation may have caused some of the landslide deposits in Valles Marineris. Valles Marineris canyon system, a large tectonic crack affected by the rising crust in the Tharsis Bulge. The Valles Marineris canyon system's formation is tied with the Tarsis Bulge formation (Noachian to Late Hesperian period).

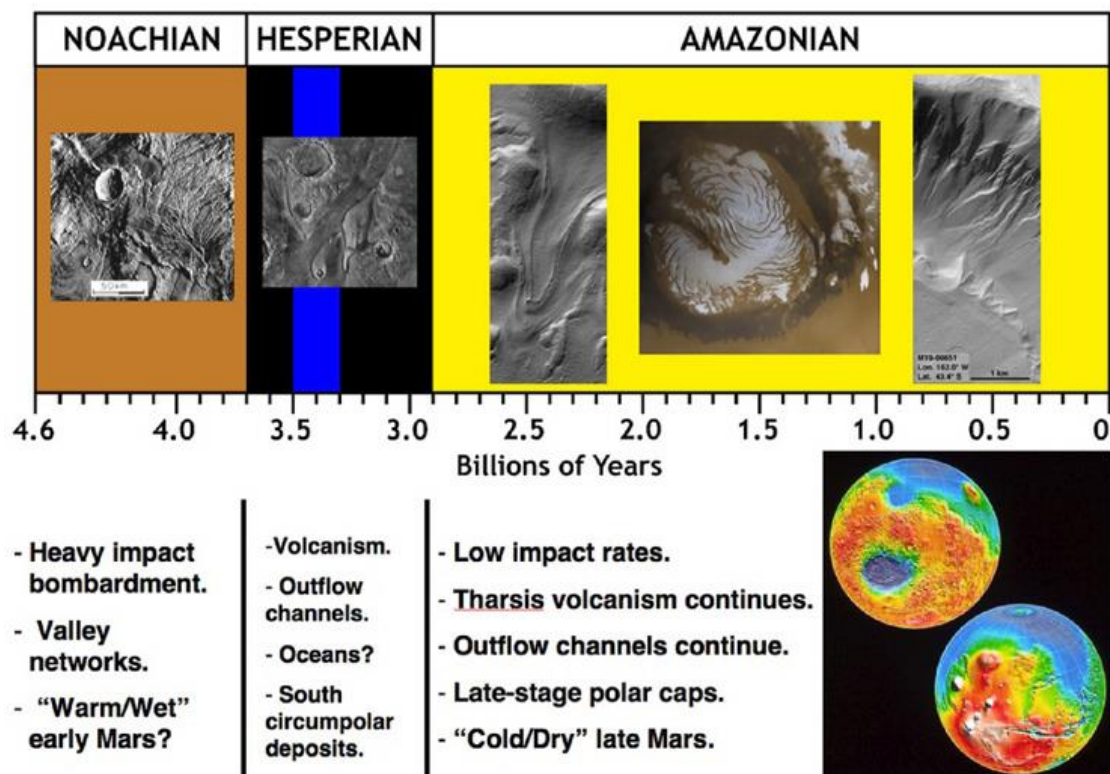
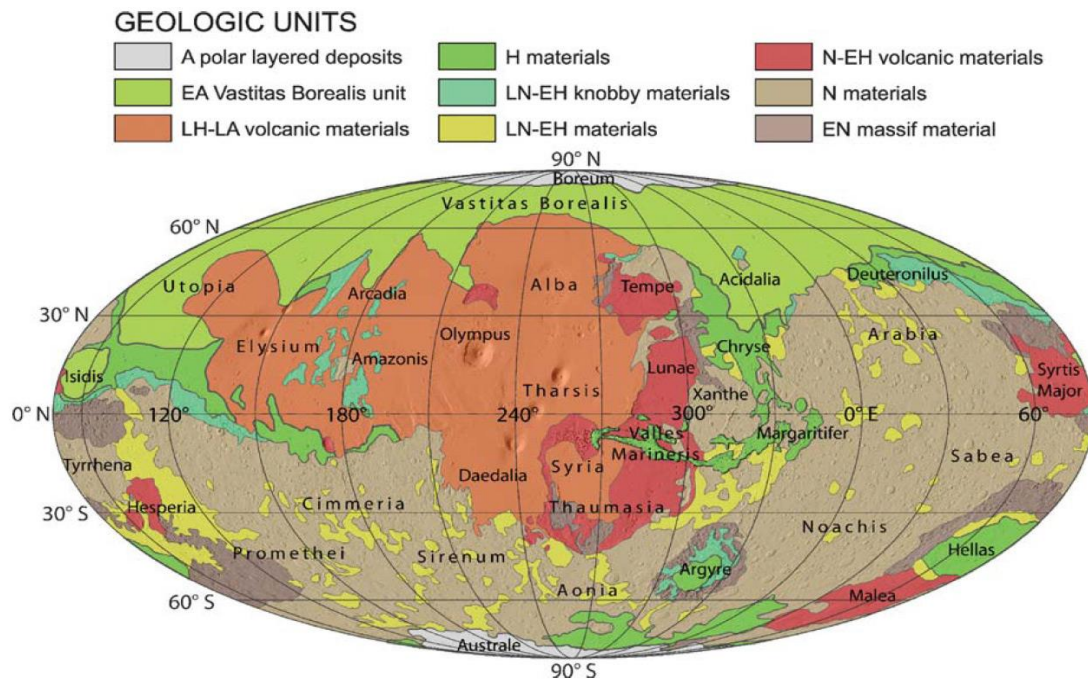


Figure 3. Mars chronology timescale system and occurred events from Tanaka et al., (1986).





**Figure 4. Global scale geological map of Mars, using mollweide projection (with east longitude and centred on 260°E) and MOLA shaded relief as background. N=Noachian, H=Hesperian, A=Amazonian, E=Early, L=Late. Map from Nimmo and Tanaka (2005).**

## 2.2. Impact crater formation

Mars is one of the best options in the planetary context to study impact craters compare to Earth with high rates of erosion, volcanic activity, and plate tectonics. Impact craters are ubiquitous landforms on the ancient surface of Mars (Melosh and Ivanov, 1999). Compared to the lunar craters, they are shallower because of erosion of rims and partial filling by windblown deposits (Greeley, 1994).

The present challenge in impact cratering studies is to use the observed morphology of extraterrestrial craters and the structure of terrestrial craters to infer the course of events during transient crater collapse. Many models have been suggested for understanding the impact crater formation (Melosh and Ivanov, 1999).

Like impact craters on Earth, many Martian craters may be difficult to identify because of erosional factors, which have modified the surface. Martian impact craters are unique

windows into the subsurface composition on Mars. (Wood et al., 1978) noted that the Mars has less basin-like craters than the Moon.

Hellas basin is the largest impact basin on Mars and in the solar system which was recognized by (Wood et al., 1978). It measures 1600 by 2000 km with a 50 to 400 km wide rim. The large Martian craters are separated by complex inter-crater plains. Most of the Martian plains are volcanic within the cratered terrain (Greeley and Spudis, 1978). The interior morphologies within basins are often modified from the effects of volcanic activity, and erosion due to continual impact bombardment on the Mars.

Three main stages lead to the formation of an impact crater deforming the surface include contact and compression, excavation and formation of transient cavity, and crater modification (Gault et al., 1968; Melosh, 1989) (Fig. 5). The following sections describe each of the impact cratering stages in more detail.

### **2.2.1. Contact and compression stage**

During the contact and compression stage, the projectile contacts the planet's surface and transfers its kinetic energy to the target rocks. Then shock waves penetrate into the target and compress it downward and outward. The projectile penetrates one to two times its diameter based on models of the impact process e.g., (Kieffer and Simonds, 1980; O'Keefe and Ahrens, 1982). High-pressure waves (shock waves) propagate both into the target and back into the projectile between the boundary of the compressed and the uncompressed target material. At this boundary, target rocks are shock vaporized and melted when they are unloaded or decompressed by rarefaction waves at high pressures ( $>100$  GPa) (Ahrens and O'Keefe, 1972; Melosh, 1989; Osinski and Pierazzo, 2013) .

The projectile may also vaporize, melt, and undergo shock metamorphism during decompression stage because of high pressure of the shocked material and passage of the rarefaction wave through the projectile (Ahrens and O'Keefe, 1972; Gault et al., 1968; Grieve et al., 1977; Melosh, 1989). Correspondingly, a zone of rock melt follows the vaporized zone, and when shock energy is dropped, rocks are damaged (fractured, brecciated) related to decreasing intensity.

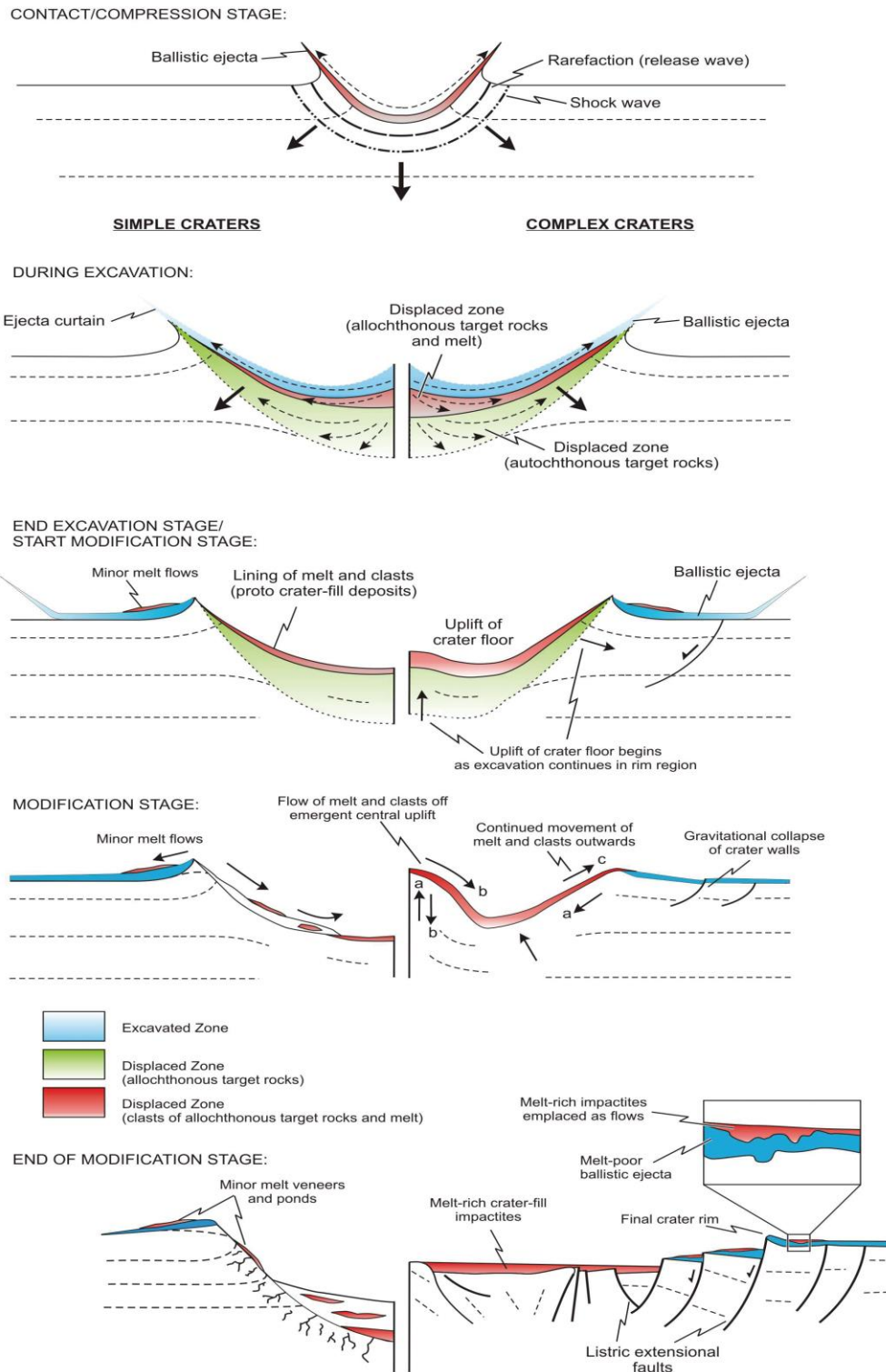


**Figure 5. Series of schematic cross-sections depicting the three main stages in the formation of impact craters. This multi-stage model accounts for melt emplacement in both simple (left panel) and complex craters (right panel). For the modification stage section, the arrows represent different time steps, labelled 'a' to 'c'. Initially the gravitational collapse of crater walls and central uplift (a) results inward movement of material. Later, melt and clasts flow off the central uplift (b). Then, there is continued movement of melt and clasts outwards once crater wall collapse has largely ceased (c). After from Osinski et al. 2011. Figure and caption from Osinski et al. 2012.**

The duration of the contact and compression stage depend on the duration of passage of rarefaction and shock waves through the projectile. When the projectile is completely unloaded contact compression transition into the excavation stage, the shock wave moving downward into the target signifies the start of the excavation stage of impact cratering formation (Melosh, 1989).

### **2.2.2. Excavation**

This stage is followed by contact and compression stage. Formation process of the transient cavity is caused by the interactions between the outward-directed shock waves and the downward-directed rarefaction waves. Both shock waves and reflected rarefaction waves spread out from the impact crater along excavation flow lines through the target (Grieve and Cintala, 1992; Melosh, 1989). Target materials move outward radially along these excavation flow lines (Melosh, 1989). The movement of rocks in the upward and outward direction results in excavation, and the formation of transient cavity (Dence, 1968). Target materials that once occupied the transient cavity are excavated and displaced.. Materials within the “excavated zone” are close to the surface as an upper zone and form the upper one-third the depth of the depth of the transient cavity (Stöffler, 1971). They are ejected beyond the crater rim, forming the ejecta blanket (Oberbeck, 1975). The ejecta consist of material from multiple shock levels because excavation flow lines intersect the pressure contours. In addition, ejecta in complex craters occur in the crater rim and interior to the final crater rim. On the other hand, highly shocked and melted allochthonous materials are driven down into the transient cavity (Grieve et al., 1977; Melosh, 1989). The velocity of the cratering flow-field can no longer excavate or displace target rock and melt. For large hypervelocity impacts on Earth, the gravity factor controls when inadequate energy remains to lift the overlying material against the force of its own weight (Anderson et al., 2004).

The transient cavity stops once the shock and rarefaction waves are no longer able to excavate or displace the target rocks (Melosh, 1989). Finally, a mixture of melt and rock debris forms a lining to the transient cavity.

### 2.2.3. Modification

During the modification stage, the transient cavity's shape has changed to form a final crater, and the most intense deformation usually occurs in the central uplift in complex craters. Modification flow is reverse of excavation flow; causes transient cavity closing. The duration of this stage depends on energy and strength of the target material. Central uplift formation is a highest degree deformation and complex process that occurs during the end of the excavation stage into the crater modification stage (Kenkmann et al., 2014; Melosh and Ivanov, 1999), where two processes occur; an inward and upward movement of large fault-bounded blocks) and a downward-directed gravitational collapse of the inner rim along concentric faults (Melosh and Ivanov, 1999; Melosh, 1989). The flow field collapses the transient cavity, and still active in some part of the crater cavity in the modification stage. The final crater expression at the end of this stage depends on the magnitude of the event. During the last part of the modification stage, bedrock of the sub-crater floor is uplifted from depth (Grieve and Therriault, 2004; Pilkington and Grieve, 1992).

The deformation formed during the modification stage, such as shear displacements occur with movements in large impact craters. Central uplifts are structurally complex and include features such as folds, which result from convergent flow, faults, fracture zones, exposure of deep bedrock, and blocks which depends the strain rate and fracture stress in size in the core of the central uplifts during the modification stage (Garvin and Frawley, 1998; Kenkmann et al., 2005; Komor et al., 1988; Larsen et al., 2009; Pike, 1980).

Central uplifts preserve morphological and structural features and provide the present-day distribution resulted by the combination of emplacement during the impact process, post impact modification, and erosion over time (Osinski and Grieve, 2013; Tornabene et al., 2012a; Tornabene et al., 2012b). As such, they are often difficult to study. Kenkmann et al, (2014) outlined the dominant mechanisms controlling the collapse of large impact craters. One model of central uplift formation (thermal weakening model) predicts that the strength of rock drops, as its temperature goes toward the melting point. Heating is an important weakening mechanism which remains in the rocks after decompression in large impacts (O'Keefe and Ahrens, 1999; Stesky et al., 1974). The other model is the block oscillation

model that impact applied a pressure in the target to oscillate as deformed blocks of rock. The last model is acoustic fluidization that explains weakening mechanism of central uplift caused by the pressure of impact within rock fragments that decrease it, allowing fluidization.

Central uplifts on Mars include floor pits and peak pits. Floor pits suggest that the target material has a significant role in affecting in central uplift morphology; however, Peak pits are depression above the central topographic rise (Barlow, 2010; Whitehead et al., 2010).

The gravity, size and target lithology of the impacted planetary body play a key role in influencing the final impact crater shape such as the crater wall collapsing (Melosh and Ivanov, 1999). Gravity also affects the driving force, size of central uplifts and the degree of slumping (Greeley, 1994). On the geologically inactive lunar surface, this complex crater form will be preserved until subsequent impact events alter it. The modification processes of uplift and collapse merge gradually into the normal processes of geological mass movement, isostatic uplift, and erosion.

An additional stage is the post-impact hydrothermal stage, in cases where water or ice may be abundant in the subsurface where these materials are heated and circulating in the structure (Kieffer and Simonds, 1980) often leading to alteration of the rocks in contact with the circulating fluids (Barnhart, 2010). Distinguishing these impact-associated hydrothermal deposits is important for understanding the climatic and geologic processes permit water on the surface. There are six locations in impact craters where hydrothermal deposits can form (Fig.6).

In summary, central uplifts allow us to investigate the early climate history and habitability of Mars (Tornabene et al., 2012b). They record structural and morphological events relating to modification and central uplift formation (Osinski and Pierazzo, 2013; Tornabene et al., 2012a). The central uplift of the complex crater is formed as the initial (transient) deep crater floor rebounds from the compressional shock of impact. Slumping of the rim further modifies and enlarges the final crater. The best locations on Mars for exposing bedrock and layered material is in central uplift (Caudill et al., 2012a; Poelchau et al., 2009).



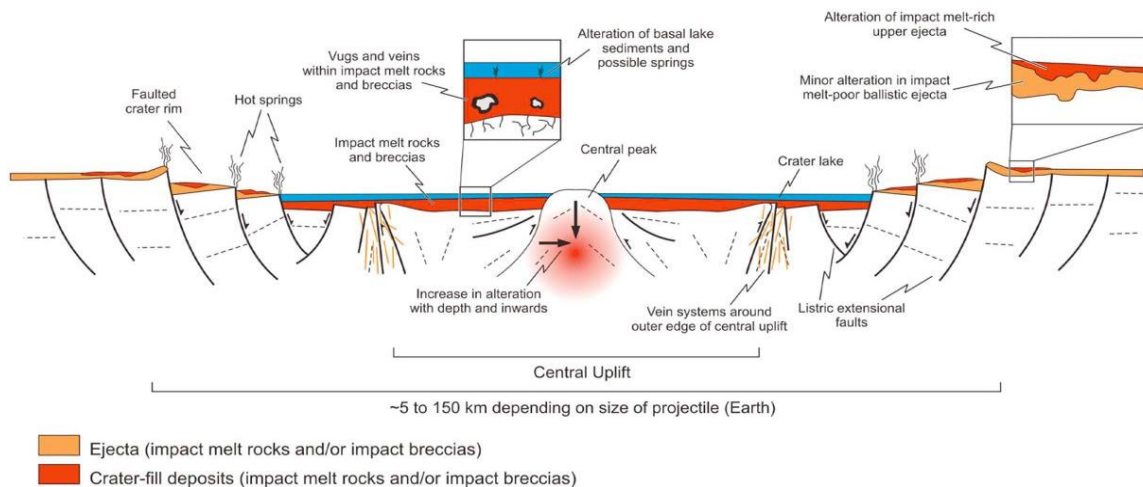


**Figure 6. Distribution of hydrothermal deposits within and around a typical complex impact crater. Modified from Osinski et al. (2012). Figure and caption from Osinski et al 2012.**

### 2.3. Impact crater morphology and morphometry

Due to the Earth's geologically active surface impact structures are often not well preserved, including their uplifts (Kenkmann et al., 2005). Weathering and erosion of the target rocks quickly alter the surface expression of impact structures; despite the crater's initial morphology, crater rims and ejecta blankets are quickly eroded and concentric ring structures can be produced or enhanced as weaker rocks of the crater floor are removed. More resistant rocks of the melt sheet may be left as plateaus overlooking the surrounding structure (Sharpton and Ward, 1990). The most complex craters on Earth are eroded to some degree, whereas they are well preserved on other planets (Turtle et al., 2005). Martian central uplifts may be well-exposed and may be readily mapped structurally and geologically in detail by using data images (Caudill et al., 2012a; Kenkmann et al., 2014; Nuhn, 2014; Quantin et al., 2012; Tornabene et al., 2012a; Tornabene et al., 2010; Wulf et al., 2012).

The morphology of craters provides useful information about the environment that the craters were formed at the time. Impact craters can be grouped into two main classes based on morphology: simple or complex (Fig. 7). Depending on the size of the transient cavity,

and the properties of the target rock, the impact crater feature can result in variable morphologies, formation of simple bowl shape cavity (simple crater) and a cavity with an interior uplift and terraced walls (complex crater) (Dence, 1968; Melosh, 1989). The transition between simple and complex craters on Mars is 5 to 10 km (Carr and Head III, 2010). Simple craters are also approximately the same size as the transient cavity, with a range of 2 to 4 km in diameter on Earth depending on target rock properties, 3 to 10 km in diameter on Mars and 15 to 20 km on the Moon (at 1/6 Earth's gravity). They are filled with breccia and impact melt deposits (Pike, 1980). They form by slumping of the transient cavity walls. The depth of the simple crater is generally 1:5 to 1:7 its diameter (Melosh, 1989; Pike, 1977). Simple craters are usually deeper than complex craters. Simple craters consist of a sharp rim with ejecta deposits and impact melts and breccias on its floor (Shoemaker, 1960). With increasing diameter, transitional craters form. They consist of shallower profile and terraced crater rim. These kinds of craters are between simple and complex craters. Transition from simple to complex craters managed by different size and gravity (Melosh, 1989; Pike, 1980). Complex craters generally have complicated structures such as uplifted rim, central uplift, flat floor, and central peak ring and continuous wall terraces (Melosh, 1989; Pike, 1980). Gravity causes the initially steep crater walls to collapse downward and inward, forming a shallower depth compared to diameter (1:10 to 1:20). The diameter depends on the surface gravity of the planet. On the other hand, complex structure produced by greater gravity and smaller diameter and brought materials from depth to the surface as a result of complex craters (Melosh, 1989; Sharpton and Ward, 1990) .



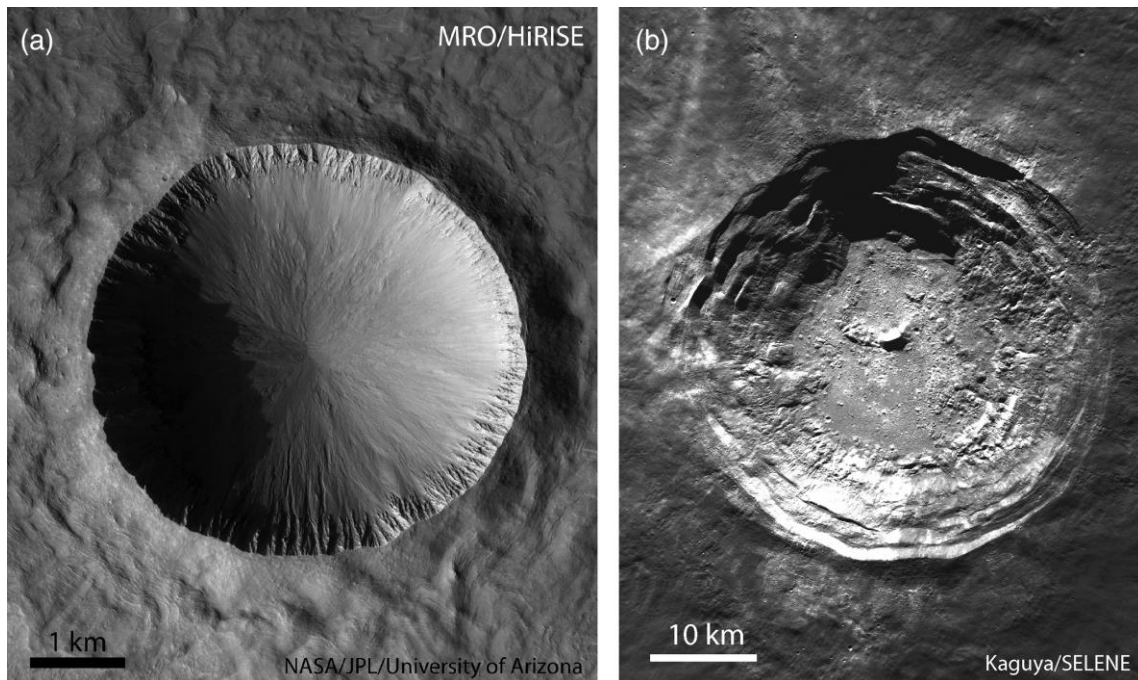


**Figure 7.** HiRISE image of an unnamed simple crater on Mars ( $38.7^{\circ}$  N/ $316.1^{\circ}$  E) displaying an elevated crater rim and steeply dipping upper cavity walls. The mid and lower parts of the wall are covered by talus deposits. Image: NASA/JPL/University of Arizona. (b) Kaguya/SELENE image (S0000001616\_1906) of the complex impact crater Aristarchus on the Moon, showing a central peak, a flat crater floor with isolated hummocks and an extensive slump terrace zone. Figure and caption from Kenkmann et al (2013).

## 2.4. Crater impactites

Impactites are produced during formation of impact structures, which include shock metamorphosed target rocks, impact breccias and impact melt deposits (Stöffler and Grieve, 2007). They are classified by observations of rocks associated with impact craters on Earth based on their physical, chemical properties and their stratigraphic setting within an impact crater (Grieve and Therriault, 2004). They are also grouped based on the extent to which they have been moved from their original pre-impact location by the cratering flow-field and the collapse of the transient cavity to create the final crater. As such, they are subdivided into two categories: 1) Parautochthonous (transported slightly out of place), and 2) Allochthonous (formed elsewhere and moved to their current location). Allochthonous impactites can be subdivided into proximal (those around the final crater) and distal (those with distance from the final crater) (Osinski and Grieve, 2013).

### **2.4.1. Impact ejecta deposits**

One of the important characteristics of impact craters is the formation of ejecta deposits. The configuration of ejecta on Martian crater is the most distinguishable among all the planets. For example lunar craters are surrounded by a continuous blanket of ejecta. The ejecta patterns around complex Martian craters are more complicated (French, 1998). With increasing the distance from the crater rim, ejecta deposits get thicker and also they become thinner with discontinuity at the outer edge (Oberbeck, 1975).

Two kinds of ejecta deposits can be observed: “Proximal” ejecta which are near the crater are continuous ejecta deposits that extend less than 5 crater radii from the rim (Stöffler and Grieve, 2007). They are made of rocks affected by different degrees of shock metamorphism and include the mixing of breccias and melt deposits (Melosh, 1989); (French, 1998). “Distal” ejecta are deposited beyond 5 crater radii from the rim. Ejecta deposits consist of shocked rock and mineral fragments, and unusual glassy object (French, 1998; Melosh, 1989).

Martian impact craters are typically surrounded by fluidized ejecta blankets. This ejecta blanket is comprised of materials ejected from the excavation that shows lobate or fluidized appearance (Barlow et al., 2000). This region (non-brecciated, melt-free) is near the rim with low shock pressures (Kieffer and Simonds, 1980). Compared with the Moon and Mercury, ejecta blankets and fields of secondary craters are less prominent on Mars. Carr (1977) proposed that material ejected from Martian craters continued to flow outward as a thin flow (continuous ejecta), while on the Moon and Earth forming hummocky ejecta close to the crater rim.

Schultz and Gault, 1979) suggested that the Martian ejecta patterns have been created by interaction of ejecta with the Martian atmosphere resulted in sorting of the ejecta. Many Martian craters, however, have ejecta deposits that appear to have flowed over the surrounding surface like mudflows. These craters are known as rampart craters, fluidized craters, or splosh craters. The final stages of ejecta emplacement involve ground-hugging flow rather than ballistic emplacement. The occurrence of rampart craters is also possible evidence for present or past subsurface ice on Mars. Rampart craters have an ejecta blanket

with a flow morphology suggesting the impact occurred onto a water or ice-rich surface (Zuber, 2001).

#### **2.4.2. Impact melt deposits**

Impact melts are one of the most characteristic features of impact events formed by the passage of shock waves and rarefaction waves through the target body at shock pressures of 50- 100 GPa (Grieve et al., 1977), causing melting of target rocks (Fig. 8). These melt deposits form a dominant part of an impact crater (Dence et al., 1977; Grieve and Cintala, 1992). During the 1960's and 1970's, many analytical and investigative studies provided observational information about impact-melted material in terrestrial impact structures (Dence, 1971; Grieve, 1975, 1978; Palme et al., 1979).

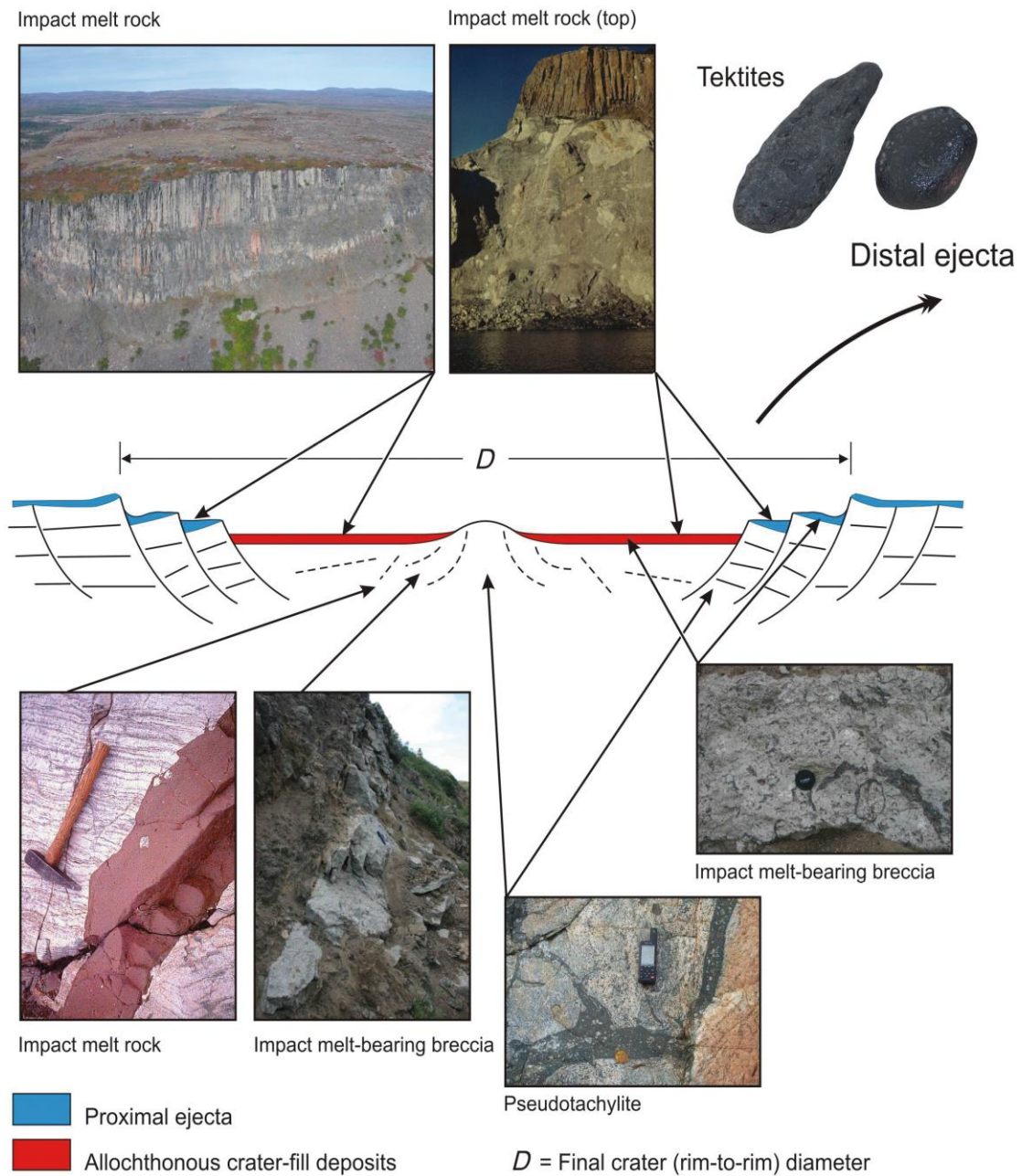


**Figure 8. Schematic diagram of a typical complex impact structure showing the main settings in which impact melt-bearing materials are typically found. Figure and caption from Osinski et al 2013.**

Depending on the cooling history of the melt rock, melt deposits can range from small glassy or crystalline fragments to large kilometre-thick coherent sheets (in large complex craters). They can be subdivided to clast-rich, clast-poor, and clast-free rocks according to their clast content (Osinski and Pierazzo, 2013). The amount of impact melt produced during an impact event depends largely on the planetary gravity, size of impact, velocity, impact angle, and rock porosities and composition of the target (Cintala and Grieve, 1998; Osinski et al., 2011). Once the magnitude of the crater event increases, the volume of melt generated also starts growing (Cintala and Grieve, 1998). Impact melt rocks derived from crystalline targets in large impact craters have a homogeneous composition compared with their original target materials (Dressler and Reimold, 2001).

Factors including the size of impactor, the angle of impact, volume of melt produced during the transient cavity, and topography can affect the locations of impact melt deposits overlying continuous ejecta.

Impact melt deposits form large ponds on crater floors (Morris et al., 2010). They are similar to morphological characteristics on Moon. Pitted materials that form based on the interaction of hot impact melt-bearing impactites with volatiles cover the surface of both Mars and Moon (Tornabene et al., 2007).

### **2.4.3. Impact breccia**

Impact breccias can be found in many different settings within impact structures; for example, in the central uplift, in crater-fill deposits, and in the ejecta blanket. They occur around, inside and below impact craters. They resulted from the zone of crater excavation and maybe highly shocked event. They fill the crater during and immediately after crater formation. The breccias fragments are typically sharp to angular. Impact breccias can be classified into two groups by the degree of mixing of different lithology (lithic breccias, and suevites) (Osinski and Grieve, 2013).



## 2.6. Geologic setting of Oudemans Crater

Oudemans Crater is a 124-km diameter crater located within the Sinai Planum region near the western end of Valles Marineris and just east of Noctis Labyrinthus (9.89 • S, 268.1 • E). This well-preserved crater lies within the Tharsis Province, a characteristic topographic “bulge”, which is a major volcanic centre on Mars. This region is comprised of extensive volcanic flood lavas, formed by hot spot volcanism (Mars; McFadden et al., 2006; Quantin et al., 2012; Wilson and Head, 2007). Furthermore, it contains the largest and most prominent volcano in the solar system, Olympus Mons (Tanaka, 1986) (Fig. 9).

These materials embay the Noachian-aged plateau materials. There is a large gap in the northern section of the crater wall because of intersection of displaced zone with deep portions of Valley system to the north. Parts of the central uplift of the crater are mantled by Aeolian deposits. On the northwestern section of the crater flow-like structures mantle other units (Mest et al., 2011).

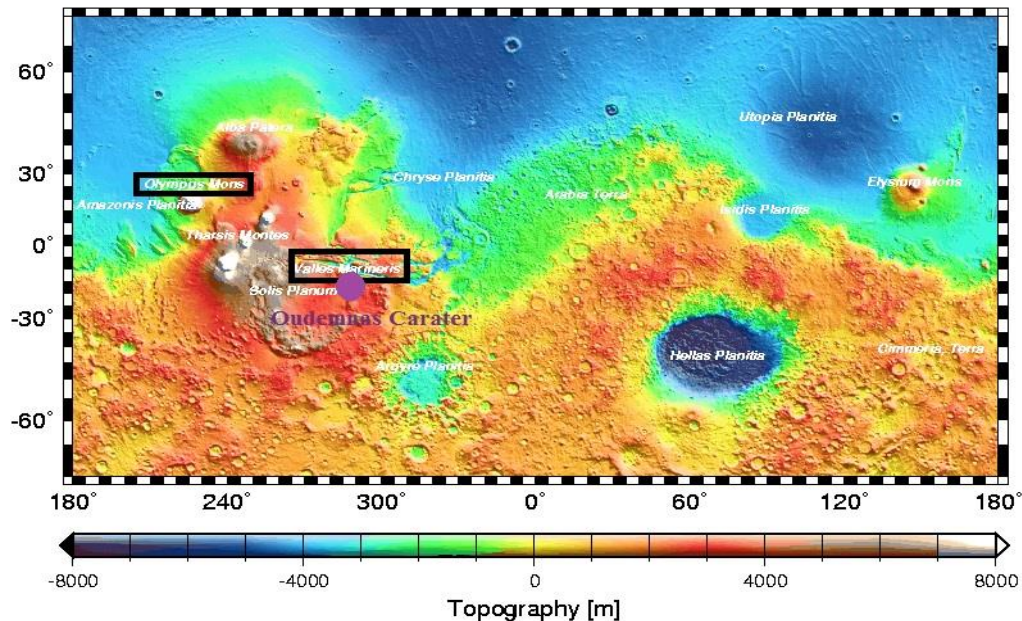


Figure 9. Location of the Oudemans crater (Purple circle) between Siani and Solis Planum on part of global topographic map (MOLA colored shaded-relief) of Mars. <http://wrgiswr.usgs.gov/open-file/of02.282/of02.282.pdf>. Zuber@tharsis.gsfc.NASA.GOV.

## **2.7 Previous work on Oudemans Crater and other Martian layered uplifts**

Layered Central uplifts are useful to analyze structural mapping as the layers are as a frame of reference from deformation (Caudill et al., 2012a; Wulf et al., 2012). Layered bedrock has been described by Tornabene et al, (2010, 2012a, 2014) as flat-lying bedrock that was reached to the surface and tilted and fractured during impact process. The concentration of layered bedrock central uplifts observed in the southwestern of Tharsis first by Tornabene et al, (2010; 2012a). Caudill et al, (2012) explained the Tharsis bulge is a volcanic layered region and almost unbroken before the excavation of an uplift by more than 20 large craters then revised to 34 craters by Tornabene et al, (2012).

In 2004, the central uplift of the Oudemans Crater was noted to contain exposed layered bedrock that is observed to be deformed and steeply-dipping in Mars Orbiter Camera (MOC) images (see [http://www.msss.com/mars\\_images/moc/2004/05/23/](http://www.msss.com/mars_images/moc/2004/05/23/)). In 2006, Bridges investigated the exposed tilted layers in Oudemans Crater using HiRISE images (e.g., Fig. 10) and CRISM observations and proposed the crater as a possible landing site for the Curiosity rover. (Mest et al., 2011) later analyzed the nature of deposits within Oudemans Crater and the deposits in Noctis Labyrinthus, which they proposed are related to the Oudemans impact. The crater possesses extended ejecta, and sharp morphologically features such as a crater rim, wall terraces, central uplift, and is interpreted to be generally well-preserved (Mest et al., 2011). He also investigated the origins of the crater, which includes Oudemans Craters' asymmetric hummocky ejecta, rim, traced walls, impact breccia, and impact melt deposits. Mest et al (2011) mentioned a large gap in the crater rim of the northwestern side. They also determined a stratigraphic uplift of ~ 7 to 11 km for the layered bedrock exposed by the central peak of the Oudemans Crater.

Tornabene et al (2010) first determined that the layers within uplifts concentrated in the Tharsis province are most consistent with pyroclastics, ash and lavas deposited during a period of voluminous volcanism and less frequent impacts. This was later studied in detail by Caudill et al (2012) and Quantin et al (2012) whom provided additional corroborative evidence for the volcanogenic origin of the layers. Tornabene et al (2010) and (Caudill et

al., 2012a) observed alternating relatively thicker light (likely representing pyroclastics) and relatively thinner dark strata (likely representing basaltic lavas).

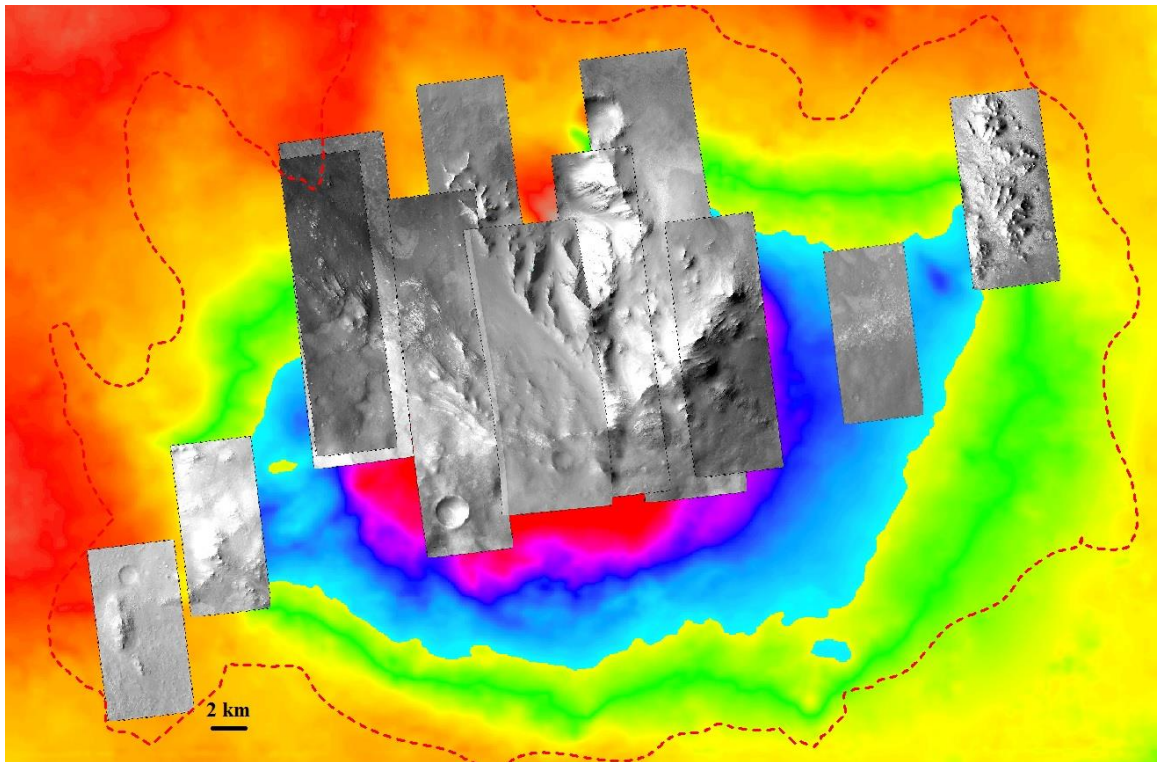


**Figure 10. Location of 11 HiRISE images used for mapping the central uplift of the Oudemans Crater overlain on the MOLA DEM based on the MOLA MEGDR data. Image: NASA/JPL/University of Arizona. Zuber@tharsis.gsfc.nasa.gov.**



### 3. Data and Methods

This section will describe the different methods used to map and analyze the central uplift of Oudemans Crater. The scale used in this study was 1:250,000. The data includes: 10 non-orthorectified High Resolution Imaging Science Experiment (HiRISE) images and 1 orthorectified HiRISE image (with pixel resolution as high as ~ 25 cm/pixel) (McEwen et al., 2010; McEwen et al., 2007) supplemented by 3 Context Camera (CTX) images (~5 m/pixel) (Malin et al., 2007) (Fig. 11); 1 High Resolution Stereo Colour Imager (HRSC) image (Fig. 12) with resolution of ~ 150 - 175 mm /pixel (Neukum and Jaumann, 2004) and 2 visible (~ 18m/pixel) and thermal infrared (~ 100m/pixel) Thermal Emission Imaging System (THEMIS IR day/night) global mosaic images (Christensen et al., 2004) (Fig. 13). These available imageries are collected from different spacecrafts and cameras; The MOLA Mission Experiment Gridded Data Record (MEGDR) (~ 462 m/pixel) (Smith et al., 2001) was examined from Mars Global Surveyor (MGS). THEMIS IR day/night achieved from Mars Odyssey spacecraft. HiRISE and CTX images come from the Mars Reconnaissance Orbiter (MRO) and the Mars Orbital Data Explorer (ODE). HRSC achieved by Planetary Data System (PDS) and (ODE) (Table 1).

The data was imported into a Geographical Information System (GIS) created using the software ESRI ArcMap v.10.1. This software is useful to execute the mapping and analysis. All images were tied to the MOLA MEGDR as a base map (Smith et al., 2001). All the images datasets were ordered descending (HiRISE, CTX, HRSC, THEMIS, and MOLA MEGDR) according to their resolution. We use these datasets to identify and classify morphologic units based on their occurrence, general morphology, texture, tonality and stratigraphic relationships to one another.

HiRISE is the most useful imagery to determine texture and the tonality of the morphologic units and impact-related morphology and structures. Utilizing the high resolution of HiRISE images, we were able to provide morphologic and structural mapping in detail, identify and analyze the fine grain morphologic and geologic units and also outline small-scale surface features, such as polygonal textures, smooth materials, and lithic clasts. The morphological and structural map created by visual interpretation of the

available images. HiRISE is also the most useful for characterizing impact-related linear features. Measuring the orientation of these linear features such as fractures, faults and dykes, but also including fold axes and the strike of bedding, provide us information regarding the deformation and structural and geological history of the central uplift of the crater. Structural data was plotted using the program Stereonet (Allmendinger et al., 2011). The CTX provides us units' relation analysis. CTX at ~ 5 meter/pixel can sometimes “fill-in” gaps in HiRISE coverage. HRSC shows location of different rock types in detail as small as 2 m) and also provide us some information related to metre-scale morphologies and textures, and THEMIS infrared (Day/night time) determine variations in physical characteristics (e.g., bedrock vs. fine-grained unconsolidated materials) based on thermal differences.

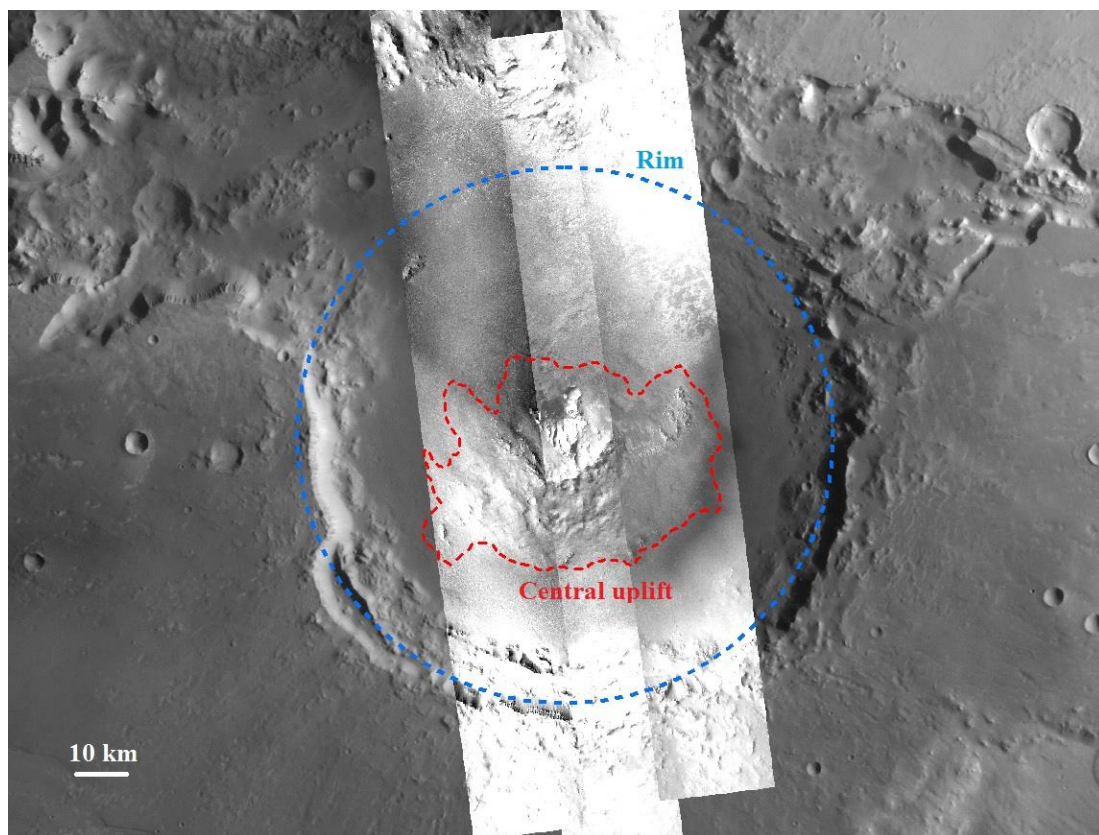


**Figure 11. Three CTX images cover central uplift of the Oudemans crater. Blue dashed circle shows rim, and red dashed smaller circle shows the Central Uplift of the Crater. P05\_003079\_1714\_XN\_08S091W, P06\_003501\_1713\_XN\_08S092W, G20\_026194\_1690\_XN\_11S091W. Image: NASA/JPL/University of Arizona.**

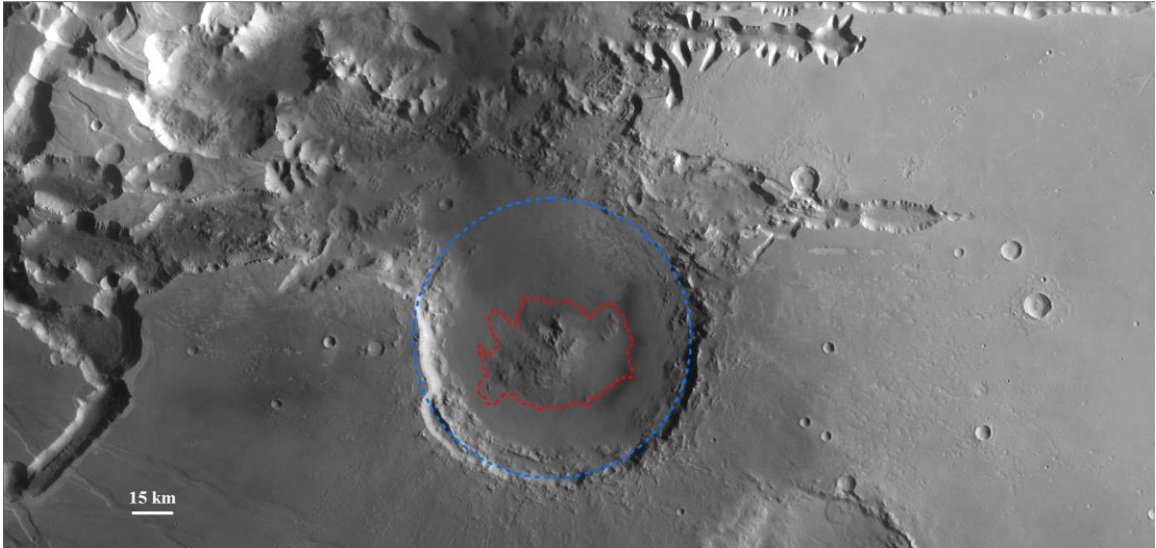


**Figure 12.** Oudemans crater on HRSC image (h0442\_0008\_nd, h2728\_0001\_nd3), Blue dashed circle shows the rim, and red dashed line shows the topographic bounds of the central uplift. Freie Universitaet Berlin and DLR Berlin, <http://hrscview.fu-berlin.de>.

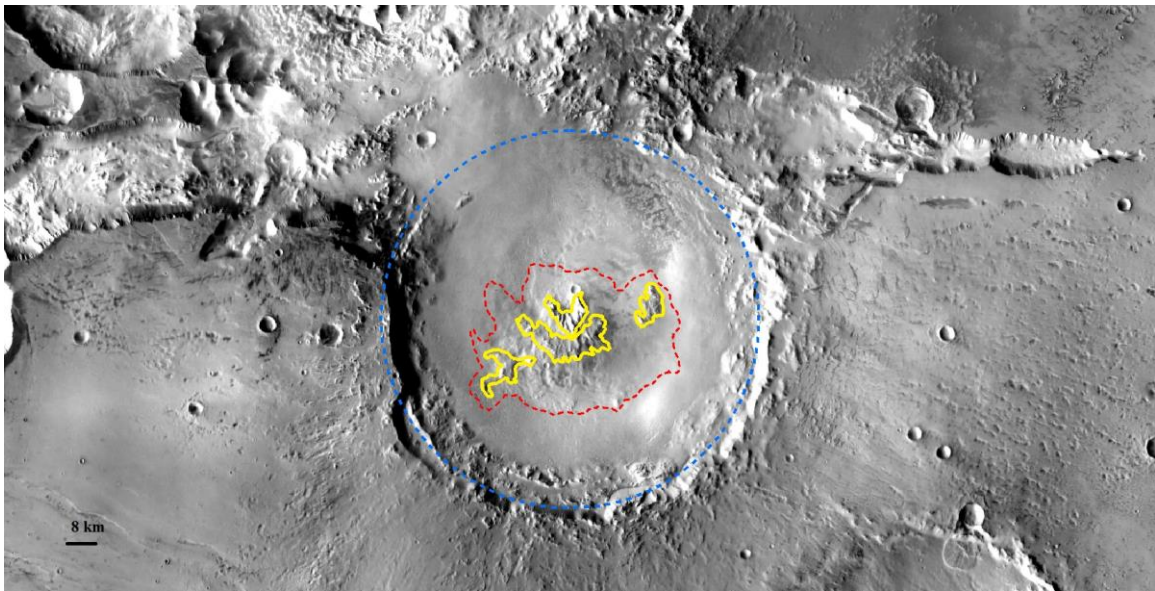


**Figure 13.** Oudemans Crater on THEMIS image. Blue circle shows the crater rim and red circle shows the central uplift of the crater, and yellow polygons show the uplifted central uplift in the core, and a gap in the northwestern part of the rim . THEMIS\_IRday\_256ppd\_West\_v2\_equirect\_clon0\_ly80. Image: NASA/JPL-Caltech/Arizona State University.

In this work, all morphological features and linear structural features were mapped in ArcGIS as polygons and polylines, respectively. The extent of the central uplift was mapped based on an observable change in slope from the crater floor to the uplift that was based off of MOLA.

Orientation (i.e., azimuth) and distances of the lineaments were exported to Excel using the option of “open the attributes” for the COGO tool in ArcView. Rose diagrams were created using data collected with the COGO tool in Arc Map to extract all the features orientation measurements and then plotted in Stereonet program. Rose diagrams are a special type of histogram for which the orientation axis is transformed into a circle to give a true angular plot. The use of the true angle conveys the orientation distribution. This projection is most often encountered in structural geology and tectonics. The rose diagram highlights the existence of orientation intervals with maximum values. The intervals with maximum values from the rose diagram can be interpreted as a major structural trend.



## 4. Results

### 4.1. Morphologic Mapping

HRSC and MOLA DTMs indicate that the topographic uplift reaches a maximum of  $\sim 2.4$  km of zero-elevation level (estimated from difference of highest elevation: 4730 m and lowest area: 2120 m). The central uplift of Oudemans Crater is, on average,  $\sim 63$  km across. It is apparent that the uplift elongated moderately in the ENE and WSW direction, and is slightly asymmetric. Importantly, the central uplift is not centred at the centre of the crater based on drawing a best-fit circle, so we can observe an asymmetry of the uplift as well. In the other words, there is a lack of uplift on the north -side of the crater. Based on MOLA and HRSC, the central uplift was divided into 4 regions based on the main topographic expressions in the uplift region with the central region then being divided into two regions based on the different textures of the materials (Fig. 14).

The central uplift of the Oudemans Crater was divided into five general morphologic units: 1) Bedrock; 2) Megabreccia; 3) Clast-rich dark-toned unit; 4) Smooth and Pitted unit; and 5) Erosional deposits (which can be further subdivided into a Mass wasting unit and Aeolian deposits unit) (Fig. 15).

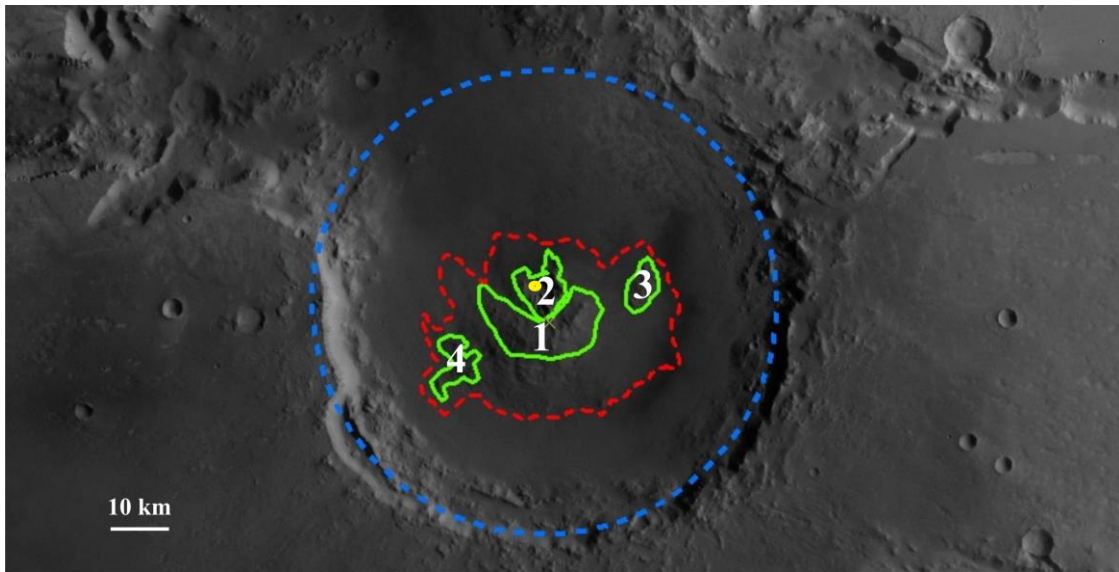
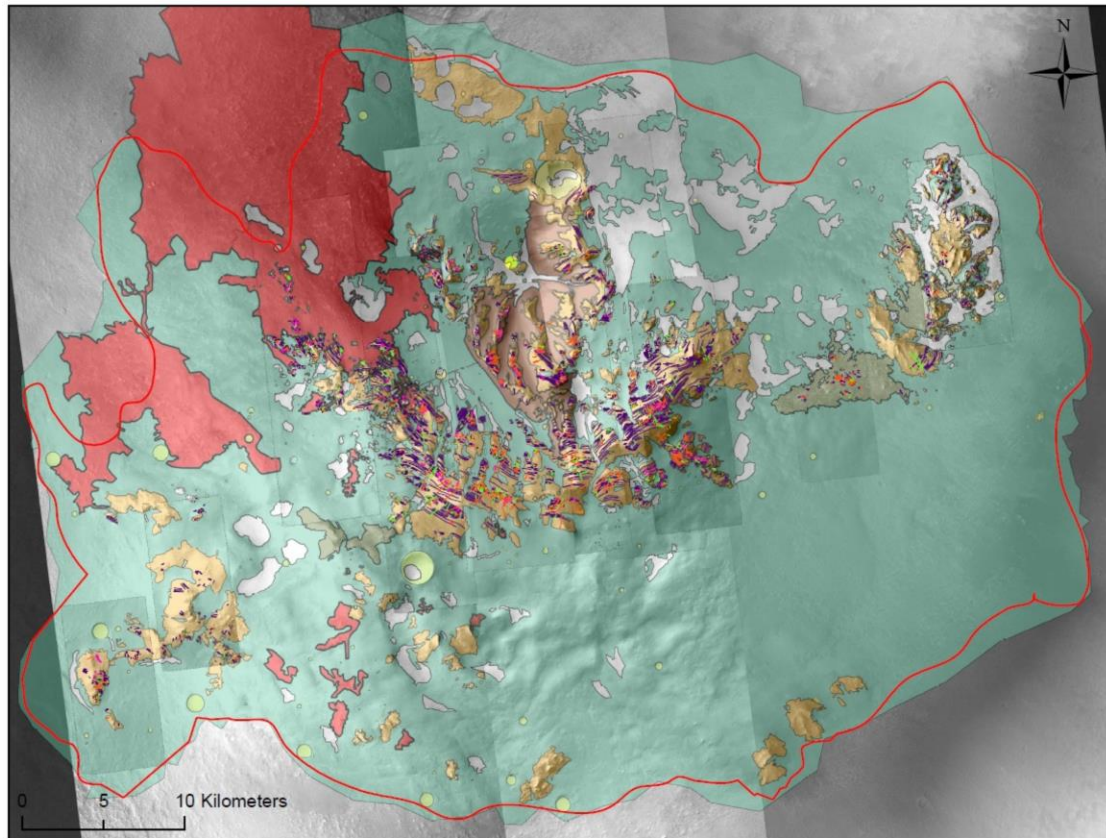


**Figure 14.** Exposed bedrock unit named region 1, and undivided outcrops named regions 2, 3, and 4 on HRSC on h2728\_0001\_nd3. img. The centre of the crater marked by a yellow circle and central uplift is limit by a red dashed line. Image: Freie Universitaet Berlin and DLR Berlin, <http://HRSCview.fu-berlin.de>.



### Legend

- Central uplift
- Dyke
- Faults
- Fractures
- Bedding
- Small craters
- Aeolian deposits
- Bedrock
- Clast-rich dark-toned unit
- Smooth and pitted materials
- Mass wasting
- Megabreccias

**Figure 15. Geomorphological and structural map of the Oudemans Crater central uplift.**

#### **4.1.1. Unit 1: Bedrock**

The exposed bedrock unit of the mapped area was subdivided into two subtypes; 1a- Layered Bedrock, 1b- Undivided Bedrock. The transition from layered to undivided units is gradational in some parts of the area and sharp in some others, and is easy to characterize by a distinct change in surface morphology. The undivided bedrock occurs in the eastern, northern, and southwestern portions of the central uplift (See green polygons No 2, 3, and 4 in Fig. 14) and will be further discussed below.

##### **4.1.1.1. Unit 1a) Well-bedded Layered Bedrock**

Based on HiRISE and CTX, the layered bedrock consists of light and dark-toned layers covering by erosional deposits in some part of the central uplift. In this region of the crater, the layered bedrock is present as a relatively extensive curved-shape zone that comprises ~ 15% of the topographic expression of the central uplift (Fig. 17). The layered bedrock consists of packets of alternating light-and dark-toned layers (possibly megablocks) within the central uplift and is consistent with previous observations (Bridges, 2006; Caudill et al., 2012a; Nuhn, 2014; Tornabene et al., 2012a; Tornabene et al., 2010; Wulf et al., 2012) (Fig. 16). The majority of exposed layered bedrock is observed in section 1 of the central uplift (Fig. 14). This unit occurs in the outer to central region of the central uplift (between ~11 km and 26 km).

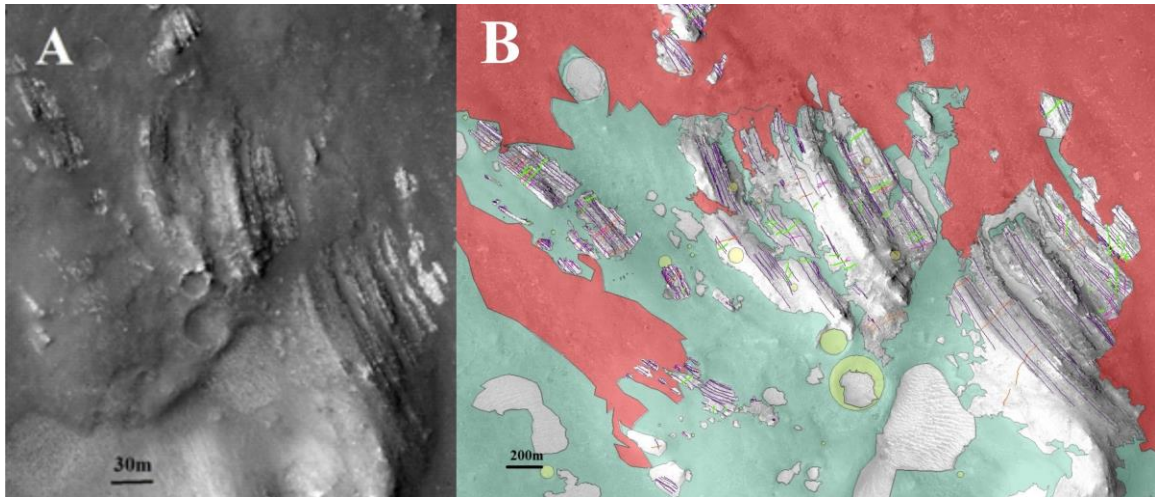


**Figure 16.** Area A in unit 1a shows layered bedrock in the western part of the central uplift (DTM sdx on ESP\_028449\_1700\_RED\_A\_01\_ORTHO), and area B mapped HiRISE image (ESP\_011676\_1700\_RED). Image: NASA/JPL/University of Arizona. Layered bedrock surrounded by some units such as dark-toned clast-rich showed by red and smooth and pitted materials by green, and covered in some part by Aeolian deposits in light grey.

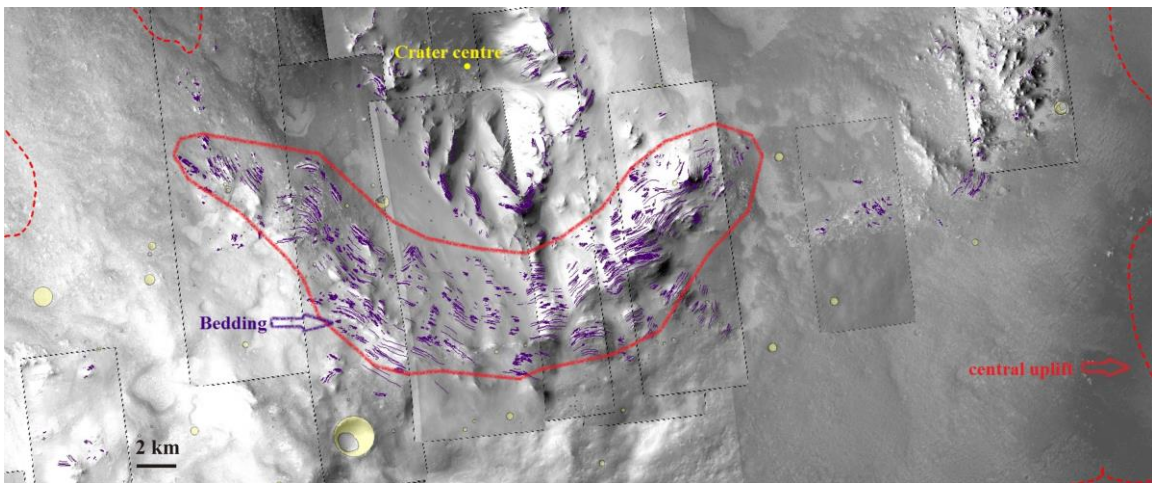


**Figure 17.** This image shows layered bedrock outlined by the red polygon in the centre. Bedding is shown by the purple lines. Image: NASA/JPL/University of Arizona.



#### **4.1.1.2. (Unit 1b) Undivided Bedrock**

This unit covers the northern, eastern, and southwestern parts of the central uplift (sub-regions 2, 3, 4) (Fig. 14). This unit shows coated and obscured bedrock and fractured outcrops with no obvious layering. This unit forms high slopes and ridges. This unit comprises less than 10% of the uplift (Fig. 18).

#### **4.1.2. Unit 2: Megabreccia**

In a limited part of the central uplift, there are several regions that display some large (>50 m) light-toned angular and sub angular clasts set within a dark-toned fine-grained matrix. The best expression of Megabreccia unit is in the eastern part of the uplift, but is also found in the southwestern section. We can observe relatively large clasts (i.e., megaclasts) within this unit (Fig. 19), which is one of its defining characteristics distinguishing it from Unit 3 (described below). This unit covers less than 5% of the total area. This unit shows different size and colour of clasts on HiRISE and CTX. The size of the megaclasts ranges from ~50 to 500 m.

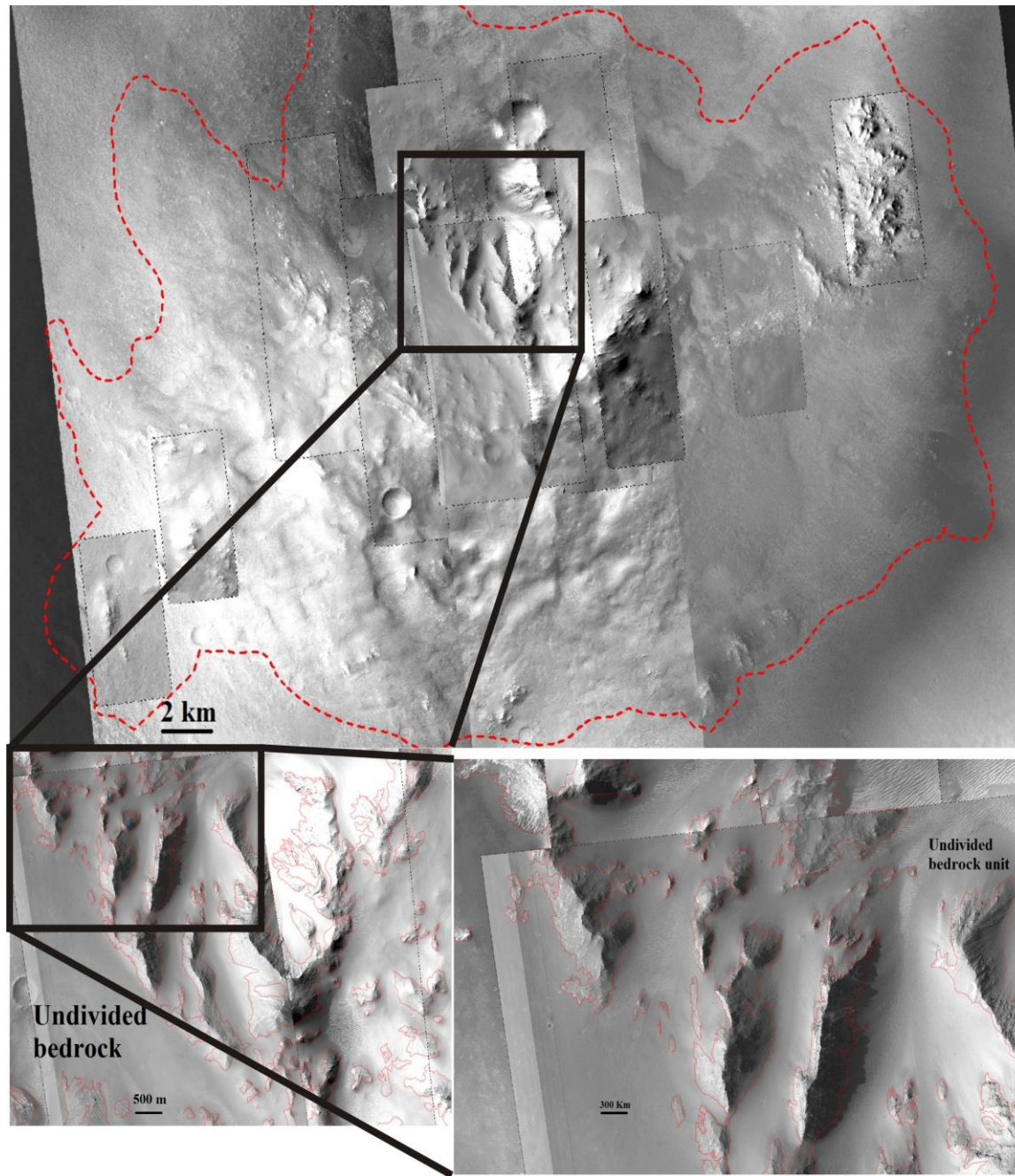


**Figure 18. Light brown polygons outline coated bedrock with a lack of layering (Undivided bedrock). The base image comprises part of four HiRISE images, PSP\_002446\_1700\_RED, ESP\_026194\_1700\_RED, ESP\_027117\_1700\_RED, ESP\_026273\_1700\_RED. Image: NASA/JPL/University of Arizona.**



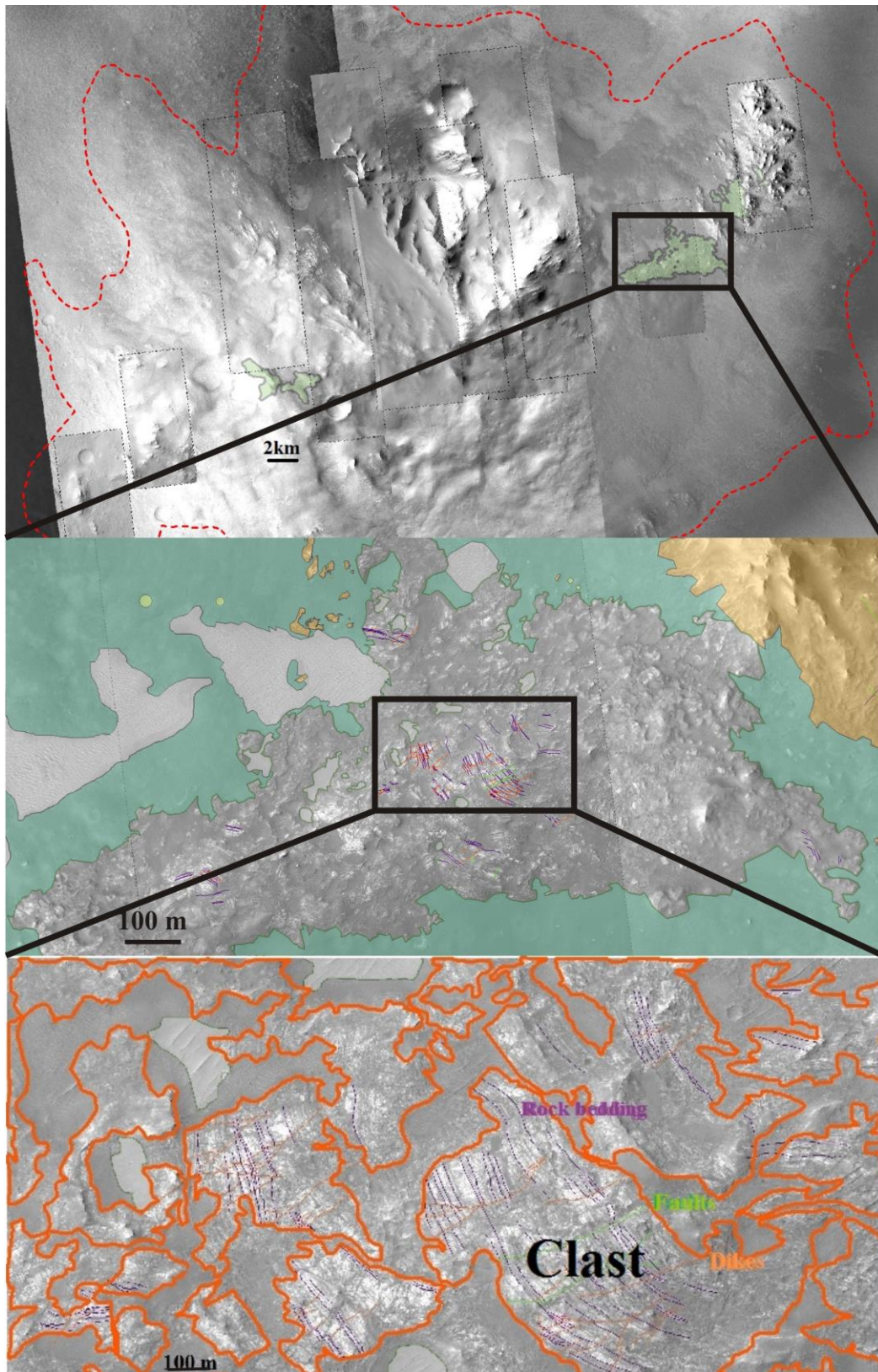


**Figure 19. Impact megabreccia showing layered megabreccia with different size of clasts, all clasts outlined with orange polygons. Part of HiRISE image ESP\_036176\_1700\_RED. Image: NASA/JPL/University of Arizona.**

#### 4.1.3. Unit 3: Fine-grained clast-rich and poor unit

This unit comprises a dark, fine-grained material with generally smooth texture and is divided into two sub-types; clast-rich and clast-poor. This unit occupies 10% of the total area and is mostly located in the western outer part of the central uplift, and surrounding by outcrops units and continuing toward the western sector of the rim (Fig. 20).

This unit forms coatings and flows on low slopes. This unit contains variable amounts of light-toned clasts which are smaller than those on Megabreccia. Melting might cause lessen strength of block contacts during the modification stage (Dence et al., 1977).

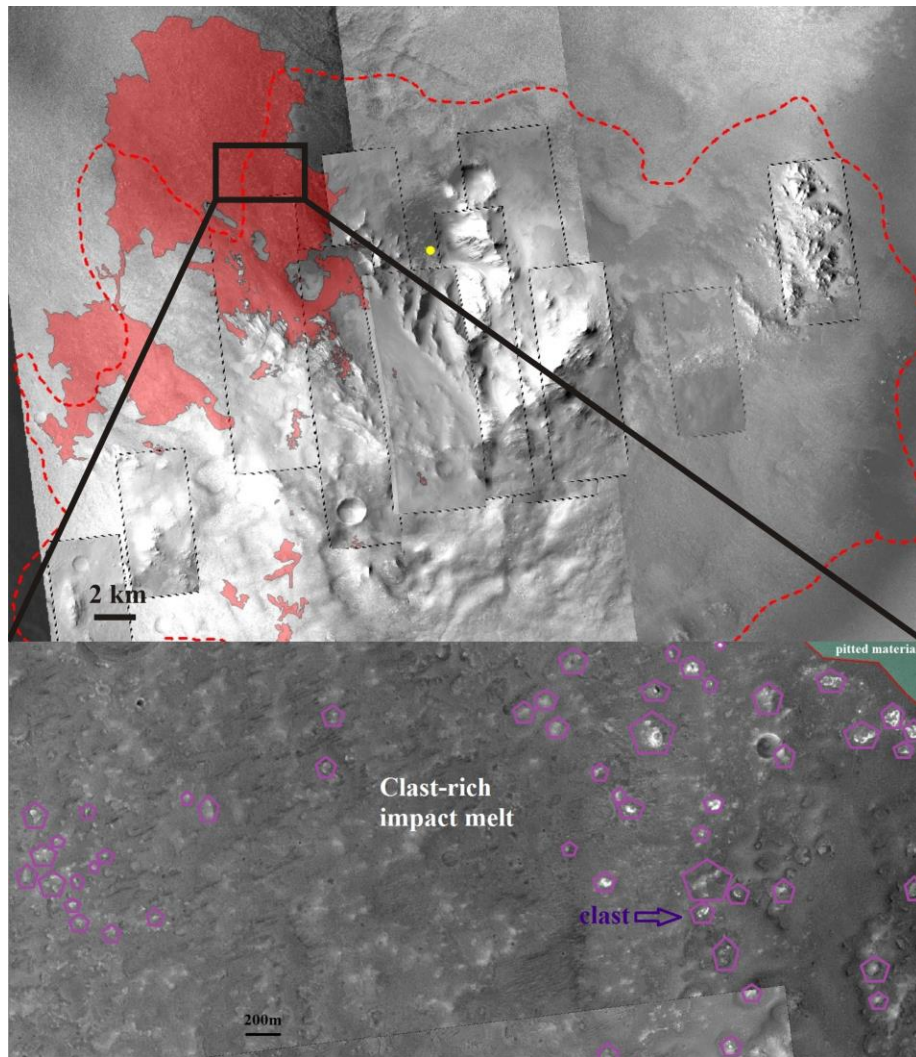


**Figure 20. Dark-toned clast-rich impact dark-toned unit in the western portion of the Oudemans Crater on HiRISE and CTX images ESP\_011676\_1700\_RED. Larger clasts are showed by light purple polygons in this unit. Image: NASA/JPL/University of Arizona.**



#### 4.1.4. Unit 4: Smooth and pitted material

In HiRISE and CTX images, large contiguous smooth and pitted dark and light-toned areas can be seen in grey color. This unit appears to coat, embay and surround the majority of the central uplift, and covers more than 40% of the mapped area (Fig. 21). The floor of Oudemans Crater is covered by a mottled deposit that extends across the whole area of the crater (Mest et al., 2011). These areas show distinct surface morphologies and cover much of the floor of Oudemans Crater. This dark-toned portion consists of a relatively high density of shallow pits, while the lighter areas show generally smoother surfaces. Around the central uplift of the crater, large plains composed of dark materials can be seen.

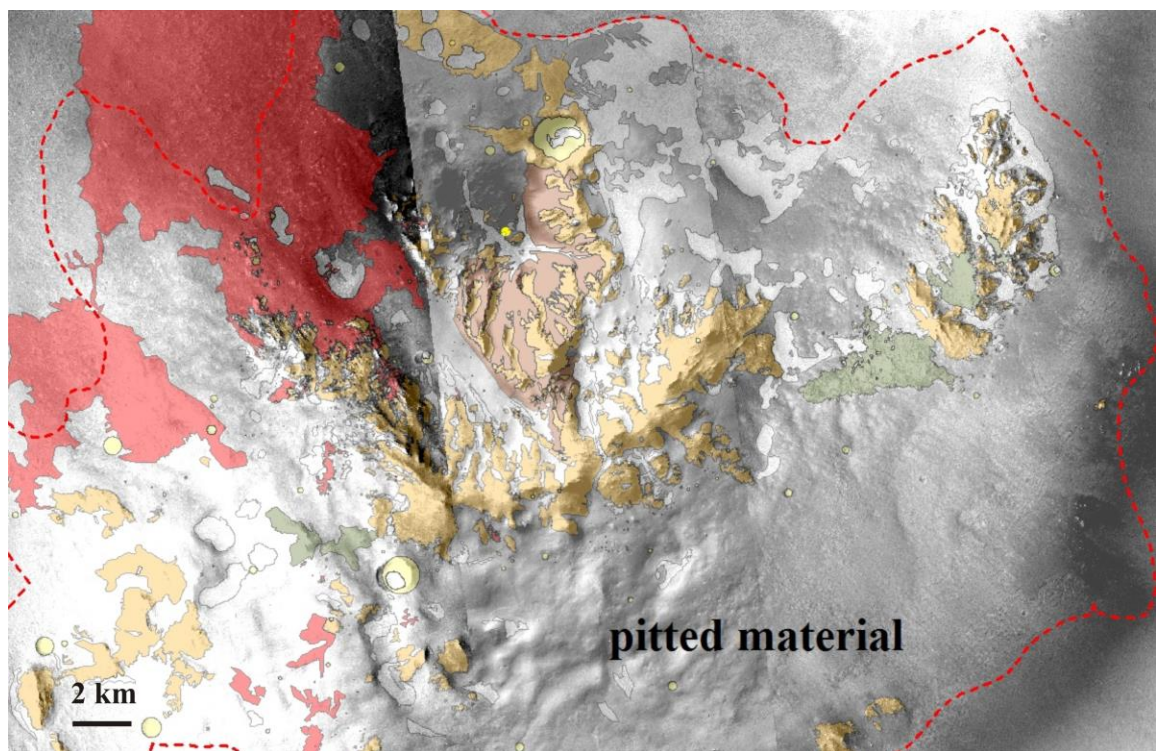
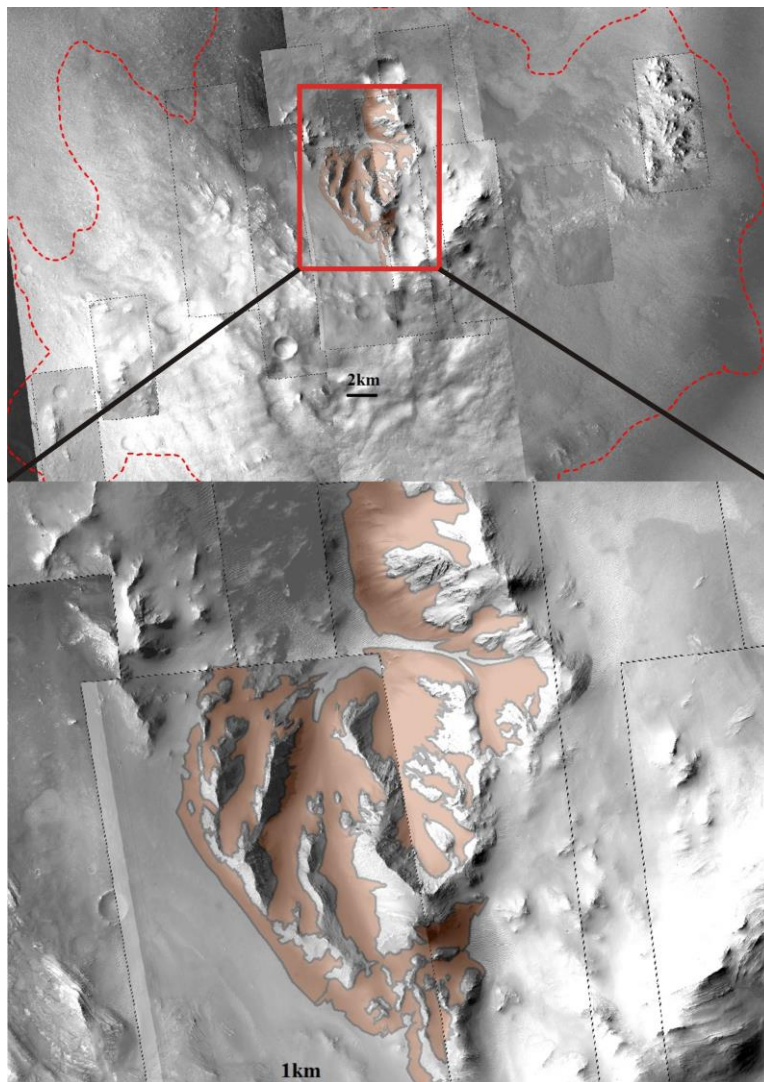


Figure 21. Dark-toned and light-toned pit unit seen in grey colour in most part of the area in the central uplift on CTX imagery. P05\_003079\_1714\_XN\_08S091W\_final.tif, P06\_003501\_1713\_XN\_08S092W\_final.tif, G20\_026194\_1690\_XN\_11S091W\_final.tif. Image: NASA/JPL/University of Arizona.

#### 4.1.5. Unit 5: Mass wasting

This unit represents a contiguous and relatively uniform-toned unit grading from smooth to granular (i.e., containing sporadic meter-sized boulders). It is observed on low slopes associated with the highest slopes within the northern core of the central uplift. It is also associated with alcove and valleys situated in this region. This unit appears to superimpose some of the bedrock with northern core of the central uplift (Fig. 22). This unit has 10% Coverage of the uplift.



**Figure 22. Mass wasting unit observed in the northern and central part of the central uplift. HiRISE image PSP\_002446\_1700\_RED and ESP\_026194\_1700\_RED. Image: NASA/JPL/University of Arizona.**

#### 4.1.6. Unit 6: Aeolian deposits

This unit is comprised predominately of linear deposits (trending NE-SW), which shows aeolian bedforms. We observed with THEMIS IR that orientations ( $\sim 45^\circ$ -  $75^\circ$ ) seem to related to the wind direction streaks at the time of their last migration. This unit is found throughout all the mapping area (Fig. 23). It is found within depressions and other low-lying areas throughout the structure, and can be readily observed partially covering the bedrock, smooth and pitted materials, megabreccias and both the clast-rich and clast poor dark-toned units. These units show low elevation related to other surrounding units. This unit has 10% Coverage of the uplift.

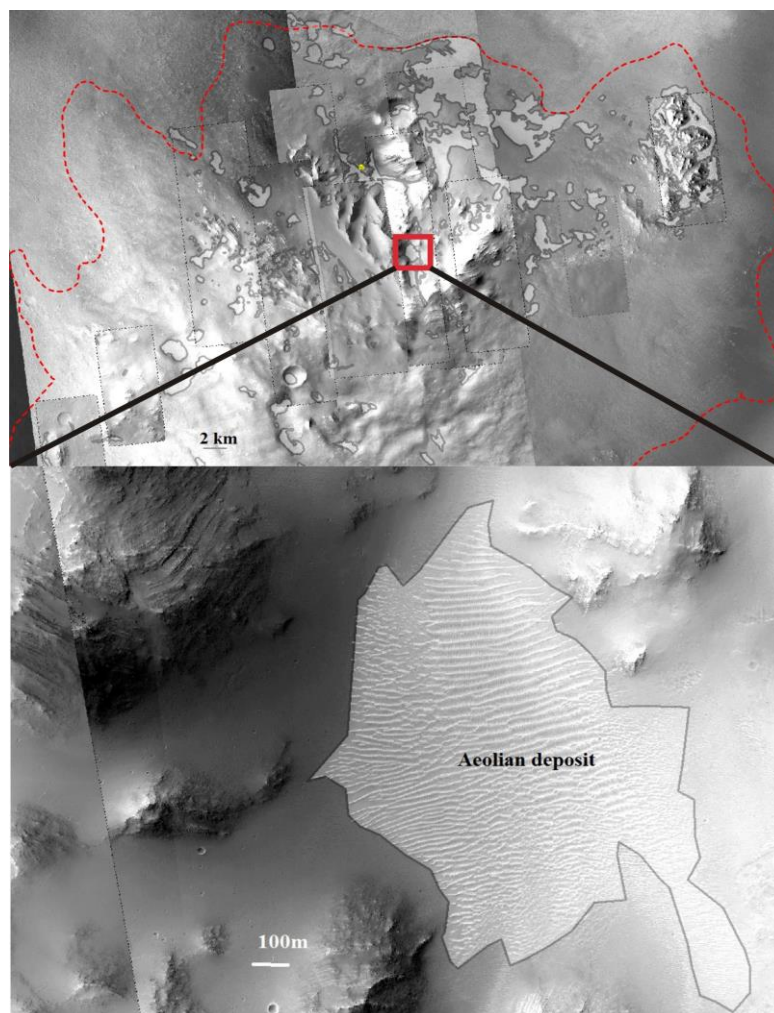


**Figure 23. Aeolian deposits seen mostly in the northern of the Crater, HiRISE image ESP\_026194\_1700. Image: NASA/JPL/University of Arizona.**



## 4.2. Structural Mapping

Using HiRISE four structural features were observed within the layered bedrock unit of the central uplift: fractures, faults, dykes and folds. Any linear discontinuities within a layer of rocks lacking offset and an observable thickness (i.e., infilled materials) are defined as fractures. Faults are defined as any observable displacement or offset that shift layers, dykes, folds, and megablocks (Fig. 24). Normal faults demonstrate crustal extension of large spatial extent with observe displacement. Thrust faults occur as spatially extensive sets; both as surface breaking faults and as blind thrust faults topped by forced fault propagation folds (wrinkle ridges) at the planetary surface. Strike-slip faults define localized arrays of distributed horizontal shear strain. Dykes are filled fractures by some applied stress and pressure to the bedding of a layers rock cut across the other types of layered rock bedding with different angle (Marshak, 2009). The thickness of the dykes ranges from several metres to ~100m. Rose diagrams were created to determine the possible presence of preferred orientations. The angle between the lineament and a line through the lineament mid-point is zero so the lineament seems to be radial to the location. For analyzing the dykes, faults, and fractures, we divided our region to 6 different parts named A to F (based on the areas with the most abundant and well-exposed linear features to least) to measure their orientation, and interpret them by plotting them in a rose diagram plot.

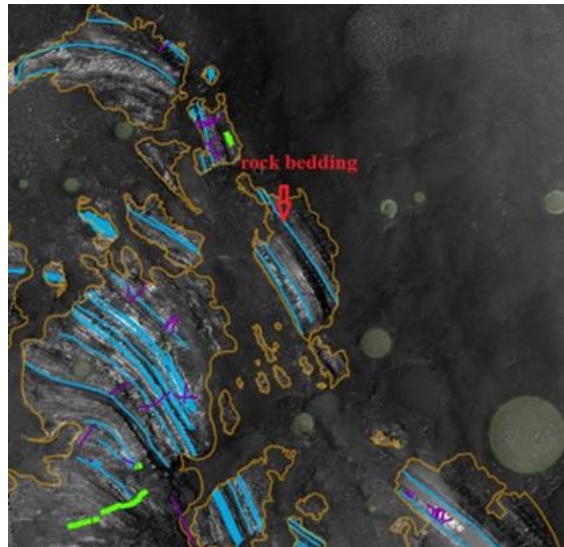


**Figure 24. Mapped HiRISE image ESP\_027882\_1700\_RED, showing tilted layers in blue colour. Image: NASA/JPL/University of Arizona.**



### 4.2.1 Fractures

We found the highest density of fractures in the central regions of the central uplift especially where the layered bedrock is the best-exposed (Fig. 25). We measured the orientations of 61 fractures in six categorized parts in our mapped area, and then plotted in a rose diagram (Fig. 26). They are distributed radially about the centre of the central uplift. Fractures in the layered bedrock in the west are typically oriented NE- SW, with a SSE- NNW trend in the eastern - part of the central uplift.

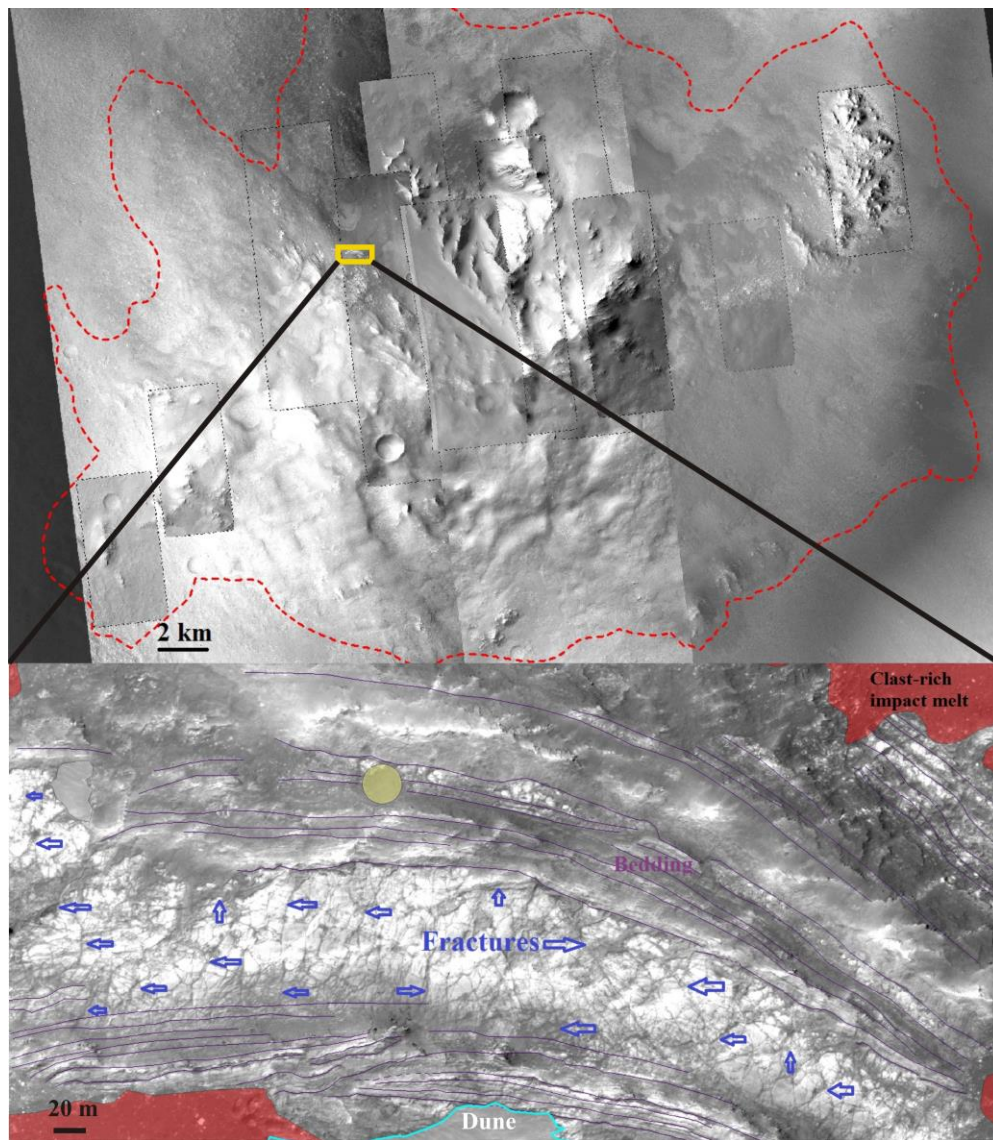


Figure 25. Close up of fractures in bedrock. Portion of HiRISE image, ESP\_027882\_1700\_RED. Image: NASA/JPL/University of Arizona

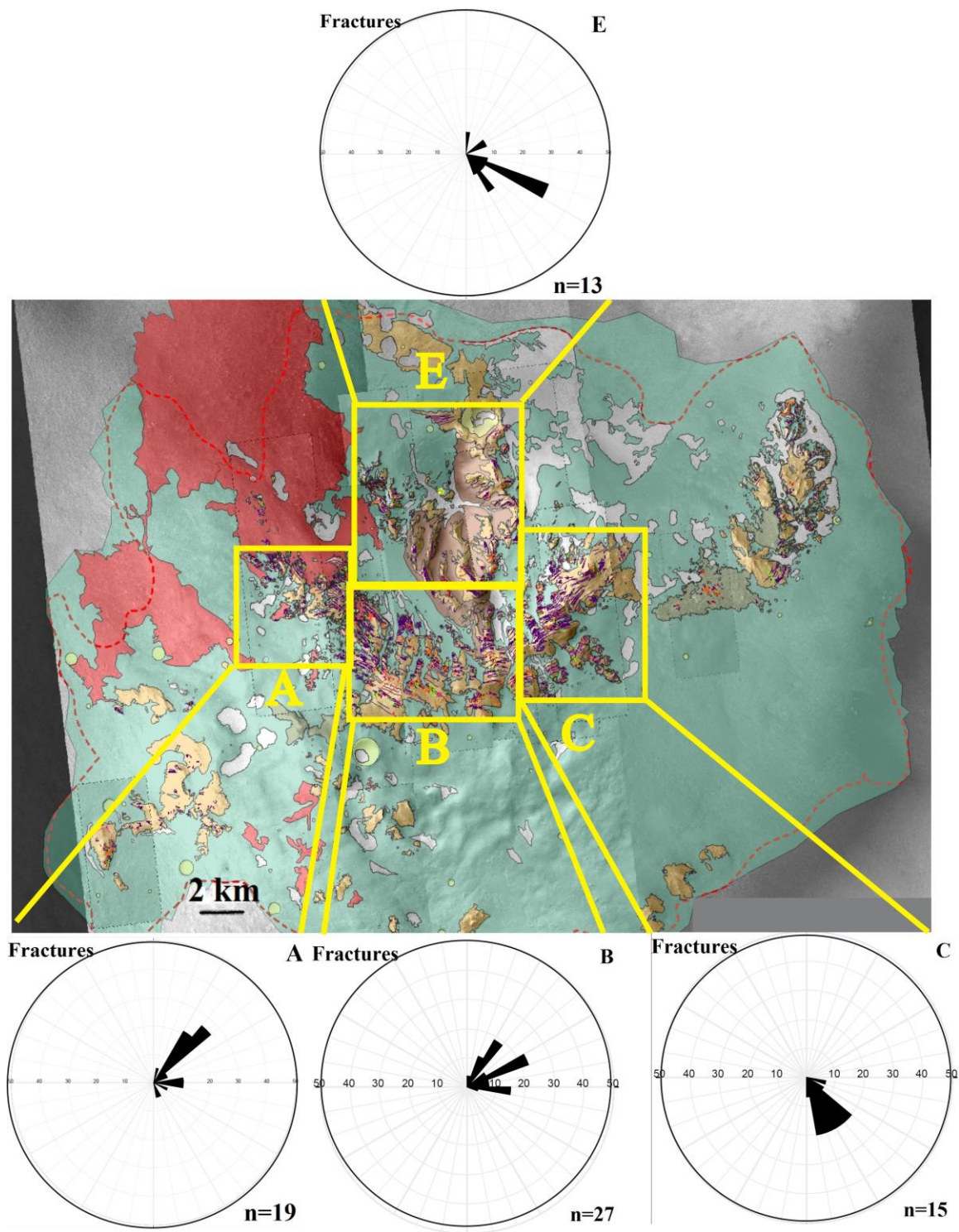
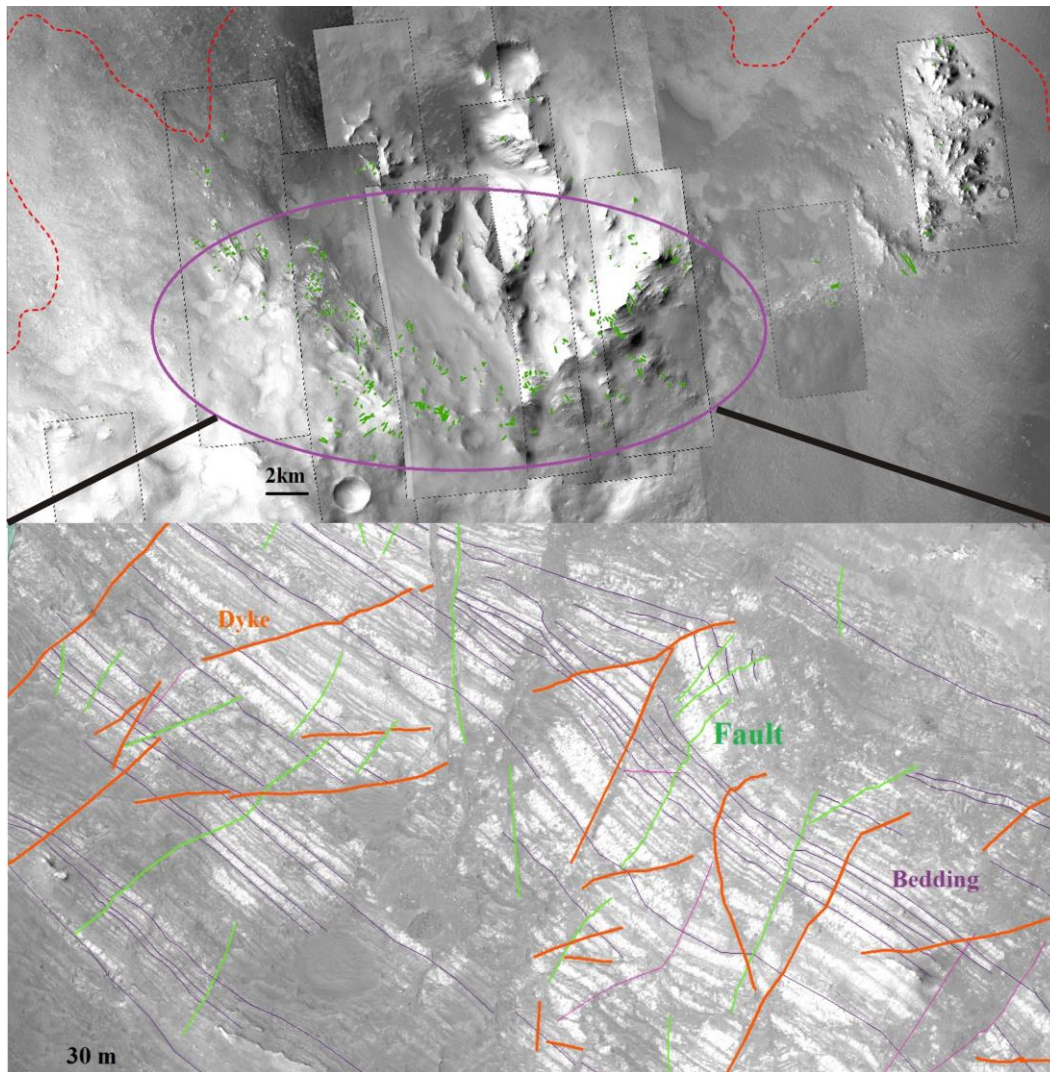


Figure 26. Rose diagram of fracture trend. Image: NASA/JPL/University of Arizona.



#### 4.2.2. Faults

Within the exposures of layered bedrock, there are very apparent offsets (“Observed”) and some areas where faulting is inferred (“Inferred”) (Fig. 27). The orientation of the 133 main faults was measured. The faults are also mostly distributed and oriented radially and sometimes concentrically around the centre of the crater. Area A shows a preferred SW - NE trend in the western part of the uplift, while the eastern part (areas C and D) show opposite direction (SE -NW, S -N). In addition, centre of the uplift (Area B) shows E - W trend (Fig. 28).



**Figure 27.** This image shows displacements across faults with high distribution toward centre of the Central uplift, faults seen by green lines, PSP\_002446\_1700\_RED.  
Image: NASA/JPL/University of Arizona.

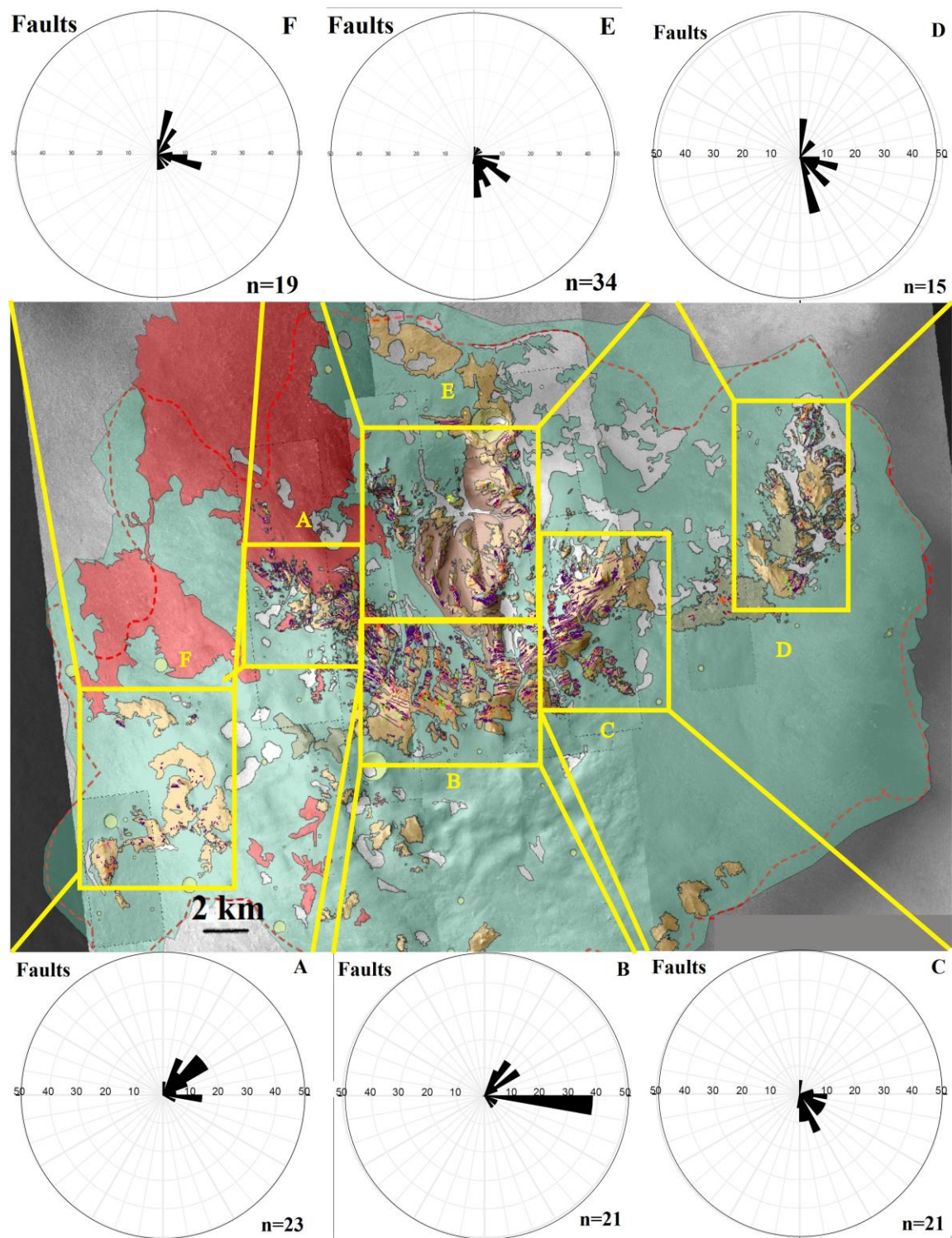


**Figure 28.** This image shows rose diagram of faults in six divided sections. Image: NASA/JPL/University of Arizona.

### 4.2.3. Folds

Folds are curved and bent as a result of permanent deformation. They are commonly formed by shortening of existing layers, but may be formed as a result of displacement on a fault in both extensional and thrust faulting (fault bend fold). Within the exposed layered bedrock we observed four large (~ 600m – 2 km) concentric folds (A, B, C, D) located toward the centre of the uplift (showing increased deformation); three (A, C, and D) open (~ 70°-120° from the limb) and one (B) close (~70° from the limb). They appear to be displaced, offset and bounded by faults (Fig. 29). Folds A, B, and C are located in layered bedrock unit, while Fold D is located in the fractured unit. Fold B that looks a fault bend fold, occurred in extensional and thrust faulting, seems to be asymmetrical and other ones (A, C, and D) are symmetrical. Figure 30 displays a close up of a fold B (~ 2.5 km). It is located toward the centre of the central uplift and is asymmetrical and a close fold (~70 inter limb angle). This fold is apparently bounded by a fault on the right limb. The right limb appears to be detached into blocks. Fold formation is accommodated by fracturing. The western part of the central uplift is dominated by two km-scale folds with NNE –SSW trending axial planes and the eastern part is contained two folds with NW -SE trending axial planes.



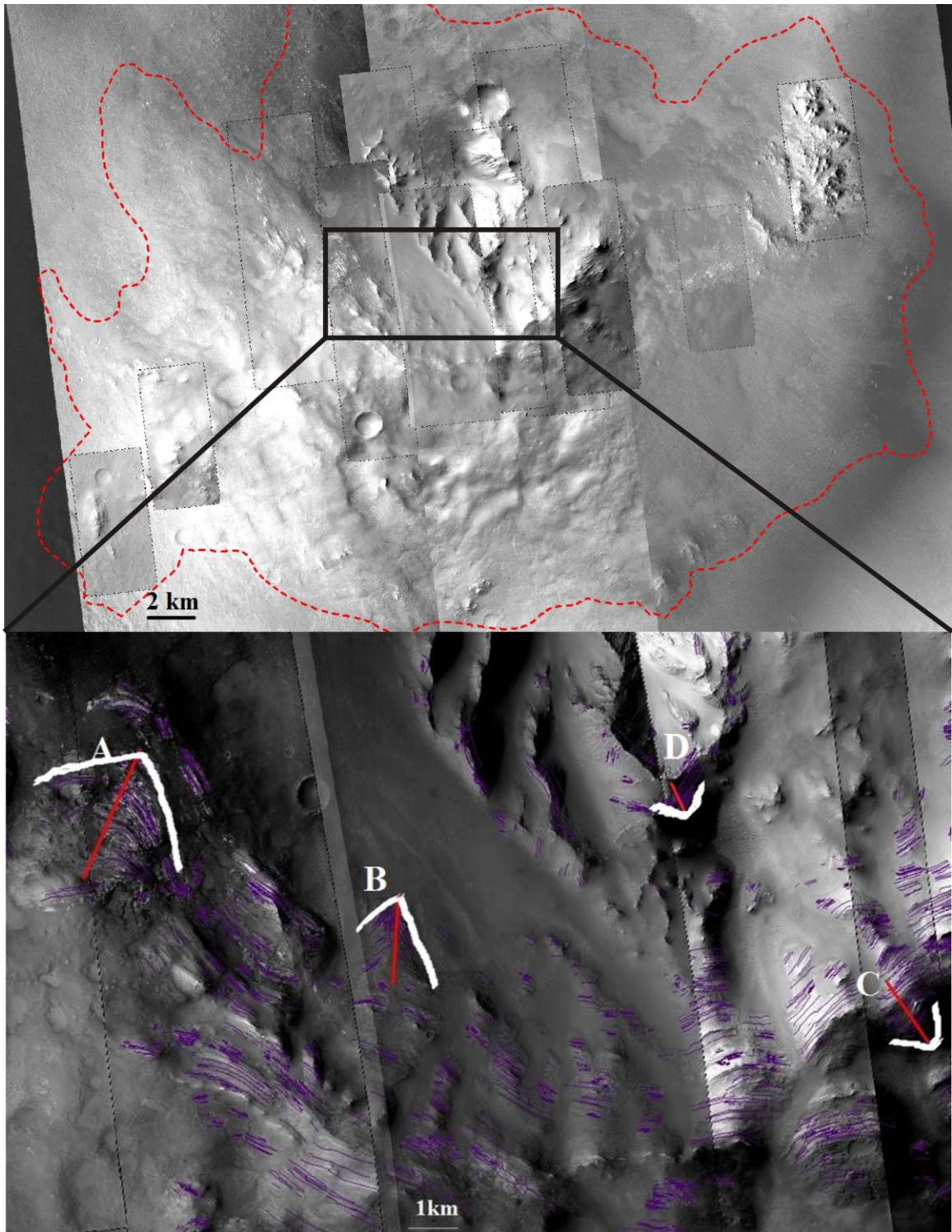


**Figure 29. Few clear folds observed in the layered section of the Crater on HiRISE images; PSP\_002446\_1700\_RED, ESP\_027882\_1700\_RED. Purple lines show the bedrock, white lines show the limbs and red lines show the fold axis. Image: NASA/JPL/University of Arizona.**

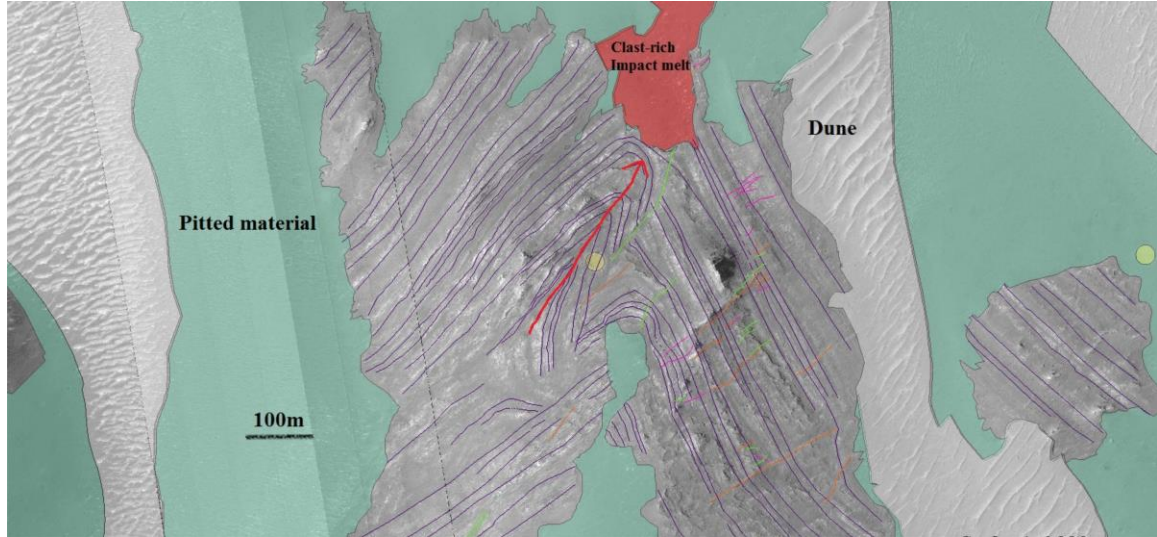


**Figure 30.** Image of fold B in HiRISE PSP\_002446\_1700\_RED, fold axis displayed by red arrow, bedding seen by purple lines, faults by green lines, dykes by orange lines, and fractures by pink lines. Image: NASA/JPL/University of Arizona.

### 4.2.3. Dykes

These structures are oriented slightly perpendicular to oblique to the bedrock with trends of NE-SW and NW-SE. The higher concentration of these features can be found in the central region of the central uplift (Fig. 31). We observed 139 dykes ranging from ~ 2 to ~ 80 m in width and ~ 1 m up to 1.3 km in length in our mapped area. We showed two obvious random dykes with thickness of 4-6 m with a close up of one of them in Figure 32. They can be recognized easily during mapping, because of their thickness, dark-toned materials (Ding et al., 2014; Marzo et al., 2010; Tornabene et al., 2010).



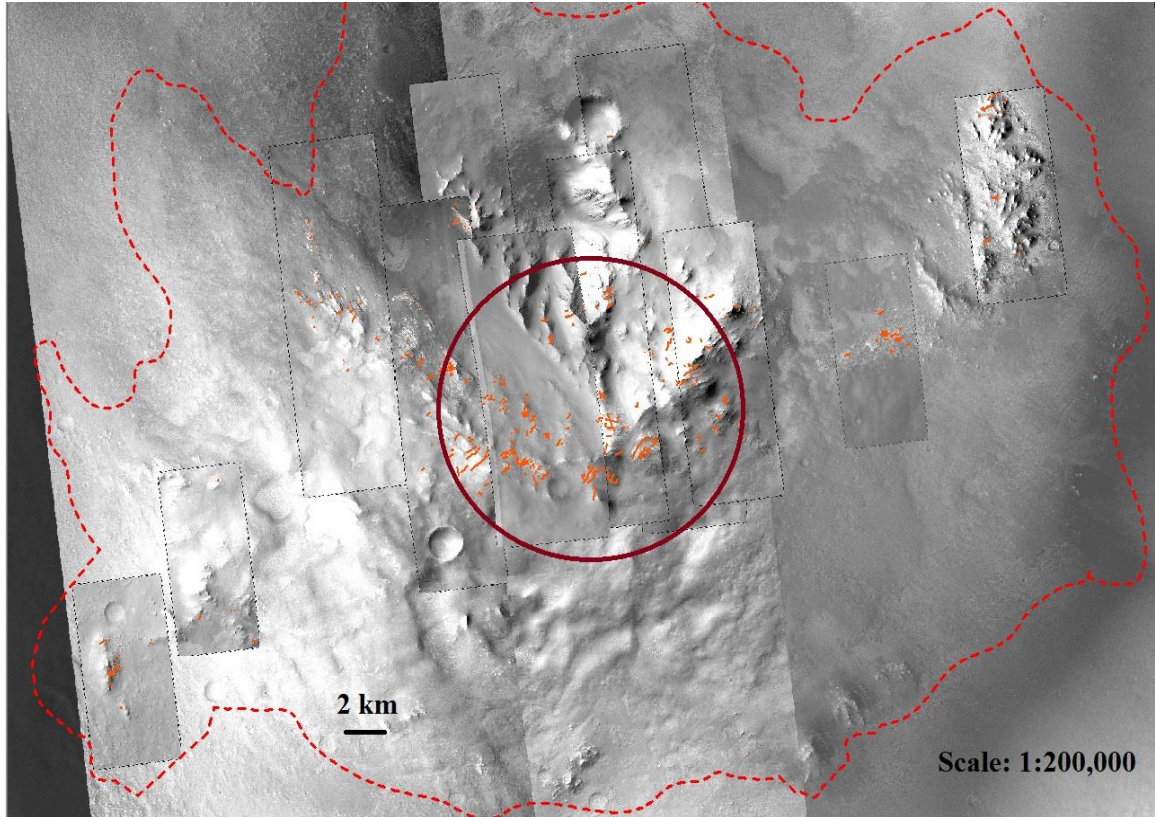


**Figure 31.** This image shows higher concentration of dykes in orange colour in the centre, outlined by the red circle. Image: NASA/JPL/University of Arizona.

At the southeastern end of the breccia dyke in Figure 33, an obvious offset can be seen, so this kind of dyke might be categorized as an offset dyke with 40 m offset. The breccia dyke cuts pretty perpendicularly through the bedding. The major trend of preferred orientation of the dykes sections in our area is NE-SW (Fig. 34).



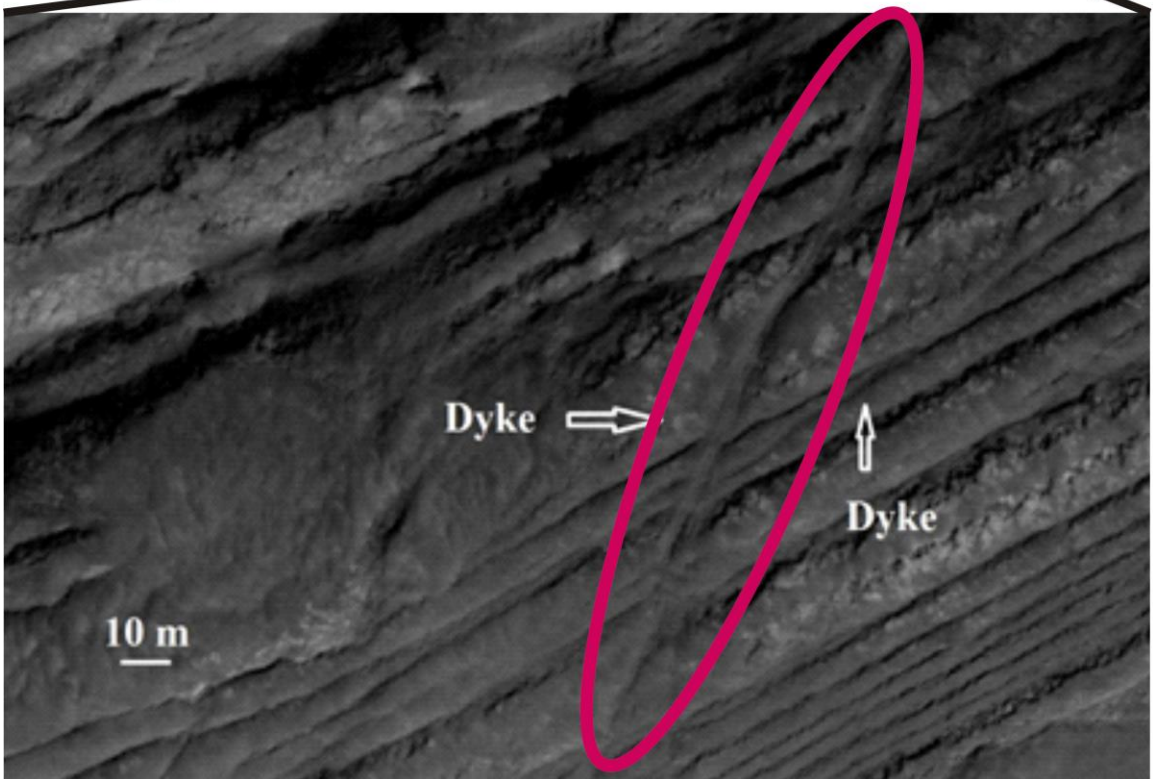
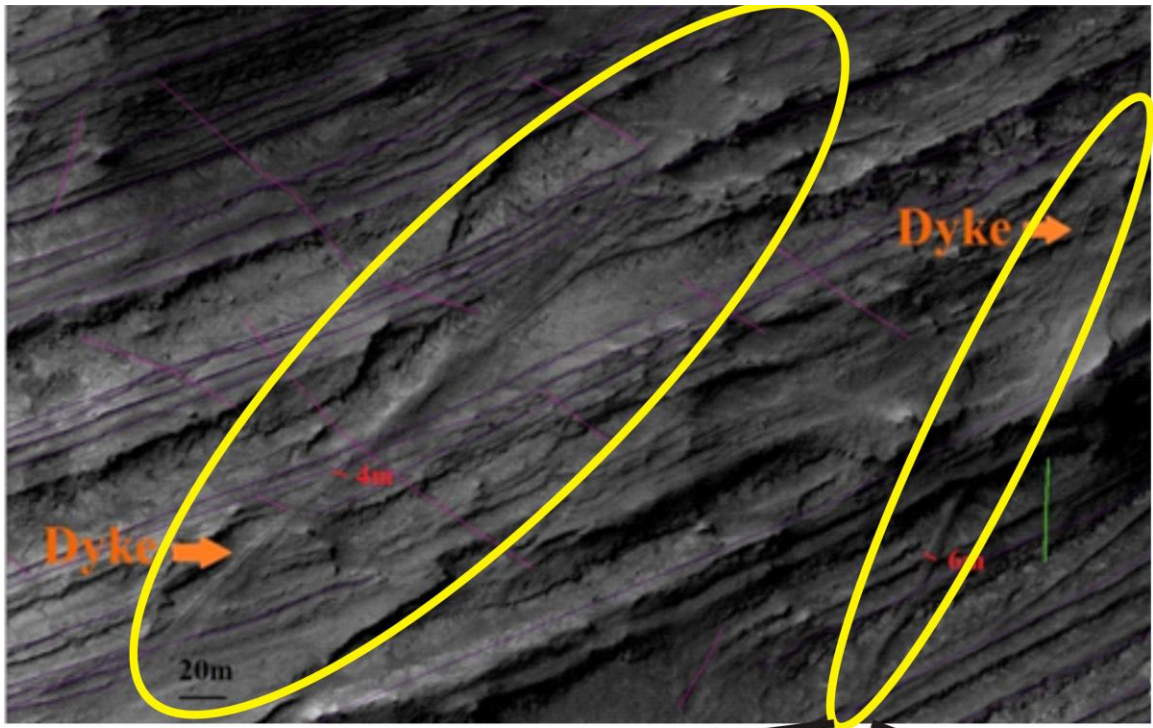
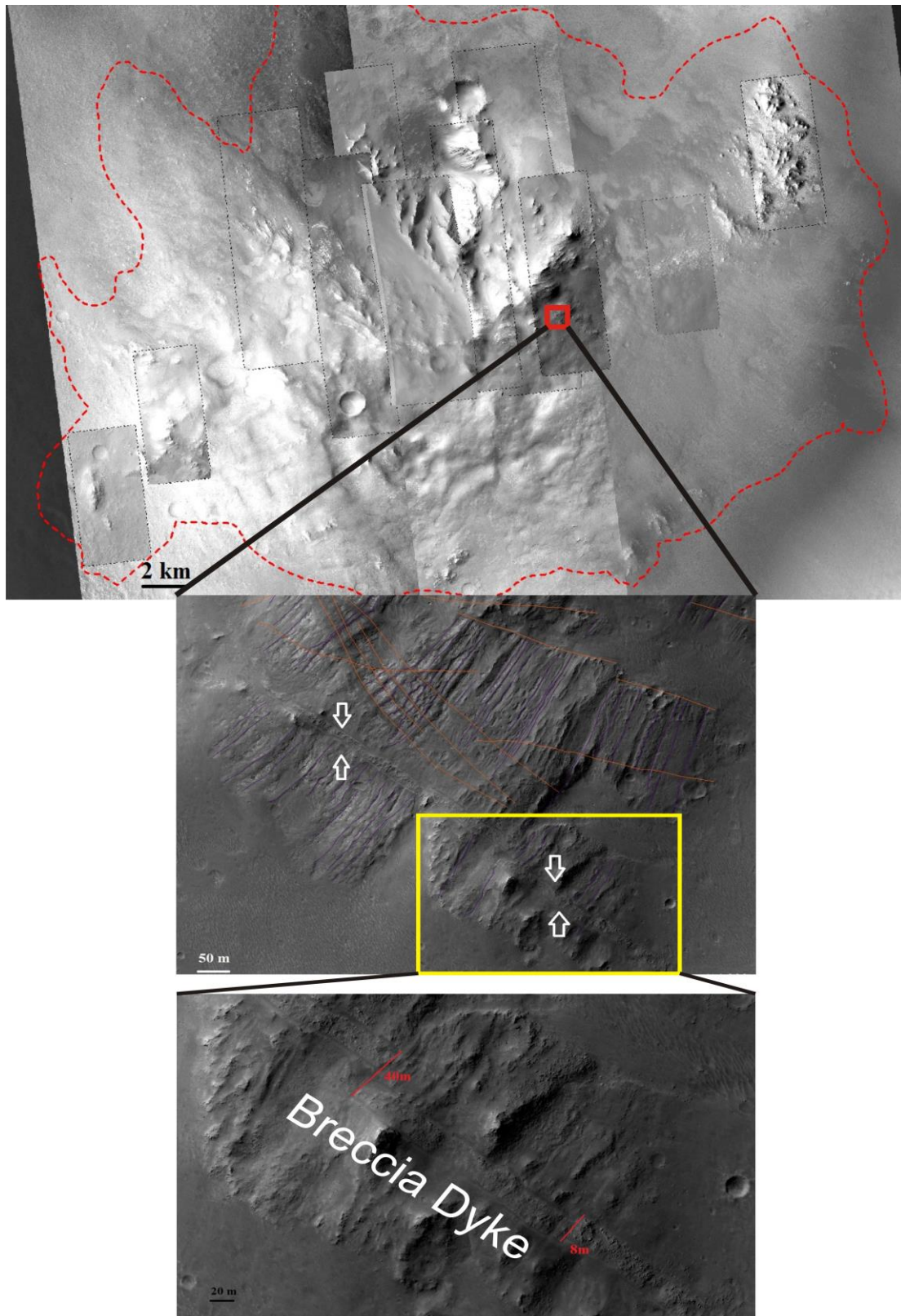


Figure 32. This image shows offsets caused by dykes which shown by orange arrows observed in HiRISE PSP\_008195\_1700\_RED, red digits (4 km, and 6 km) showed a thickness of the dykes. This image is a close up one of the dykes showed by white arrow in the previous photo. Image: NASA/JPL/University of Arizona.



**Figure 33.** Impact breccia dyke is cutting sharply through layers. Dykes shown by orange polylines and layers shown by purple ones. HiRISE imagery; PSP\_008195\_1700\_RED. Image: NASA/JPL/University of Arizona.



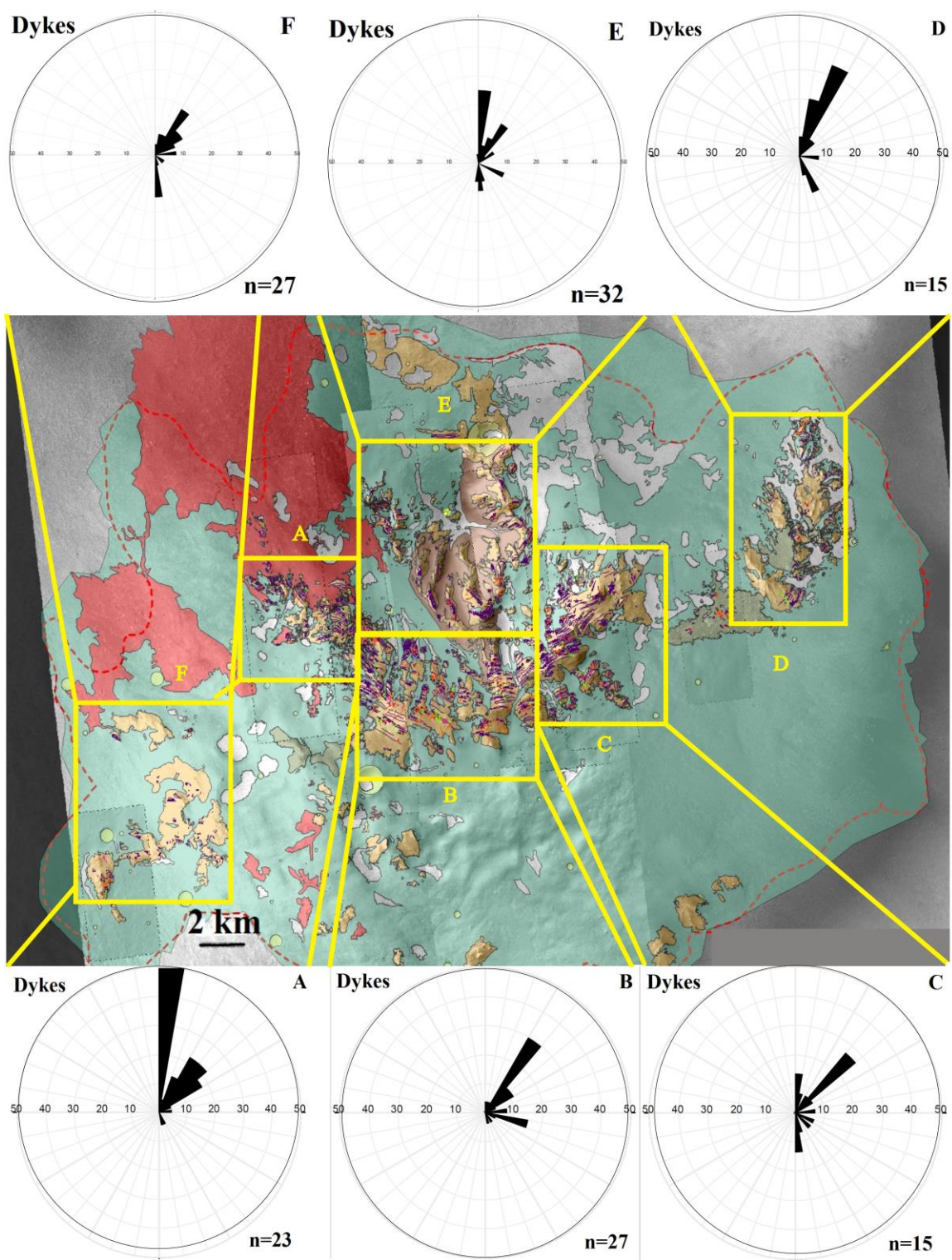


Figure 34. Rose diagrams of dyke trend. Image: NASA/JPL/University of Arizona.

## **5. Interpretations and Discussion**

The major result of this work has been the production of a geological and structural map of the central uplift of the 124 km diameter Oudemans Crater. This represents the most detailed geological map produced to date of the largest central uplift exposing extensive layered bedrock on Mars. The results of this geological mapping and associated geomorphological and structural investigations are discussed below.

### **5.1. Exposed layered bedrock and undivided bedrock**

Layered bedrock are useful for structural mapping as the layers provide a frame of reference from deformation (Caudill et al., 2012a; Wulf et al., 2012). Layered bedrock has been defined as “large megablocks of flat-lying layered bedrock excavating from deep depth then tilted and fractured during the impact process” (Caudill et al., 2012a; Nuhn, 2014; Tornabene et al., 2012a; Tornabene et al., 2010; Tornabene et al., 2014; Wulf et al., 2012). The exposed layered megablocks are uplifted, tilted, and deformed during the modification stage of crater formation and are consistent with observations of layered bedrock from other studies. The exposed layered bedrock unit is similar to descriptions in previous studies of exposed layered bedrock within the central uplifts of other Martian impact craters (Caudill et al., 2012a; Marzo et al., 2010; Nuhn, 2014; Quantin et al., 2012; Tornabene et al., 2012a; Tornabene et al., 2010; Wulf et al., 2012). As at many other localities throughout the Tharsis region, these exposures of layered bedrock within the Oudemans central uplift contain both dark-toned and light-toned fractured bedrock. Oudemans Crater layers are consistent with this interpretation with the lighter and thicker lower-standing layers being thought to be pyroclastics, while the thinner higher-standing darker layers are likely intervening basaltic lava flows (Caudill et al., 2012a; Quantin et al., 2012; Tornabene et al., 2012a; Tornabene et al., 2010; Wulf et al., 2012). Spectral analyses of the Oudemans layered bedrock central uplift (Quantin et al., 2012) indicate that these materials are dominated by mafic components (interpreted to be basalts), which is consistent with the previous volcanic interpretation by Tornabene et al ( 2010).

The layered bedrock within the Oudemans central uplift is best exposed in sections A, B and C as a curved-shaped unit. Conversely, the layered bedrock in a few parts of the central uplift (sections F and D) is least exposed when compared to sections A, B and C.

Sections F and D were mapped predominately as the Undivided Bedrock unit, which has a topographic expression indicative of bedrock, but appears to be extensively coated by some sort of smooth and indistinct materials (discussed below) (Fig. 35).

Section E, representing the core of the uplift (Fig. 18), displays the least abundant and layered bedrock exposure due to coverage by smooth units. Fracturing and massive texture of the bedrock is the visible rock type of this; however this unit is coated by other deposits (e.g., aeolian deposits, mass wasting and lava flows). High resolution images have shown that there are three basic types of uplifted bedrock in complex crater central uplifts on Mars based on a global database produced by (Tornabene et al., 2010; Tornabene et al., 2014). These include: 1) Layered Bedrock (LB), 2) Massive and Fractured Bedrock (MFB), 3) Megabrecciated Bedrock (MMB). This section is massive in appearance (Fig. 18), and thus may represent the massive, fractured bedrock unit observed within several central uplifts across Mars and is also consistent with observations of (Tornabene et al., 2012a). The high slope-forming aspect and the higher elevation of the bedrock within the core of the central uplift may suggest that it is a different lithology and topography from the layered bedrock. If the core of the Oudemans uplift (Section E) truly lacks layered bedrock, then the Oudemans uplift may expose and sample a contact between the oldest and deepest lavas in the region and the underlying ancient basement rock (heavily- cratered Noachian basement). However, it should be noted that the highest amount of deformation occurs in the centre of central uplifts, which is consistent with observations of terrestrial craters (Kenkmann et al., 2005).

The thickness of layered bedrock is thought to represent the culmination of the extensive volcanic history of the Tharsis region and, exposed by and below Oudemans Crater is high.

Mest et al (2011) estimated ~7-11 km of uplift within the uplift of Oudemans Crater, while Caudill et al (2012) and Quantin et al (2012) estimated a pre-impact thickness of the layered deposits as ~ 14 km and ~18 km respectively.

However, these previous authors did not take into consideration the fact that the core does not expose extensive layers, and over thrusting of stratigraphic units in central uplifts e.g., (Kenkmann et al., 2014) and thus the thickness of the Tharsis lavas, based on the

mapping results herein, may suggest a thickness of substantially less than 18 km. This has implications for estimate and models that attempt to understand the volcanic history of Tharsis, as well as climate models that try to account for the input of volcanogenic gases into the atmosphere of Mars. These estimateds are based on stratigraphic section uplift (SU) equation (the uplift is not completely layered) (Caudill et al., 2012).

The orientation of 238 bedding planes is plotted in Figure 35. The major trends of the bedding shows a NW-SE direction for areas A, B, and a NE-SW trend for area C, and D located in the eastern part of the central uplift. Areas E and F show slight trends (NW-SE and NNW-SSE, respectively), but generally show multiple orientations. It should be noted that layered bedrock is the most poorly exposed in these regions.

## **5.2. Crater-fill deposits**

### **5.2.1 Impact melt rocks**

Impact melt rocks form by the passage of shock waves and rarefaction waves through the target body (Grieve et al., 1977). They can be subdivided into categories based on the amount of the clasts: clast-rich, clast-poor, or clast-free (Osinski and Pierazzo, 2013). They are found in multiple locations within complex craters, including as coating on uplifted bedrock (Osinski et al., 2011; Tornabene et al., 2012b), but they are generally recognized as part of the most extensive deposits on the floor of the best-preserved craters, including Mars e.g (Osinski et al., 2011; Tornabene et al., 2012b). They can also have variable clast contents and different textures as a result of their emplacement and cooling history within the impact structure (Osinski et al., 2008). The clast-rich dark-toned unit and the smooth and pitted units are interpreted to be impact melt-bearing units and are similar to units described in other Martian impact craters (Marzo et al., 2010; Nuhn, 2014; Tornabene et al., 2012a; Tornabene et al., 2010). Whereas, the Megabreccia unit in Oudemans (although previously described in multiple occurrences and localities (Grant et al., 2008a; Marzo et al., 2010; Tornabene et al., 2012a; Tornabene et al., 2010; Tornabene et al., 2014) may represent one of the best examples of crater-fill observed megabreccias to date.



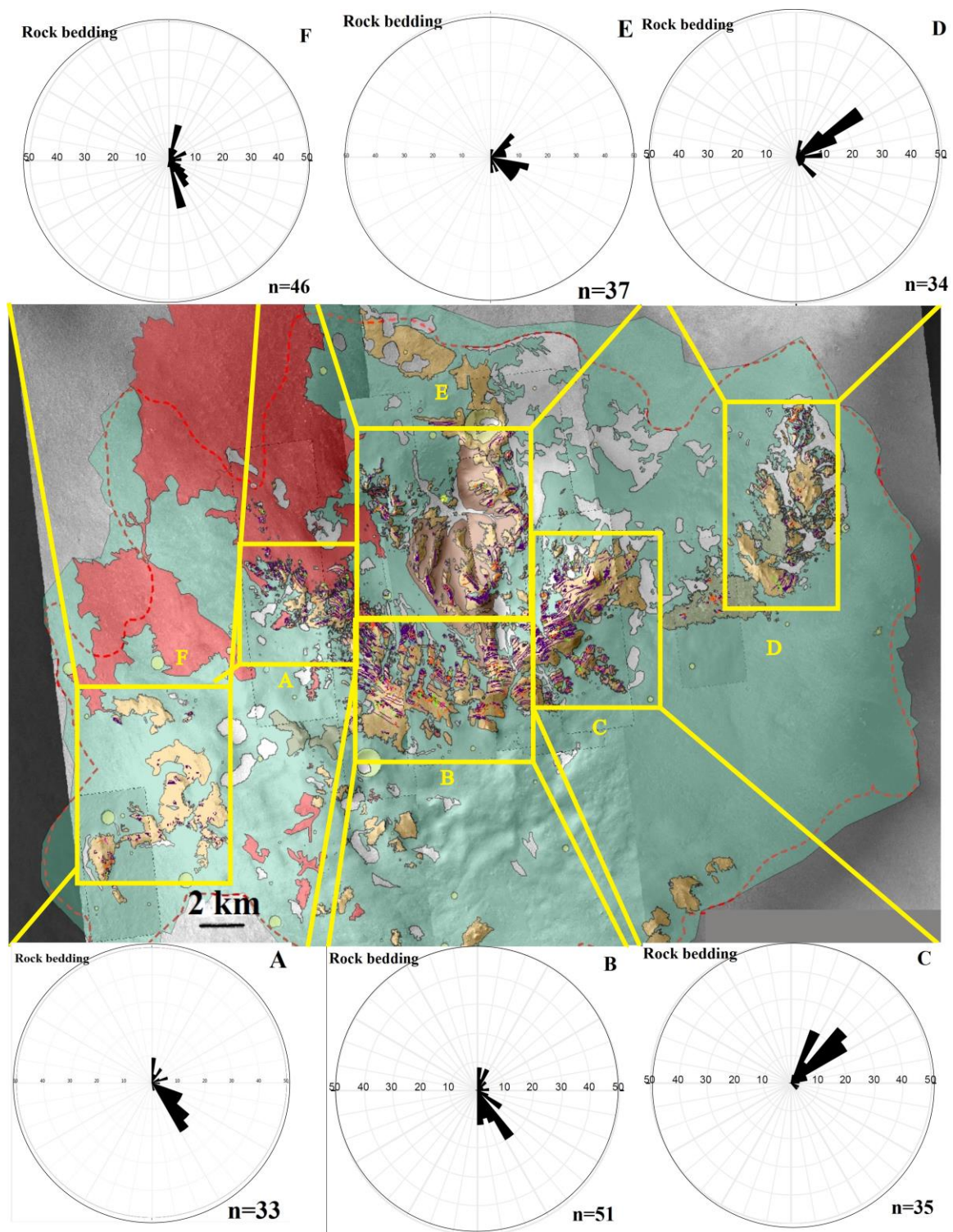


Figure 35. Rose diagrams of bedding trends. Image: NASA/JPL/University of Arizona.

The dark-toned unit has a fine-grained matrix that surrounds light-toned clasts that is observed to overlie the bedrock units and megablocks units. It is located mostly in the northwestern part of the central uplift and overlies all other units except mass wasting and aeolian deposits. Melt drapes the surrounding area and demonstrates flow features that show that it flowed into and accumulated in the topographic low of the central uplift. It covers ~ 10% of the area (Fig. 21). This unit embays and flows along topographic lows between high-standing structurally uplifted megablocks in the central uplift. During an oblique impact, impact melt would be favorably deposited along the direction of the inward projectile. The clasts consist of angular, sub-rounded, and rounded fragments of rocks. Based on the properties described here, and their consistency with previous work (Marzo et al., 2010; Nuhn, 2014; Tornabene et al., 2012a), this clast-rich dark-toned unit is interpreted to be impact melt-bearing unit, which forms the crater-fill deposits surrounding the uplift. The properties and stratigraphic location in the impact crater is consistent with observations of impact melt rocks in terrestrial impact structures (Grieve et al., 1977).

The amount of the impact melt produced in a crater depends on velocity, size of impact, and rock porosities, e.g., (Cintala and Grieve, 1998; Osinski et al., 2011). These melt deposits form a considerable part of an impact crater. Impact melt maintains a high temperature and low viscosity post-emplacement, allowing movement of melt-rich after the cessation of the modification. This would generally give the appearance of multiple melt-bearing flow events. Distribution of flow units interpreted here to be impact melt. The observations made here for Oudemans Crater compare well to observations of impact melt deposits at large impact craters on the Moon (Hawke and Head, 1977), on the Earth (Grieve and Cintala, 1992; Grieve et al., 1977) and Mars (Marzo et al., 2010; Osinski et al., 2011; Tornabene et al., 2010; Tornabene et al., 2014). These studies show that central uplifts are draped by considerable amounts of impact melt rocks. This is critically important for remote sensing studies where compositional data of central uplifts is typically interpreted to represent the signature of uplifted bedrock. These results from Oudemans show that care is needed in the interpretation of such datasets as considerable amounts of impact melt may cover bedrock and, thus, the compositional data from orbit may not be indicative of the bedrock.

### **5.2.2 Martian crater-related pitted material (volatile-rich impact melt deposits)**

This unit is considered as a dark-toned unit; consist of quasi-circular collection of eroded form of crater-related pitted materials varying in preservation within the central uplift floor. This unit also has a distinct surface morphology with dark-toned shallow material and high density of pits (Fig. 22). This unit is located in low-lying topographic areas and is the most extensive deposits of the crater-fill. Smooth and Pitted materials cover much of the floor of Oudemans Crater. Crater-related smooth and pitted materials are wide-spread in many well-preserved and fresh craters ranging from ~1 to 150 km in size (Tornabene et al., 2012b). The smooth and pitted materials are shallow circular or polygonal shaped features with no sign of ejecta blankets or significant rim uplift. Smooth and Pitted materials are thought to form through the interaction of hot deposits and volatiles during impact process and pre-existing water-ice contained in the Martian subsurface (Tornabene et al., 2012b) (Fig. 36). Tornabene et al, 2012a) investigated smooth and pitted materials and suggested that it represents the topmost and highest stratigraphic crater-related portion of crater-fill units within Martian impact craters. These smooth and pitted materials represent the best-preserved syn-impact morphological units. Compared to previous observations of over 200 impact craters (Tornabene et al., 2012a) smooth and pitted materials in our studied area appear to be more eroded especially in the western part of the central uplift. The erosion and deposition rates depend on exposures. There are higher depositions for a negative exposure and less erosion for areas of positive exposure. This is consistent with the large size of Oudemans, which can be broadly used to indicate age because of less erosion in the eastern part of our crater, the smooth and pitted material can be seen more clearly. In the western part of the central uplift, aeolian deposits cover the smooth and pitted materials and pit rims/walls have been more extensively eroded making them more difficult to recognize. They are interpreted to form on a higher elevation part of the crater floor and be almost non-existent within the floor pit boundary. This unit stratigraphically represents the highest unit of the crater-fill deposits.



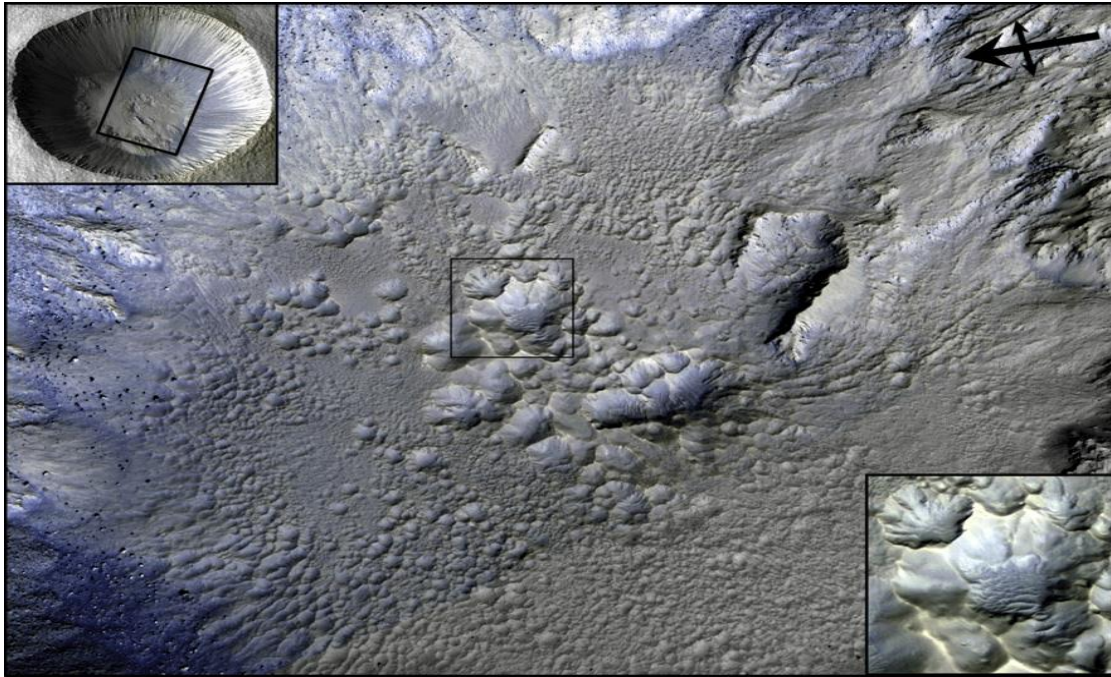


**Figure 36.** Crater-related pitted materials observed on the floor (i.e., the Crater fill) of Zumba Crater in Daedalia Planum from Tornabene et al (2012b). Pitted material shows less erosion compared to the smooth and pitted material in our Crater.

### 5.2.3 Megabreccia

The megabreccia unit described first to comprises large angular, irregularly rounded, and poorly sorted clasts of rock set within a finer grained matrix (Grant et al., 2008a) (Fig. 19). The only logical interpretation, based on the occurrence and stratigraphic relations of this unit, is that it is an impact-generated crater-fill deposit formed during the modification stage. The fine-grained dark matrix may alternately be melt coating. This unit of is inconsistent with the units observed in the central uplift of Toro Crater (Marzo et al., 2010), while is consistent with other central uplifts of complex craters with Noachian units (Tornabene et al., 2012a) and megabreccia unit in the unnamed Crater E (Quantin et al., 2012). Megabreccia units in the Richy Crater draped over the central uplift and are interpreted as a clast-rich and perhaps melt-rich impactite produces by impact event (Ding et al., 2014). There are two relatively well-exposed and extensive megabrecciated units in the east part of the Oudemans central uplift, which show larger clasts compared to the fine clast units and some smaller breccia units exist (Fig. 20). Megabreccia in our area is in the crater-fill deposits. They are most likely erosional windows. Megabreccia stands in relief

suggesting that they are more resistant to erosion than the matrix materials. The large clasts within the mega breccia contain clear layers, similar to the layering seen in the uplifted megablocks of the uplift.

### **5.3. Mass wasting and aeolian deposits**

Light-toned eroded outcrops are found in Oudemans Crater. These units are surrounded by smooth and pitted material. These units are interpreted as mass wasting produced after impact crater process (Fig. 23). Aeolian deposit also formed after impact crater (post impact crater) by saltation of fine grains (Ferguson et al., 2006). They cover all of the other morphologic units, therefore we can interpret this unit as the youngest unit (Amazonian age). These subsequent geologic processes which are as a regional overprint or erosion, show the post- impact history as well (Kenkmann et al., 2014). Mass wasting units are the unconsolidated materials resulting by erosion of bedrock on steep slopes. These are clearly post-impact so are younger than other units in age and can overlie some units in most part of our area (Fig. 24). Dune deposits limit the exposure, especially in the northern and northeastern part of the central uplift.

### **5.4. Nature of the central uplift at Oudemans Crater**

Impact craters are not immediately obvious on the surface of Earth because our planet is geologically active. The surface is in a constant state of change from erosion, infilling, volcanism, and tectonic activity. These processes have led to the rapid removal or burial of Earth's impact structures. As such, studies of central uplifts such as Oudemans offer important potential insights into crater formation.

The crater rim and ejecta blanket of Oudemans are noticeably asymmetric and the crater rim has a gap in the northwestern portion (Fig. 13). In this respect, Oudemans Crater is similar to King Crater on the Moon, which has a Y-shaped central uplift and a gap in the north part of its rim because of pre-existing topography (Fig. 37). Similar to the King Crater rim, the northwestern rim of the Oudemans Crater is not as well defined as most of the rest of the rim. We interpret the asymmetry of the central uplift as a result of lacking of the wall terraces into the northwestern part of the rim toward the canyon system. We also interpret it would be result of the collapse of the uplift due to the collapse of the crater rim

northwards into the canyon system. Melt pond which composed of impact-related melt lies to the northwest of both Oudemans and King, has a relatively flat, smooth surface in the northwestern part of the central uplift. Oudemans was up against Valles marineris, but King Crater cut through an older crater, so rim is lower on the north because of pre-existing void.

In our research, we focused on mapping the main structures. The layers in the uplift experienced a complex structural history including fracturing, dyke formation, faulting and folding during crater formation. It is clear from this study that deformation of the bedrock increases towards the centre of the central uplift. In other words, there is a trend for blocks to become more highly deformed, situated proximal to the centre of the central uplift. We identified several types of dykes, fractures and faults within the mapping area.

We mapped 139 crosscutting structures which we interpret as dykes in the uplifted blocks of the central uplift. We define a dyke as a fracture that has been infilled by impact melt and/or lithic breccia and they formed along fractures. The material in dykes are younger than the rocks that contain them (Marshak, 2009). Dykes within Oudemans Crater show multistage deformation during the impact process as shown by the evidence of multiple displacements or fault offsets especially in the centre. This strongly suggests that the dykes formed early on in the cratering process before the major structural movements during the modification stage. Dyke stands in relief just like the dark layers in the bedrock. This may suggest they have a similar composition.

During the modification stage, faults occur under high strain rate. We infer that faults in this region are concentric thrust faults bounding the large blocks located towards the centre of the central uplift showing higher deformation. The distribution and geometry of faults exposed in the crater floor of complex craters provide the key to reconstruct the kinematic history of a collapsing crater. The preferred orientation of faults seems to be perpendicular to the bedding (oblique to the central uplift) and be possibly thrust faults. The motion along strain-rate faults is the leading mechanism controlling the collapse of complex craters.



Within the uplift, we observed few folds (named A to D) located towards the centre of the central uplift. Some of them appear to be bounded by faults such as Fold B (see Fig. 30). These folds are consistent with high strain rates during an impact event. For example limb of fold B was detached as a result of a fault then offset one of the fold limbs from the other. Our observations would be consistent with (Kenkmann et al., 2005) who noted that the highest amount of deformation is predicted to occur centreward. Moreover, we considered lack of folding in our area would be possibly related to less strain due to the lack of collapse from the wall/terraces to the northwestern part of the rim.

The structural complexity of the central uplift increases towards the centre because the amount of folds, thrust faults and dykes (the intensity of deformation) increase by the motion of rock towards the centre. These structures that formed in layered bedrocks show a preferred orientation of bedding, fault planes, and dykes during the crater modification process.

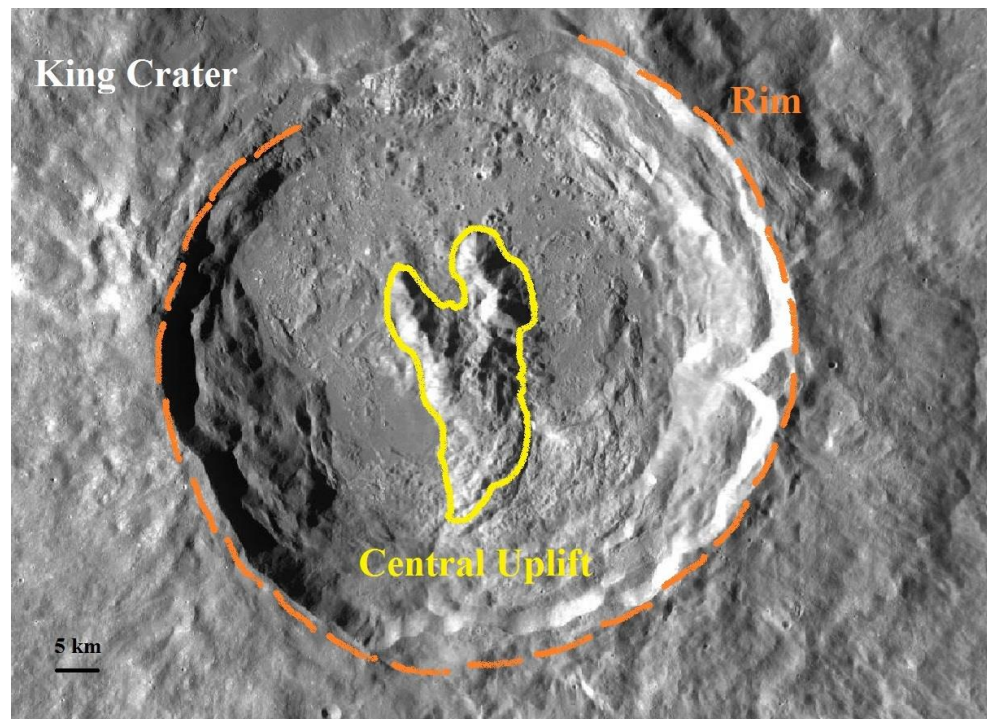


**Figure 37.** This image shows King Crater on Moon. Y-shaped central uplift and collapsed rim displayed by yellow and orange lines respectively.

## 5.5. Stratigraphic history

According to the structural and morphological mapping together with knowledge about the geological setting and formation of impact craters, a generalized stratigraphic column for Oudemans Crater has been produced. Cross-cutting relationships of rocks were used to determine the relative ages of the different units.

- **Pre-existing:**
  - Layered Bedrock
  - Possible fractured and massive bedrock
- **Syn-impact (Excavation and Modification):**
  - Faults, Dykes and Fractures
  - Clast-rich Breccias (Mega breccia) Crater fills in the crater floor
  - Clast-poor and Clast-rich Impact melt
  - Smooth and Pitted materials
- **Post-impact:**
  - Mass wasting
  - Aeolian deposits

By creating the central uplift stratigraphy profile model, age of central uplift units can be estimated; from top to bottom (outer portions of the uplift, moving toward centre), deepest/oldest layer exposure in the centre of central uplift, the unit's age becomes older or lower in the pre-impact stratigraphy. From centre to outward the units becomes younger or higher in the pre-impact stratigraphy: Exposed mega-blocks (layered and undivided bedrocks), megabreccia, smooth and pitted material, impact melt rock mass wasting and Aeolian deposits (Fig. 38).

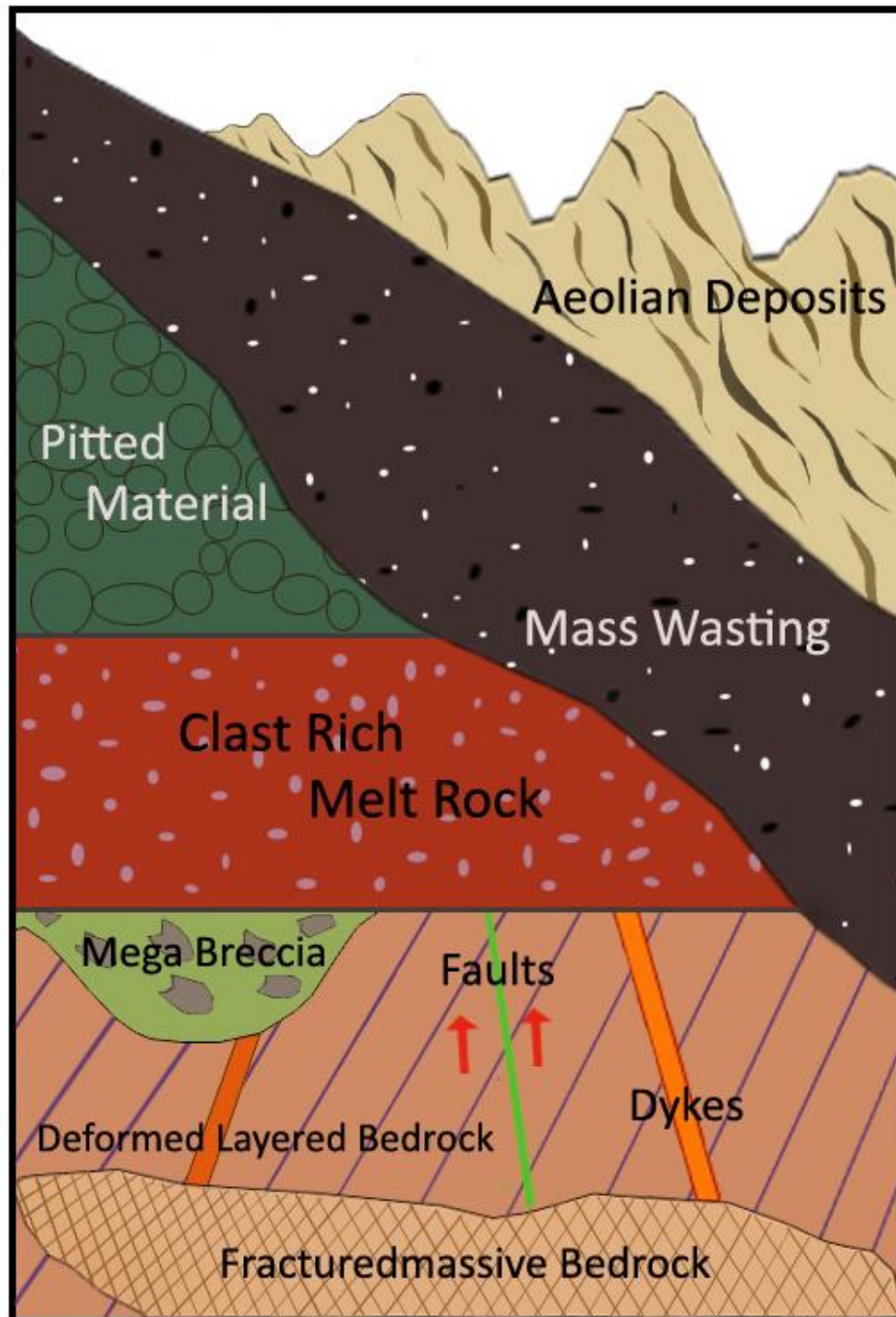


Figure 38. Stratigraphic column ordered units by age, composition and formation time from older to younger.

## 6. Summary and Conclusion

This section will describe the implications and conclusions of this research. The goals of this research have mostly been achieved:

1. General a morphological map by using all available image (HiRISE, CTX, THEMIS, HRSC), and elevation (MOLA, and HRSC DTM's) data in ARC GIS of the central uplift of the crater;
2. Determine relative bedding orientations and a structural map;
3. Perform a geological and structural (lineament) of the area using Arc GIS;
4. Interpret and analyze the stratigraphy and structural deformation history of units of the uplift;

In order to map the morphological and geological structures of the study area, Oudemans Crater central uplift divided into 5 units (layered bedrock and undivided bedrock, megabreccias, impact melt, smooth and pitted material, mass wasting, and aeolian bedforms), then ordered from oldest to youngest age by stratigraphy and lithology aspects. I propose the central uplift affected by the processes of erosion, deposition and regional deformation. In the main, our survey shows an obvious increase in deformation toward the center of the uplift (See Section A, B and C in Fig.). Structural deformation most likely occurred during the formation of the central uplift (Excavation and Modification stages) which most likely related to the active volcanic Tharsis region. The central uplift shows a collapse and slump in the core from impact melts and flows outward over the northwestern part of the rim. Widespread overturning of strata in the central uplift periphery enables the outward collapse.

Most of the layered bedrock unit stands curved-shape in the centre extended to the east and west of the central uplift as undivided outcrops; most of this unit influenced by erosion factors especially undivided outcrops with no clear layering. The clast-rich Megabreccia units appear close to the outer part of the central uplift and are considered to be draped over the central uplift. Infilled impact melt unit mostly covers western part of the central uplift, surrounding all the units with higher elevation to the boundary between units and

filling deposits. Smooth and Pitted material observed most part of the central uplift and surround most outcrops except aeolian and mass wasting deposits. This unit was considered to be more obvious in the eastern part than western part. The western part of the crater is interpreted to be less resistant to weathering compared to the eastern section of the area. Mass wasting unit formed northern part towards centre of the crater in the high elevation topography (located in the E section). Finally, the crater central uplift was affected by aeolian deposits and erosion.

Layered bedrock, undivided bedrock, (complex network of linear features such as fault, fractures and dykes) were interpreted prior to Oudemans Crater formation. Megabreccia, impact melt and smooth and pitted materials were formed as impact-induced (at the same time with crater formation), and mass wasting and aeolian bedforms were considered to be formed after the impact process.

Structural data analyses show the orientation and preferential of linear features (layered bedrock, fault, fracture, and dyke) signify a preferred transport direction during the central uplift of the Oudemans Crater formation process. The concentricity lineament analysis technique used in this study is an approach to quantify lineament localizations.

The orientation of structural elements show that the majority of dykes with the same preferred orientation trend (NE\_SW) to the impact trajectory. Also observed faults have a large thrust component in a high strain zone toward center of the uplift. Moreover, along folds axes in our area, materials were uplifted. Folds could have been formed as deformation zones above faults in this study. The propagation of observed fold is toward the core of the central uplift.

According to our more detailed investigation of the structural study, central uplift of the Oudemans Crater could have been highly deformed by many structural features especially through centre of the central uplift. These results provide further information regarding the effects and styles of modifying process on the central uplift of the Oudemans Crater.

Finally, relation of mapped morphologic and stratigraphic units showed us the trend of the uplifted units from depth to surface and formation age (See section 5.5. Stratigraphic history).



**Appendix A. Results from orientation measurement of linear features of area A.**

Rock beddings			Faults			Dikes			Fractures		
FID	Dir.	Dist.	FID	Dir.	Dist.	FID	Dir.	Dist.	FID	Dir.	Dist.
250	142.01	193.63	273	52.34	21.96	404	40.14	81.26	90	90.25	11.91
3305	143.10	72.26	510	48.76	221.24	401	42.11	103.15	421	44.63	68.76
4090	142.68	478.54	295	55.91	49.86	402	23.72	74.19	424	42.80	41.48
3349	142.02	453.68	512	25.01	66.83	402	44.96	62.61	424	35.08	24.15
243	130.50	459.47	20	90.71	39.79	405	35.75	228.94	424	55.16	50.48
2253	132.57	186.90	489	3.63	113.68	437	43.57	117.00	117	34.22	23.71
3407	119.24	71.50	486	44.60	49.51	438	50.56	41.95	117	34.98	53.75
3407	117.75	159.25	486	21.63	69.32	411	54.19	142.52	73	97.50	62.03
5518	132.21	50.41	513	36.59	41.79	412	33.48	128.34	72	88.16	49.23
3995	167.98	21.82	513	68.75	34.59	414	34.46	65.46	70	31.23	117.91
5953	142.42	126.16	513	52.47	46.04	25	169.35	135.45	431	45.12	134.61
1427	130.61	283.71	48	67.48	37.55	110	9.17	60.57	432	48.60	88.89
5569	117.96	122.39	48	50.19	42.86	95	17.87	165.83	153	16.73	143.39
1437	139.65	173.18	324	26.20	151.02	443	44.23	295.78	176	169.08	41.90
151	128.70	381.65	86	40.24	108.14	440	31.85	175.22	144	119.15	78.77
150	135.45	283.79	47	41.79	178.58	444	68.68	122.82	189	88.90	110.09
268	118.68	741.47	45	94.35	196.32	445	82.73	102.10	135	155.80	104.07
4022	120.25	690.28	305	99.68	174.73	445	52.63	200.11	315	61.07	99.01
4564	127.88	806.58	509	85.98	90.61	94	159.14	79.05	371	44.85	78.38
4530	98.73	356.46	511	113.90	83.09	422	50.23	154.44			
4563	127.40	818.17	59	33.39	173.68	37	21.03	147.04			
4271	77.42	316.60	121	79.07	84.39	37	32.23	64.74			
5958	79.25	325.96				37	27.49	99.82			
4285	37.99	96.51									
6003	148.73	125.20									
6001	0.40	22.62									
6001	17.49	35.49									
6001	6.86	28.36									
6001	37.94	63.34									
6001	27.50	63.72									
1582	4.89	991.51									
313	144.79	488.21									
198	68.53	634.79									

**Appendix B. Results from orientation measurement of linear features of area B.**

Rock beddings			Faults			Dikes			Fractures		
FID	Dir.	Dist.	FID	Dir.	Dist.	FID	Dir.	Dist.	FID	Dir.	Dist.
39	152.62	1265.47	17	95.41	971.34	333	104.26	661.74	355	25.93	1786.18
167	148.61	1176.42	370	36.08	189.48	23	9.55	338.74	202	68.10	345.77
217	145.26	722.94	25	97.30	846.89	79	141.65	549.17	21	72.00	92.98
7196	150.08	2209.07	272	54.69	246.93	419	59.28	362.56	58	90.30	300.37
7194	159.77	1677.28	515	117.92	397.18	160	31.50	354.41	215	18.28	310.57
2976	147.53	1186.13	571	36.47	812.58	85	81.79	309.27	279	27.50	161.96
7199	153.48	638.68	106	149.30	393.87	142	30.18	311.82	205	51.48	155.52
6191	128.10	541.99	14	95.93	994.15	231	16.82	252.57	216	36.92	172.07
1729	134.84	549.30	419	41.01	322.58	478	30.96	138.85	349	68.17	187.38
3779	146.23	917.99	12	120.47	417.47	481	30.62	503.81	355	65.22	113.65
3781	169.69	438.39	20	97.75	830.92	49	110.75	1120.40	5	57.03	350.06
4550	141.91	439.27	339	90.82	185.28	641	35.17	427.23	192	68.01	292.66
6183	171.30	309.47	535	94.88	272.19	673	40.11	1318.15	19	72.00	92.98
3779	147.33	879.69	329	98.94	133.83	637	105.26	543.01	352	90.00	107.95
1209	145.84	564.45	93	55.11	289.97	234	33.46	508.27	434	38.30	68.98
3585	172.41	320.31	341	24.34	158.21	644	38.56	317.92	190	2.24	62.18
7217	2.03	413.09	16	27.15	119.76	501	55.05	576.56	195	36.64	77.77
4894	161.88	612.46	334	91.39	182.37	216	21.95	445.13	196	95.16	64.69
166	57.59	610.91	17	58.34	69.55	506	85.13	781.86	216	38.05	154.55
7201	20.34	1057.09	397	63.16	479.15	508	50.81	556.03	221	92.92	96.25
6135	20.56	895.29	395	38.69	170.81	493	102.42	250.58	281	85.62	107.03
5034	6.08	465.50				409	62.91	661.40	229	26.89	88.47
1177	172.61	288.14				487	44.36	464.10	280	101.65	104.82
4894	122.33	883.04				288	37.21	430.54	432	69.36	112.06
41	89.86	326.23				492	102.99	254.16	223	87.70	139.13
41	75.12	302.29				39	163.67	389.65	291	64.20	70.53
3554	117.60	630.54				545	45.87	202.91	256	39.04	75.62
6183	173.54	368.56									
6187	46.85	742.76									
4490	128.75	829.81									
6198	128.09	1094.71									
114	148.27	236.43									
114	123.30	216.85									
114	80.30	49.74									
112	116.24	403.37									
118	146.69	182.35									
3692	22.71	402.73									
1464	166.68	459.50									
2955	144.01	668.94									
2955	157.67	640.71									
2955	166.69	356.18									
6309	168.91	537.88									
1974	16.48	805.70									
1974	0.46	1052.02									
151	44.76	538.82									
151	18.79	571.80									
151	0.93	132.82									
151	23.75	130.08									
6274	154.56	162.61									

**Appendix C. Results from orientation measurement of linear features of area C.**

Rock beddings			Faults			Dikes			Fractures		
FID	Dir.	Dist.	FID	Dir.	Dist.	FID	Dir.	Dist.	FID	Dir.	Dist.
67	47.03	235.33	44	78.26	156.06	465	14.65	231.03	435	168.79	212.01
67	21.18	514.44	518	0.56	107.05	464	114.00	121.97	436	161.96	90.99
67	42.43	245.90	478	119.69	519.13	466	45.26	113.07	429	153.62	136.49
48	132.18	372.34	126	157.78	434.85	267	42.08	491.42	417	138.59	185.91
48	115.76	590.94	9	121.46	817.04	264	45.20	351.50	224	102.30	864.89
153	57.28	435.33	464	817.04	827.48	248	84.99	264.24	388	132.73	103.28
5632	65.24	255.24	116	172.06	459.49	654	1.07	394.83	402	139.58	208.82
171	40.89	1628.90	443	96.95	254.45	653	133.49	303.61	460	150.12	286.83
5052	46.43	718.65	130	104.83	372.23	439	167.05	405.34	458	154.82	212.35
5257	44.88	772.63	131	156.80	322.40	34	41.40	531.66	456	166.39	467.08
6088	18.51	1174.79	513	164.25	428.85	436	38.30	275.60	457	177.43	402.49
6119	23.21	419.59	595	151.92	232.80	291	170.32	405.83	461	122.91	214.30
5251	47.99	1247.71	509	85.22	372.22	652	9.86	362.27	424	147.80	168.84
5643	39.73	407.70	591	134.76	346.25	273	52.13	120.67	427	143.82	143.82
7111	72.35	610.84	600	176.84	272.79	405	170.32	163.46	405	144.43	70.10
7104	56.79	631.37	87	129.61	398.39						
6100	58.25	718.56	603	169.25	254.33						
7131	23.16	347.07	8	180.00	169.33						
66	31.69	1036.31	598	117.98	383.49						
6094	54.71	1546.14	160	91.90	285.91						
7160	52.35	584.78	599	130.24	180.23						
170	40.98	1734.84									
6084	24.48	3096.25									
97	26.71	2354.69									
108	57.62	1574.16									
7165	44.49	1057.09									
5306	22.61	1084.99									
5312	22.59	319.36									
7149	56.04	468.92									
7151	83.66	503.14									
26	42.81	1471.59									
7151	74.65	839.58									
900	50.34	1357.61									
5157	38.06	638.45									
7139	61.369	721.44									

**Appendix D. Results from orientation measurement of linear features of area D.**

Rock beddings			Faults			Dikes		
FID	Dir.	Dist.	FID	Dir.	Dist.	FID	Dir.	Dist.
7543	63.33	456.85	550	125.10	1435.79	605	25.34	331.39
7546	10.10	192.09	549	119.22	1073.18	610	9.96	140.76
7548	10.10	192.09	552	164.41	205.34	606	165.10	135.80
7544	47.95	726.87	564	133.51	76.01	609	22.95	139.39
2345	48.34	109.13	567	165.45	100.51	587	14.57	170.86
6672	57.53	206.99	568	100.51	58.82	591	37.59	580.15
6675	53.13	238.13	569	2.60	34.96	583	26.52	220.68
6804	137.74	109.65	554	33.69	26.71	618	17.85	410.00
6828	54.09	102.94	548	6.01	60.66	178	26.23	484.59
6808	70.64	166.38	563	151.69	31.64	175	159.59	69.43
6835	113.43	207.62	546	42.88	161.76	612	45.00	215.15
6805	92.78	171.08	545	161.93	156.97	590	95.44	139.54
6829	52.63	280.06	559	104.85	255.31	611	155.77	139.27
6850	63.48	99.27	560	133.87	144.54	613	21.25	122.64
6812	53.43	81.71	561	98.13	52.39	616	14.53	59.04
6816	62.00	123.55						
6816	155.71	58.98						
7580	132.05	272.58						
7580	50.69	184.63						
7582	29.53	161.33						
7585	82.94	105.88						
7558	51.28	353.67						
7552	47.00	736.19						
7555	133.78	131.93						
7554	82.30	319.49						
6860	62.18	161.55						
6886	108.44	160.52						
7561	52.24	356.44						
7567	44.48	311.52						
7574	61.01	335.75						
7563	85.86	274.56						
7563	145.34	182.01						
7570	125.84	176.24						
7561	50.03	352.15						

**Appendix E. Results from orientation measurement of linear features of area E.**

Rock beddings			Faults			Dikes			Fractures		
FID	Dir.	Dist.	FID	Dir.	Dist.	FID	Dir.	Dist.	FID	Dir.	Dist.
8302	110.08	1282.33	676	172.23	99.75	724	17.43	335.56	455	67.22	224.09
365	125.03	881.42	672	152.61	99.42	570	5.91	231.42	453	108.86	68.24
381	138.76	1541.19	675	173.42	69.25	708	175.11	279.54	412	54.05	71.73
6865	53.96	573.33	681	1.77	82.00	631	110.51	224.93	501	112.34	36.59
6851	55.90	526.18	110	165.96	109.09	762	44.24	106.18	500	118.88	40.59
8316	105.81	576.69	570	177.84	350.82	763	25.95	96.00	439	110.72	27.30
174	49.34	852.77	679	146.31	314.81	640	9.92	184.16	504	157.62	116.74
6861	157.73	450.31	678	163.71	200.95	820	30.05	924.65	381	116.93	149.57
7795	157.83	570.46	104	113.96	195.44	818	168.23	282.89	382	124.62	108.03
6447	114.78	284.12	625	173.45	243.68	815	4.54	418.03	377	135.00	145.93
6447	130.59	510.87	626	180.00	202.41	852	3.49	543.40	507	142.37	80.18
7878	54.42	566.09	677	178.78	155.33	723	17.74	347.25	506	148.24	65.35
8288	120.03	953.17	629	118.81	90.59	561	22.57	551.56	508	3.67	31.02
8281	80.45	406.48	530	155.56	191.82	650	22.96	423.85			
8281	108.45	446.44	371	98.75	104.40	707	173.80	306.06			
8286	128.55	649.57	370	39.81	103.32	866	110.16	251.55			
7864	81.52	1452.59	111	107.65	122.17	819	170.13	377.27			
7994	139.10	637.02	372	120.92	131.94	576	54.46	284.51			
7874	100.59	494.03	109	46.44	222.71	719	8.91	341.47			
273	176.30	574.34	112	137.39	179.76	717	34.31	358.73			
7394	48.81	775.20	373	26.03	126.61	636	36.81	473.66			
406	74.05	404.50	115	124.48	51.23	630	113.39	266.64			
4709	66.32	614.75	113	121.61	40.39	631	34.22	399.95			
7395	118.04	827.37	644	165.41	199.58	827	58.05	295.17			
7409	178.85	657.07	636	126.91	244.19	855	180.00	317.50			
7402	41.10	495.06	638	130.68	198.88	734	34.06	537.60			
7925	113.77	945.36	267	159.27	104.67	652	2.12	428.92			
3835	19.37	765.67	375	67.85	124.40	727	357.71	198.60			
7399	9.83	604.19	376	97.13	85.33	736	167.20	179.08			
7399	79.38	258.43	637	113.77	242.86	726	1.82	195.05			
7413	44.36	1268.87	637	95.53	126.45	862	180.00	107.95			
426	65.74	618.16	642	152.02	95.87	865	4.95	165.72			
4489	168.79	144.89	641	129.75	64.31						
4489	133.59	205.29	643	140.71	75.21						
4489	106.70	138.12									
8322	102.67	330.81									
8322	127.75	259.32									



**Appendix F. Results from orientation measurement of linear features of area F.**

Rock beddings			Faults			Dikes		
FID	Dir.	Dist.	FID	Dir.	Dist.	FID	Dir.	Dist.
4746	154.02	649.88	609	90.65	252.81	698	57.69	88.95
5752	145.53	413.35	624	94.03	119.19	698	87.92	29.12
5752	165.92	201.59	622	100.59	147.88	699	54.27	37.16
5752	33.69	103.70	610	85.53	130.34	661	0.92	400.10
7866	158.44	133.39	631	34.66	80.85	681	66.50	167.92
7868	4.73	37.89	633	5.82	71.81	680	47.23	216.25
7868	166.51	95.24	590	12.90	74.80	683	48.96	170.06
7882	21.04	29.48	589	158.59	72.23	589	23.07	459.26
7882	180.00	31.75	585	132.91	70.44	694	133.01	120.78
2213	168.64	115.51	586	111.18	39.37	696	55.39	74.83
2194	15.75	41.83	588	19.50	107.01	693	32.11	127.44
2194	162.62	81.51	587	108.43	65.89	685	33.45	142.07
7943	38.07	55.79	533	37.76	142.58	686	176.42	135.73
7944	168.90	57.70	626	166.57	109.35	688	172.61	144.07
7944	144.32	38.66	625	106.93	38.17	687	161.84	139.50
7957	16.59	116.78	628	50.53	87.10	689	179.09	83.35
7965	18.08	81.83	627	46.22	52.77	690	177.31	112.57
7967	16.84	63.23	629	10.04	45.54	647	16.56	408.52
7967	160.58	44.67	630	172.68	45.57	530	42.38	184.48
7234	172.27	467.27				646	36.96	495.04
7587	144.26	321.28				697	23.77	157.56
7606	166.50	489.78				648	17.58	140.16
7609	129.26	311.41				213	129.37	33.37
7218	112.65	216.68				211	32.17	25.79
7186	146.31	228.95				210	88.18	22.55
7660	136.24	184.17				210	64.39	10.65
7652	120.07	278.82				215	32.96	69.60
7682	139.76	324.41						
7676	120.66	158.79						
7822	142.43	130.19						
7785	110.64	108.56						
2887	14.46	249.45						
7750	99.05	181.65						
7749	85.96	114.25						
7810	79.38	129.21						
2878	61.19	108.71						
7764	19.65	70.80						
7765	82.88	63.99						
7765	69.86	50.73						
6402	130.71	146.33						
6397	139.74	37.14						
6397	28.50	63.22						
7859	63.81	107.92						
7049	52.39	106.86						
7049	4.95	59.69						
7856	168.69	56.66						

**Table 1. The data images of Oudemans Crater with their scale and ID.**

Cameras	Product Number (IDs)	Pixel scale
HiRISE	ESP_025983_1700_RED	$\leq 25\text{cm/pixel}$
	ESP_011966_1700_RED	
	PSP_002446_1700_RED	
	PSP_007048_1695_RED	
	ESP_027882_1700_RED	
	ESP_026194_1700_RED	
	ESP_027117_1700_RED	
	PSP_008195_1700_RED	
	ESP_026273_1700_RED	
	ESP_011676_1700_RED	
	ESP_036176_1700_RED	
CTX	P05_003079_1714_XN_08S091W	$\sim 6\text{ m/pixel}$
	P06_003501_1713_XN_08S092W	
	G20_026194_1690_XN_11S091W	
HRSC	h0442_0008_nd3	150-170 m/pixel
	h2728_0001_nd3	
THEMIS	THEMIS_IRnight_256ppd_60NS_West_v1_equirect_clon0_ly80.jp2	$\sim 100\text{ m/pixel}$
	THEMIS_IRday_256ppd_West_v2_equirect_clon0_ly80.jp2	
MOLA SHADED RELIEF	MOL MEGDR_NE_Oudemans_128ppd_geotiff.tif	$\sim 462\text{ m/pixel}$

## 7. References

- Ahrens, T. J., and O'Keefe, J. D., 1972, Shock melting and vaporization of lunar rocks and minerals: *The Moon*, v. 4, no. 1-2, p. 214-249.
- Allmendinger, R. W., Cardozo, N., and Fisher, D. M., 2011, *Structural Geology Algorithms: Vectors and Tensors*, Cambridge University Press.
- Anderson, J. L., Schultz, P. H., and Heineck, J. T., 2004, Experimental ejection angles for oblique impacts: Implications for the subsurface flow-field: *Meteoritics & Planetary Science*, v. 39, no. 2, p. 303-320.
- Andrews-Hanna, J. C., Zuber, M. T., and Banerdt, W. B., 2008, The Borealis basin and the origin of the martian crustal dichotomy: *Nature*, v. 453, no. 7199, p. 1212-1215.
- Barlow, N. G., 2010, Central pit craters: Observations from Mars and Ganymede and implications for formation models: *Geological Society of America Special Papers*, v. 465, p. 15-27.
- Barlow, N. G., Boyce, J. M., Costard, F. M., Craddock, R. A., Garvin, J. B., Sakimoto, S. E., Kuzmin, R. O., Roddy, D. J., and Soderblom, L. A., 2000, Standardizing the nomenclature of Martian impact crater ejecta morphologies: *Journal of Geophysical Research: Planets* (1991–2012), v. 105, no. E11, p. 26733-26738.
- Barnhart, C. J., 2010, Geologic phenomena related to water on Mars: Post-impact hydrothermal systems, impact excavation and valley network evolution.
- Beyer, R. A., and McEwen, A. S., 2005, Layering stratigraphy of eastern Coprates and northern Capri Chasmata, Mars: *Icarus*, v. 179, no. 1, p. 1-23.
- Bleacher, J. E., Sakimoto, S. E., Garvin, J. B., and Wong, M., 2003, Deflation/erosion rates for the Parva Member, Dorsa Argentea Formation and implications for the south polar region of Mars: *Journal of Geophysical Research: Planets* (1991–2012), v. 108, no. E7.
- Breuer, D., and Spohn, T., 2003, Early plate tectonics versus single-plate tectonics on Mars: Evidence from magnetic field history and crust evolution: *Journal of Geophysical Research: Planets* (1991–2012), v. 108, no. E7.
- Bridges, N., Studies of martian sedimentological history through in-situ study of Gale and Oudemans Craters: Two landing site proposals for the Mars Science Laboratory, *in* *Proceedings First Landing Site Workshop for the Mars Science Laboratory*, Pasadena, CA2006.
- Carr, M. H., 1979, Formation of Martian flood features by release of water from confined aquifers: *Journal of Geophysical Research: Solid Earth* (1978–2012), v. 84, no. B6, p. 2995-3007.
- Carr, M. H., 1981, *The Surface of Mars*: Yale Univ. Press, new Haven, Conn.,
- Carr, M. H., 2006, *The surface of Mars: The Surface of Mars*, by Michael H. Carr. ISBN-10 0-521-87201-4; ISBN-13 978-0-521-87201-0. Published by Cambridge University Press, Cambridge, UK, 2006., v. 1.
- Carr, M. H., and Head III, J. W., 2010, Geologic history of Mars: *Earth and Planetary Science Letters*, v. 294, no. 3, p. 185-203.
- Caudill, C., Tornabene, L., McEwen, A., Byrne, S., Ojha, L., and Mattson, S., 2012a, Layered MegaBlocks in the central uplifts of impact craters: *Icarus*, v. 221, no. 2, p. 710-720.

- Caudill, C. M., Tornabene, L. L., McEwen, A. S., Byrne, S., Ojha, L., and Mattson, S., 2012b, Layered MegaBlocks in the central uplifts of impact craters: *Icarus*, v. 221, no. 2, p. 710-720.
- Christensen, P. R., Jakosky, B. M., Kieffer, H. H., Malin, M. C., McSween Jr, H. Y., Nealon, K., Mehall, G. L., Silverman, S. H., Ferry, S., and Caplinger, M., 2004, The thermal emission imaging system (THEMIS) for the Mars 2001 Odyssey Mission: *Space Science Reviews*, v. 110, no. 1-2, p. 85-130.
- Cintala, M. J., and Grieve, R. A., 1998, Scaling impact melting and crater dimensions: Implications for the lunar cratering record: *Meteoritics & Planetary Science*, v. 33, no. 4, p. 889-912.
- Craddock, R. A., Maxwell, T. A., and Howard, A. D., 1997, Crater morphometry and modification in the Sinus Sabaeus and Margaritifer Sinus regions of Mars: *Journal of Geophysical Research: Planets (1991–2012)*, v. 102, no. E6, p. 13321-13340.
- Dence, M., Grieve, R. A., and Robertson, P., Terrestrial impact structures-Principal characteristics and energy considerations, *in* *Proceedings Impact and explosion cratering: Planetary and terrestrial implications 1977*, Volume 1, p. 247-275.
- Dence, M. R., 1968, Shock zoning at Canadian craters: Petrography and structural implications: *Contributions from the Dominion Astrophysical Observatory in Victoria*, v. 8.
- Dence, M. R., 1971, Impact melts: *Journal of Geophysical Research*, v. 76, no. 23, p. 5552-5565.
- Ding, N., Bray, V., McEwen, A., Mattson, S., Okubo, C., Chojnacki, M., and Tornabene, L., 2014, The central uplift of Ritchy crater, Mars.
- Dressler, B., and Reimold, W., 2001, Terrestrial impact melt rocks and glasses: *Earth-Science Reviews*, v. 56, no. 1, p. 205-284.
- Ferguson, R. L., Christensen, P. R., and Kieffer, H. H., 2006, High-resolution thermal inertia derived from the Thermal Emission Imaging System (THEMIS): Thermal model and applications: *Journal of Geophysical Research: Planets (1991–2012)*, v. 111, no. E12.
- Forsberg-Taylor, N. K., Howard, A. D., and Craddock, R. A., 2004, Crater degradation in the Martian highlands: Morphometric analysis of the Sinus Sabaeus region and simulation modeling suggest fluvial processes: *Journal of Geophysical Research: Planets (1991–2012)*, v. 109, no. E5.
- French, B. M., 1998, *Traces of catastrophe: A handbook of shock-metamorphic effects in terrestrial meteorite impact structures*: Technical Report, LPI-Contrib-954, v. 1.
- Fuller, E. R., and Head, J. W., 2002, Amazonis Planitia: The role of geologically recent volcanism and sedimentation in the formation of the smoothest plains on Mars: *Journal of Geophysical Research: Planets (1991–2012)*, v. 107, no. E10, p. 11-11-11-25.
- Garvin, J. B., and Frawley, J. J., 1998, Geometric properties of Martian impact craters: Preliminary results from the Mars Orbiter Laser Altimeter: *Geophysical Research Letters*, v. 25, no. 24, p. 4405-4408.
- Gault, D. E., Oberbeck, V., and Quaide, W., 1968, *Impact cratering mechanics and structures*. Gerald Schubert, D. L. T., Peter Olson, 2001, *Mantle convection in the Earth and Planets*, Cambridge University Press.
- Grant, J. A., Irwin, R. P., Grotzinger, J. P., Milliken, R. E., Tornabene, L. L., McEwen, A. S., Weitz, C. M., Squyres, S. W., Glotch, T. D., and Thomson, B. J., 2008a, HiRISE imaging of impact megabreccia and sub-meter aqueous strata in Holden Crater, Mars: *Geology*, v. 36, no. 3, p. 195-198.
- Grant, J. A., Wilson, S. A., Cohen, B. A., Golombek, M. P., Geissler, P. E., Sullivan, R. J., Kirk, R. L., and Parker, T. J., 2008b, Degradation of Victoria crater, Mars: *Journal of Geophysical Research: Planets (1991–2012)*, v. 113, no. E11.
- Greeley, R., 1994, *Planetary Landscapes*, New York, London, Chapman & Hall, 286 pp p.:



- Greeley, R., and Spudis, P. D., 1978, Volcanism in the cratered terrain hemisphere of Mars: *Geophysical Research Letters*, v. 5, no. 6, p. 453-455.
- Grieve, R., and Cintala, M., 1992, An analysis of differential impact melt-crater scaling and implications for the terrestrial impact record: *Meteoritics*, v. 27, no. 5, p. 526-538.
- Grieve, R. A., 1975, Petrology and chemistry of the impact melt at Mistastin Lake crater, Labrador: *Geological Society of America Bulletin*, v. 86, no. 12, p. 1617-1629.
- The melt rocks at Brent crater, Ontario, Canada, *in* *Proceedings Lunar and Planetary Science Conference Proceedings 1978*, Volume 9, p. 2579-2608.
- Grieve, R. A., Dence, M., and Robertson, P., Cratering processes-As interpreted from the occurrence of impact melts, *in* *Proceedings Impact and explosion cratering: Planetary and terrestrial implications 1977*, Volume 1, p. 791-814.
- Grieve, R. A., and Therriault, A. M., 2004, Observations at terrestrial impact structures: Their utility in constraining crater formation: *Meteoritics & Planetary Science*, v. 39, no. 2, p. 199-216.
- Harrison, T. N., Malin, M. C., Edgett, K. S., Shean, D. E., Kennedy, M. R., Lipkaman, L. J., Cantor, B. A., and Posiolova, L. V., 2010, Impact-induced overland fluid flow and channelized erosion at Lyot Crater, Mars: *Geophysical Research Letters*, v. 37, no. 21.
- Hauck, S. A., and Phillips, R. J., 2002, Thermal and crustal evolution of Mars: *Journal of Geophysical Research: Planets (1991–2012)*, v. 107, no. E7, p. 6-1-6-19.
- Hawke, B., and Head, J., Impact melt on lunar crater rims, *in* *Proceedings Impact and Explosion Cratering: Planetary and Terrestrial Implications 1977*, Volume 1, p. 815-841.
- Head, J., Greeley, R., Golombek, M., Hartmann, W., Hauber, E., Jaumann, R., Masson, P., Neukum, G., Nyquist, L., and Carr, M., 2001, Geological processes and evolution, *Chronology and Evolution of Mars*, Springer, p. 263-292.
- Head, J. W., Kreslavsky, M. A., and Pratt, S., 2002, Northern lowlands of Mars: Evidence for widespread volcanic flooding and tectonic deformation in the Hesperian Period: *Journal of Geophysical Research: Planets (1991–2012)*, v. 107, no. E1, p. 3-1-3-29.
- Jakosky, B. M., and Phillips, R. J., 2001, Mars' volatile and climate history: *Nature*, v. 412, no. 6843, p. 237-244.
- Jones, E. G., and Lineweaver, C. H., 2010, To what extent does terrestrial life “follow the water”? *Astrobiology*, v. 10, no. 3, p. 349-361.
- Kenkmann, T., Jahn, A., Scherler, D., and Ivanov, B. A., 2005, Structure and formation of a central uplift: A case study at the Upheaval Dome impact crater, Utah: *Geological Society of America Special Papers*, v. 384, p. 85-115.
- Kenkmann, T., Poelchau, M. H., and Wulf, G., 2014, Structural geology of impact craters: *Journal of Structural Geology*, v. 62, p. 156-182.
- Kieffer, S. W., and Simonds, C. H., 1980, The role of volatiles and lithology in the impact cratering process: *Reviews of Geophysics*, v. 18, no. 1, p. 143-181.
- Komor, S. C., Valley, J. W., and Brown, P. E., 1988, Fluid-inclusion evidence for impact heating at the Siljan Ring, Sweden: *Geology*, v. 16, no. 8, p. 711-715.
- Larsen, D., Stephens, E. C., and Zivkovic, V. B., 2009, Postimpact alteration of sedimentary breccias in the ICDP-USGS eyreville A and B cores with comparison to the Cape Charles core, Chesapeake Bay impact structure, Virginia, USA: *Geological Society of America Special Papers*, v. 458, p. 699-721.
- Malin, M. C., Bell, J. F., Cantor, B. A., Caplinger, M. A., Calvin, W. M., Clancy, R. T., Edgett, K. S., Edwards, L., Haberle, R. M., and James, P. B., 2007, Context camera investigation on board the Mars Reconnaissance Orbiter: *Journal of Geophysical Research: Planets (1991–2012)*, v. 112, no. E5. Mars, M., Mars in print.

- Marshak, S. M., 2009, *Essentials of Geology* Norton & Company, Incorporated, W. W., p. 628.
- Marzo, G. A., Davila, A. F., Tornabene, L. L., Dohm, J. M., Fairén, A. G., Gross, C., Kneissl, T., Bishop, J. L., Roush, T. L., and McKay, C. P., 2010, Evidence for Hesperian impact-induced hydrothermalism on Mars: *Icarus*, v. 208, no. 2, p. 667-683.
- McEwen, A. S., Banks, M. E., Baugh, N., Becker, K., Boyd, A., Bergstrom, J. W., Beyer, R. A., Bortolini, E., Bridges, N. T., and Byrne, S., 2010, The high resolution imaging science experiment (HiRISE) during MRO's primary science phase (PSP): *Icarus*, v. 205, no. 1, p. 2-37.
- McEwen, A. S., Eliason, E. M., Bergstrom, J. W., Bridges, N. T., Hansen, C. J., Delamere, W. A., Grant, J. A., Gulick, V. C., Herkenhoff, K. E., and Keszthelyi, L., 2007, Mars reconnaissance orbiter's high resolution imaging science experiment (HiRISE): *Journal of Geophysical Research: Planets* (1991–2012), v. 112, no. E5.
- McEwen, A. S., Malin, M. C., Carr, M. H., and Hartmann, W. K., 1999, Voluminous volcanism on early Mars revealed in Valles Marineris: *Nature*, v. 397, no. 6720, p. 584-586.
- McFadden, L.-A., Johnson, T., and Weissman, P., 2006, *Encyclopedia of the solar system*, Academic press.
- Melosh, H., and Ivanov, B., 1999, Impact crater collapse: *Annual Review of Earth and Planetary Sciences*, v. 27, no. 1, p. 385-415.
- Melosh, H. J., 1989, *Impact cratering: A geologic process: Research supported by NASA*. New York, Oxford University Press (Oxford Monographs on Geology and Geophysics, No. 11), 1989, 253 p., v. 1.
- Mest, S., Weitz, C., and Tornabene, L., Correlation of Low-Albedo Deposits on the Floors of Oudemans Crater and Southeast Noctis Labyrinthus, *in Proceedings Lunar and Planetary Institute Science Conference Abstracts 2011*, Volume 42, p. 2547.
- Morris, A. R., Mouginis-Mark, P. J., and Garbeil, H., 2010, Possible impact melt and debris flows at Tooting Crater, Mars: *Icarus*, v. 209, no. 2, p. 369-389.
- Neukum, G., and Jaumann, R., HRSC: The high resolution stereo camera of Mars Express, *in Proceedings Mars Express: The Scientific Payload 2004*, Volume 1240, p. 17-35.
- Neumann, G. A., Zuber, M. T., Wieczorek, M. A., McGovern, P. J., Lemoine, F. G., and Smith, D. E., 2004, Crustal structure of Mars from gravity and topography: *Journal of Geophysical Research: Planets*, v. 109, no. E8, p. E08002.
- Nimmo, F., and Tanaka, K., 2005, Early crustal evolution of Mars 1: *Annu. Rev. Earth Planet. Sci.*, v. 33, p. 133-161.
- Nuhn, A., 2014, Morphologic and structural mapping of layered central uplifts on Mars [Master of Science Integrated Article]: Western Ontario.
- O'Keefe, J. D., and Ahrens, T. J., 1982, Cometary and meteorite swarm impact on planetary surfaces: *Journal of Geophysical Research: Solid Earth* (1978–2012), v. 87, no. B8, p. 6668-6680.
- O'Keefe, J., and Ahrens, T.J., 1999, Complex craters: Relationship of stratigraphy and rings to impact conditions: *Journal of Geophysical Research: Planets* (1991–2012), v. 104, no. E11, p. 27091-27104.
- Oberbeck, V. R., 1975, The role of ballistic erosion and sedimentation in lunar stratigraphy: *Reviews of Geophysics*, v. 13, no. 2, p. 337-362.
- Osinski, G. R., and Grieve, R. A., 2013, Comparison of Mid-Size Terrestrial Complex Impact Structures: A Case Study: *Impact Cratering: Processes and Products*, p. 290-305.

- Osinski, G. R., Grieve, R. A. F., Collins, G. S., Marion, C., and Sylvester, P., 2008, The effect of target lithology on the products of impact melting: *Meteoritics & Planetary Science*, v. 43, no. 12, p. 1939-1954.
- Osinski, G. R., and Pierazzo, E., 2013, *Impact cratering: processes and products*, John Wiley & Sons.
- Osinski, G. R., Tornabene, L. L., and Grieve, R. A., 2011, Impact ejecta emplacement on terrestrial planets: *Earth and Planetary Science Letters*, v. 310, no. 3, p. 167-181.
- Palme, H., Göbel, E., and Grieve, R., The distribution of volatile and siderophile elements in the impact melt of East Clearwater/Quebec, *in* *Proceedings Lunar and Planetary Science Conference Proceedings 1979*, Volume 10, p. 2465-2492.
- Parfitt, L., and Wilson, L., 2009, *Fundamentals of physical volcanology*, John Wiley & Sons.
- Pike, R. J., Size-dependence in the shape of fresh impact craters on the Moon, *in* *Proceedings Impact and Explosion Cratering: Planetary and Terrestrial Implications 1977*, Volume 1, p. 489-509.
- Pike, R.J., Control of crater morphology by gravity and target type-Mars, earth, moon, *in* *Proceedings Lunar and Planetary Science Conference Proceedings 1980*, Volume 11, p. 2159-2189.
- Pilkington, M., and Grieve, R., 1992, The geophysical signature of terrestrial impact craters: *Reviews of Geophysics*, v. 30, no. 2, p. 161-181.
- Platz, T., Michael, G., Tanaka, K. L., Skinner Jr, J. A., and Fortezzo, C. M., 2013, Crater-based dating of geological units on Mars: Methods and application for the new global geological map: *Icarus*, v. 225, no. 1, p. 806-827.
- Poelchau, M. H., Kenkmann, T., and Kring, D. A., 2009, Rim uplift and crater shape in Meteor Crater: Effects of target heterogeneities and trajectory obliquity: *Journal of Geophysical Research: Planets* (1991–2012), v. 114, no. E1.
- Quantin, C., Flahaut, J., Clenet, H., Allemand, P., and Thomas, P., 2012, Composition and structures of the subsurface in the vicinity of Valles Marineris as revealed by central uplifts of impact craters: *Icarus*, v. 221, no. 1, p. 436-452.
- Reese, C., Solomatov, V., and Moresi, L.-N., 1999, Non-Newtonian Stagnant Lid Convection and Magmatic Resurfacing on Venus: *Icarus*, v. 139, no. 1, p. 67-80.
- Reese, C., Solomatov, V., and Moresi, L. N., 1998, Heat transport efficiency for stagnant lid convection with dislocation viscosity: Application to Mars and Venus: *Journal of Geophysical Research: Planets* (1991–2012), v. 103, no. E6, p. 13643-13657.
- Sharpton, V. L., and Ward, P. D., 1990, *Global catastrophes in Earth history; An interdisciplinary conference on impacts, volcanism, and mass mortality*, Geological Society of America.
- Shoemaker, E. M. I. G. C., 1960, *Penetration mechanics of high velocity meteorites : illustrated by Meteor Crater, Arizona*, Copenhagen, [Berlingske bogtr.].
- Smith, D. E., Zuber, M. T., Frey, H. V., Garvin, J. B., Head, J. W., Muhleman, D. O., Pettengill, G. H., Phillips, R. J., Solomon, S. C., and Zwally, H. J., 2001, Mars Orbiter Laser Altimeter: Experiment summary after the first year of global mapping of Mars: *Journal of Geophysical Research: Planets* (1991–2012), v. 106, no. E10, p. 23689-23722.
- Solomon, S. C., et al, 2005, *New Perspectives on Ancient Mars*, Volume 37, p. 5713 pp.
- Stesky, R., Brace, W., Riley, D., and Robin, P.-Y., 1974, Friction in faulted rock at high temperature and pressure: *Tectonophysics*, v. 23, no. 1, p. 177-203.
- Stöffler, D., 1971, Progressive metamorphism and classification of shocked and brecciated crystalline rocks at impact craters: *Journal of Geophysical Research*, v. 76, no. 23, p. 5541-5551.
- Stöffler, D., and Grieve, R., 2007, *Impactites: Metamorphic rocks*, p. 82-92.

- Strom, R. G., Malhotra, R., Ito, T., Yoshida, F., and Kring, D. A., 2005, The origin of planetary impactors in the inner solar system: *Science*, v. 309, no. 5742, p. 1847-1850.
- Tanaka, K. L., 1986, The stratigraphy of Mars: *Journal of Geophysical Research: Solid Earth* (1978–2012), v. 91, no. B13, p. E139-E158.
- Tanaka, K. L., Scott, D. H., and Greeley, R., 1992, Global stratigraphy: Mars, v. 1, p. 345-382.
- Tornabene, L., Caudill, C., Osinski, G., McEwen, A., Wray, J., Mustard, J., Skok, J., Grant, J., and Mattson, S., 2012a, A crater-exposed bedrock database for Mars with applications for determining the composition and structure of the upper crust[abs], in 3<sup>rd</sup> International Conference on Early Mars: Lake Tahoe, Utah, abstract 7069.
- Tornabene, L., McEwen, A., Caudill, C., Osinski, G., Wray, J., Marzo, G., Mustard, J., Skok, J., Grant, J., and Mattson, S., 2010, A crater-exposed bedrock database for Mars with applications for determining the composition and structure of the upper crust, in *Proceedings Lunar and Planetary Science Conference*, Volume 41, p. 1737.
- Tornabene, L., McEwen, A., Osinski, G., Mouginis-Mark, P., Boyce, J., Williams, R., Wray, J., and Grant, J., 2007, Impact melting and the role of subsurface volatiles: Implications for the formation of valley networks and phyllosilicate-rich lithologies on early Mars, in *Proceedings Seventh International Conference on Mars*, 3288.
- Tornabene, L., Osinski, G., and McEwen, A., 2013, Meter-to Decameter-Scale Morphology of Melt Rocks, Breccias, Bedrock and Structures in Central Uplifts Revealed by the Mars Reconnaissance Orbiter: *LPI Contributions*, v. 1737, p. 3107.
- Tornabene, L. L., Moersch, J. E., McSween, H. Y., Hamilton, V. E., Piatek, J. L., and Christensen, P. R., 2008, Surface and crater-exposed lithologic units of the Isidis Basin as mapped by coanalysis of THEMIS and TES derived data products: *Journal of Geophysical Research: Planets* (1991–2012), v. 113, no. E10.
- Tornabene, L. L., Osinski, G. R., McEwen, A. S., Boyce, J. M., Bray, V. J., Caudill, C. M., Grant, J. A., Hamilton, C. W., Mattson, S., and Mouginis-Mark, P. J., 2012b, Widespread crater-related pitted materials on Mars: Further evidence for the role of target volatiles during the impact process: *Icarus*, v. 220, no. 2, p. 348-368.
- Tornabene, L. L., Osinski, G. R., McEwen, A. S., Ling, V. C., C. M.; , Nuhn, A., Hopkins, R., D'Aoust, B., Kasmai, B., and Mattson, S., 2014, A global synthesis of the meter-to decameter-scale morphology and structure of complex crater central uplifts, *Eighth International Conference on Mars*, Volume 1379: Dabney Hall and Garden, Houston, p. 2
- Turtle, E., Pierazzo, E., Collins, G., Osinski, G., Melosh, H., Morgan, J., and Reimold, W., 2005, Impact structures: What does crater diameter mean?: *Geological Society of America Special Papers*, v. 384, p. 1-24.
- Van Thienen, P., Vlaar, N., and Van den Berg, A., 2005, Assessment of the cooling capacity of plate tectonics and flood volcanism in the evolution of Earth, Mars and Venus: *Physics of the Earth and Planetary Interiors*, v. 150, no. 4, p. 287-315.
- Veverka, J., and Thomas, P., 1979, PHOBOS and Deimos-A preview of what asteroids are like: *Asteroids*, v. 1, p. 628-651.
- Watters, T. R., McGovern, P. J., and Irwin Iii, R. P., 2007, Hemispheres Apart: The Crustal Dichotomy on Mars: *Annual Review of Earth and Planetary Sciences*, v. 35, no. 1, p. 621-652.
- Weizman, A., Stevenson, D. J., Prialnik, D., and Podolak, M., 2001, Modeling the Volcanism on Mars: *Icarus*, v. 150, no. 2, p. 195-205.
- Whitehead, J., Grieve, R., Garvin, J., and Spray, J., 2010, The effects of crater degradation and target differences on the morphologies of martian complex craters: *Geological Society of America Special Papers*, v. 465, p. 67-80.

- Wilson, L., 2009, Volcanism in the solar system: *Nature Geoscience*, v. 2, no. 6, p. 389-397.
- Wilson, L., and Head, J. W., 2007, Explosive volcanic eruptions on Mars: Tephra and accretionary lapilli formation, dispersal and recognition in the geologic record: *Journal of volcanology and geothermal research*, v. 163, no. 1, p. 83-97.
- Witbeck, N. E., Tanaka, K. L., and Scott, H., 1991, Geologic map of the Valles Marineris region, Mars, The Survey.
- Wood, C., Head, J., and Cintala, M., Interior morphology of fresh Martian craters-The effects of target characteristics, *in* *Proceedings Lunar and Planetary Science Conference Proceedings 1978*, Volume 9, p. 3691-3709.
- Wulf, G., Poelchau, M., and Kenkmann, T., 2012, Structural asymmetry in martian impact craters as an indicator for an impact trajectory: *Icarus*, v. 220, no. 1, p. 194-204.
- Zuber, M. T., 2001, The crust and mantle of Mars: *Nature*, v. 412, no. 6843, p. 220-227.
- Zuber, M. T., Solomon, S. C., Phillips, R. J., Smith, D. E., Tyler, G. L., Aharonson, O., Balmino, G., Banerdt, W. B., Head, J. W., and Johnson, C. L., 2000, Internal structure and early thermal evolution of Mars from Mars Global Surveyor topography and gravity: *Science*, v. 287, no. 5459, p. 1788-1793.



## Curriculum Vitae

<b>Name:</b>	Bahareh Kasmai
<b>Post-secondary Education and Degrees:</b>	Islamic Azad University Tehran, Iran 2003-2006 B.Sc.  Islamic Azad University Tehran, Iran 2006-2009 M.Sc.  The University of Western Ontario London, Ontario, Canada 2011-2014 M.Sc.
<b>Honours and Awards:</b>	Western Graduate Research Scholarship (WGRS) 2011-2013
<b>Related Work Experience</b>	Instructor Karaj Payamenoor University 2010-2011  Teaching Assistant University of Western Ontario 2011-2013  Research assistant University of Western Ontario 2011-2014

**Publications:**

L. L. Tornabene, G. R. Osinski, A. S. McEwen, V. Ling, C. M. Caudill, A. Nuhn, R. Hopkins, B. D'Aoust, B. Kasmai, and S. Mattson. (2014). A Global Synthesis of The Metre- To Decametre-Scale Morphology And Structure Of Complex Crater Central Uplifts.